UNIVERSITY OF CALIFORNIA, SAN DIEGO

Properties of nonlinear and breaking deep-water surface waves

A dissertation submitted in partial satisfaction of the
requirements for the degree
Doctor of Philosophy

in

Oceanography

by

Nicholas Edward Pizzo

Committee in charge:

W. Kendall Melville, Chair
Robert Guza
Richard Salmon
Sutanu Sarkar
Jerome Smith

2015

The dissertation of Nicholas Edward Pizzo is approved, and it is acceptable in quality and form for publication on microfilm and electronically:

_____

_____

_____

_____

_____
Chair

University of California, San Diego

2015

EPIGRAPH

"When I heard the learn'd astronomer,
When the proofs, the figures, were ranged in columns before me,
When I was shown the charts and diagrams, to add, divide, and measure them,
When I sitting heard the astronomer where he lectured with much applause in the lecture-room,
How soon unaccountable I became tired and sick,
Till rising and gliding out I wander'd off by myself,
In the mystical moist night-air, and from time to time,
Look'd up in perfect silence at the stars."

—Walt Whitman

TABLE OF CONTENTS

LIST OF FIGURES

LIST OF TABLES

ACKNOWLEDGEMENTS

First, I would like to thank my research advisor, Ken Melville for his support and encouragement, without which this thesis would not have been possible. His passion for science is contagious, and has made our time together very enjoyable.

I would also like to thank my committee members, Satanu Sarkar, Bob Guza, Jerry Smith and Rick Salmon. In particular, Rick Salmon has served as a mentor to the "Theory group", and has, along with Ken, taught me the value of understanding the historical development of scientific ideas. Furthermore, I thank Jerry for our many enjoyable conversations about waves at "TG".

The research presented in this thesis also benefited from the support of current and past members of the Air-Sea Interaction Laboratory. Thanks are due to Peter Sutherland, Ben Reineman, Laurent Grare, Nick Statom, Luc Deike, Luc Lenain and Stephen Holleman.

My time at Scripps was made truly enjoyable thanks to the constant support of friends and colleagues. Although I can not list them all, I thank Brett, Timmy, Roland, Nick, Alan, Roy, Rayleigh, Kelley, Emily, and Sara for making life outside of Scripps so fun.

I thank my family for their encouragement over the years. My parents have always been unwavering in their support, and it is their selflessness that has allowed me to pursue my interests. My brothers have helped keep me grounded. For that, and much more, I thank them.

Chapter 2 is a reprint of the material as it appears in"Vortex generation by deep-water breaking waves", *Journal of Fluid Mechanics*, **734**, p.p. 198-218 by Pizzo, N.P. and Melville, W.K. (2013). Chapter 3 has been submitted to the Journal of Fluid Mechanics as "Current generation by deep-water breaking waves" by Pizzo, N.P., Deike, L., and Melville, W.K. (2015). Chapter 4 has been submitted as "Wave modulation: the geometry, kinematics, and dynamics of surface-wave focusing" by Pizzo, N.P. and Melville, W.K.

VITA

2008	B.Sc. Physics & B.Sc. Mathematics, University of California, Santa Barbara
2009–2015	Graduate Student Researcher Scripps Institution of Oceanography University of California, San Diego
2015	Ph. D. in Oceanography, University of California, San Diego

PUBLICATIONS

Pizzo, N.E. and Melville, W.K. (2013), Vortex generation by deep-water breaking waves, *Journal of Fluid Mechanics*, **734**, 198-218.

FIELDS OF STUDY

Major Field: Physical Oceanography

Studies in Physics
Professors R.K. Pathria, H. Arbabanel, A. Manohar, K. Intrilligator, and M. Di Ventra

Studies in Fluid Dynamics
Professor M.C. Hendershott

Studies in Geophysical Fluid Dynamics
Professors J. MacKinnon and P. Cessi

Studies in Linear and Nonlinear Waves
Professors W. K. Melville, M. C. Hendershott, and R. T. Guza

Studies in Data Analysis
Professors D. L. Rudnick, and R. Pinkle

Studies in Physical Oceanography
Professors J. MacKinnon, U. Send, C. Winant, and D. Roemmich

ABSTRACT OF THE DISSERTATION

Properties of nonlinear and breaking deep-water surface waves

by

Nicholas Edward Pizzo

Doctor of Philosophy in Oceanography

University of California, San Diego, 2015

Professor W. Kendall Melville, Chair

In this thesis we study nonlinear and breaking deep-water surface waves. First, we consider the vorticity generated by an individual breaking wave, drawing on classical literature on vortex generation by impulsive forcing. We employ this theory to develop a scaling argument for the relationship between the generated circulation and the variables characterizing the breaking wave. This model is then compared to limited laboratory experiments, and good agreement is found.

We next pursue a related problem, namely the partitioning of energy in the breaking induced currents, between the turbulent and mean flow. This is the inverse problem to the vortex generation model, as we work backwards from the structure of the induced flow, using existing results on vortex dynamics to find the energy necessary to generate the (half) vortex ring induced by breaking. This

yields a theoretical model for the ratio of the energy in the mean flow currents to the total energy lost from the wave field, in terms of the characteristic variables of the breaking wave. This relationship is then examined numerically, using a direct numerical simulation of the two-phase air-water Navier-Stokes equations, and agreement between the model, the numerical experiments, and limited available laboratory data is found.

One approach to breaking is through the focusing of wave packets. Here, we theoretically and numerically examine weakly nonlinear narrow-banded wave packets. By employing moment evolution equations of the modified nonlinear Schrodinger equation (MNLSE), we derive new predictions for the geometry, kinematics, and dynamics of focusing wave packets. In particular, we predict that as the wave group focuses: the group velocity increases; the packet leans forward; and the energy equipartition (between kinetic and potential) breaks down. These results are then corroborated by numerical integration of both the MNLSE and the fully nonlinear evolution equations for irrotational inviscid deep-water surface gravity waves.

Finally we present several ongoing projects related to nonlinear and breaking surface waves. First, we present a Lagrangian for deep-water surface gravity waves and discuss its numerical implementation. Next, a virial theorem for surface gravity waves is derived. Finally, we derive the criterion for the Benjamin-Feir instability based on a variance identity for the nonlinear Schrodinger equation.

1 Introduction

When wind blows over water, surface waves are created. These waves modulate the transfer of mass, momentum, and energy between the atmosphere and the ocean (*Melville* 1996). Although some of the momentum and energy transferred from the atmosphere to the ocean is propagated away in the form of swell, the majority is deposited locally into the water column by wave breaking. Therefore, a better understanding of the properties of these waves as they focus and break is crucial for accurately describing upper ocean processes. This dissertation attempts to better understand properties of the mean flow induced by wave breaking, and the nonlinear properties of surface waves as they focus.

Wave breaking is a two-phase turbulent unsteady flow, making theoretical, numerical, and laboratory studies difficult (*Perlin et al.* 2013). Although early theoretical work elucidated a great deal about the structure of weakly nonlinear deep-water waves, wave breaking is out of reach of any known analytical techniques. Furthermore, as the scales present in breaking span several orders of magnitude, numerical methods have only recently become robust enough to model the full wave breaking process (*Deike et al.* 2015). This has motivated the need for detailed laboratory studies to guide theoretical and numerical analysis. In this thesis, the questions we consider are motivated by laboratory observations. Theoretical models are then derived, and in some cases numerical simulations are used to further examine and corroborate these predictions.

A classic approach to studying deep-water breaking waves in the laboratory employs a dispersive focusing technique (*Longuet-Higgins* 1974) to create reproducible breaking waves (*Melville and Rapp* 1985, *Rapp and Melville* 1990). In particular, longer faster waves are generated after slower shorter waves, and linear

wave theory is used to constrain the waves to meet at a point in space and time, potentially leading to wave breaking. This allows for a systematic study of local and global properties of breaking waves. Two parameters define these wave packets: the first is the maximum linear slope at focusing, S, and the second is the (normalized) bandwidth Δ. Both of these parameters are known *a priori*.

An important recent study that employed this technique was performed by *Drazen et al.* (2008). The authors used an inertial scaling argument (*Taylor* 1935) for *plunging* breaking waves to deduce the dependence of the energy dissipated by breaking on the variables characterizing the breaking wave. By constructing a simple argument based on the geometry of a wave at breaking, it was found that the relevant variable characterizing the energy dissipation is S, which recall is the maximum linear slope at breaking. This parameter can be interpreted as the energy available to the water column from the wave field. The argument was then compared to all available laboratory data (*Romero et al.* 2012), and good agreement was found over nearly three orders of magnitude, including for waves that were gently spilling. The simplicity and robustness of this scaling argument has motivated much of the work contained in this thesis.

First, we study properties of the mean flow generated by deep-water breaking waves. The ensemble-averaged breaking induced flow is characterized by a coherent vortex, lasting more than 50 wave periods after the breaking event. The structure of this induced flow has been shown to be crucial to the dynamics of the upper ocean (*Sullivan et al.* 2004, 2007), so that a better understanding of this process can greatly enhance coupled atmosphere-ocean models (*Cavaleri et al.* 2012). We explain the structure of the mean flow induced by breaking, and through classical fluid mechanics and a scaling argument we connect the circulation of the induced vortex with the variables characterizing the breaking wave. The model is compared with limited available laboratory data, and agreement is found.

The structure of the induced flow then allows us to use classical methods in vortex dynamics to deduce integral properties of the flow induced by breaking. In particular, the vortex structure constrains the momentum and energy that is needed to generate this mean flow current. This allows us to deduce a scaling

argument for the ratio of the energy in the mean flow to the total energy lost by the wave field. It is found that at least 95% of the energy lost from the wave field due to breaking is locally dissipated in the water column by the generation of turbulence and mixing. The theoretical model is corroborated by numerical experiments and limited existing laboratory data. If the result holds up under further laboratory and field measurements, it will serve as a first step towards answering the question: How is the energy lost from the wave field distributed between currents and turbulence? With recent developments in measuring and scaling the statistics (*Sutherland and Melville* 2013) and dynamics of breaking (*Romero et al.* 2012), this should lead to significantly improved predictions of the generation of ocean currents and upper ocean mixing.

The two chapters discussed above make it clear that the slope at breaking provides a robust characterization of certain integral properties of breaking waves. This motivated us to examine the evolution of the characteristic variables of waves and wave packets as they focus. In particular, we consider the geometry, kinematics, and dynamics of weakly nonlinear narrow-banded surface gravity wave packets governed by the modified nonlinear Schrodinger equation (MNLSE). The MNLSE, and its lower order counterpart the nonlinear Schrodinger equation (NLSE), have garnered considerable interest from a variety of different fields, including mathematics, physics, and oceanography (*Sulem and Sulem* 1999). We use techniques developed in the plasma physics and optics community to establish facts about the wave field as it focuses. In particular we explain the asymmetric forward leaning of the packet as it focuses; that is, the steeper slope of the forward face of the packet. Furthermore, we quantify the modifications to the group velocity due to focusing, finding that wave packets speed up as they focus. Finally, the breakdown of equipartition, between kinetic and potential energy, is then related to the focusing of the wave packet. Numerical simulations of the MNLSE, and the fully nonlinear potential flow equations, are then used to corroborate the theoretical predictions.

This dissertation is composed of three research chapters. Chapter 2 is a reprint of the material as it appears in "Vortex generation by deep-water breaking waves", *Journal of Fluid Mechanics*, **734**, p.p. 198-218 by Pizzo, N.P. and Melville,

W.K. (2013). Chapter 3 has been submitted to the Journal of Fluid Mechanics as "Current generation by deep-water breaking waves" by Pizzo, N.P., Deike, L., and Melville, W.K. (2015). Chapter 4 has been submitted as "Wave modulation: the geometry, kinematics, and dynamics of surface-wave focusing" by Pizzo, N.P. and Melville, W.K. In Appendix A, we derive a Lagrangian for water waves, and present a numerical model based on this description. Appendix B derives a virial theorem for the fully nonlinear potential flow equations governing irrotational inviscid deep-water surface gravity waves. Finally, in Appendix C we show how the Benjamin-Feir instability can be derived from the variance identity of the nonlinear Schrodinger equation. Each of the appendices is currently being prepared for publication. Each chapter and the appendices begin with an introduction, and end with a summary.

2 Vortex generation by deep-water wave breaking

2.1 Introduction

Breaking waves are an important mechanism for modulating and enhancing the flux of gases, heat, and momentum across the air-sea interface (*Melville* 1996). Breaking is believed to be the main way that momentum is passed from the wind-driven irrotational wave field into the underlying rotational ocean currents. An improved knowledge of the modification of these fluxes due to breaking is crucial for a better understanding of the mechanisms involved in air-sea interaction, and specifically for the enhancement of coupled atmosphere-ocean models. Although there have been recent advances in laboratory and field measurements, the problems associated with wave breaking still present demanding experimental, numerical, and theoretical challenges. Therefore, even simple theoretical models focusing on the response of the water column to breaking can prove to be valuable in gaining a better understanding of air-sea interaction from local to global scales (*Banner and Peregrine* 1993, *Melville* 1996). In this chapter, we present a model relating the circulation generated by a breaking wave to the wave energy dissipated due to breaking.

Duncan (1981) performed laboratory experiments involving quasi-steady breaking generated by flow over a submerged hydrofoil. The scaling of dissipation *Duncan* (1981) found is consistent with the description *Lighthill* (1978) presented of the wave power generated by flow past a cylinder. Using the balance of forces for breaking waves presented in *Duncan* (1981), *Phillips* (1985) proposed a model

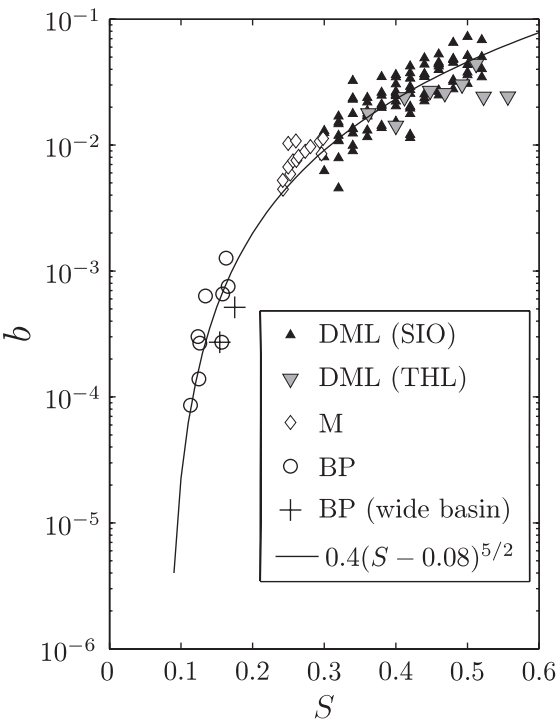

Figure 2.1: Analysis of laboratory measurements, adapted from *Romero et al.* (2012), of the breaking parameter b versus the maximum linear slope at breaking, S, as defined in equation (1.2). DML (SIO) and DML (THL) is data from *Drazen et al.* (2008), M is data from Melville (1994), BP and BP (wide basin) are data from *Banner and Peirson* (2007) and the solid line represents the fit predicted by the scaling argument of *Drazen et al.* (2008), with coefficient 0.4 and threshold slope of 0.08 chosen to best fit the data. See *Romero et al.* (2012) for more details.

for the energy dissipation rate of a breaking wave per unit length of breaking crest, ϵ_l:

$$\epsilon_l = \mathrm{b}\frac{\rho c^5}{g}, \tag{2.1}$$

where ρ is the density of water, g is the acceleration due to gravity, c is the characteristic wave phase speed and b is a non-dimensional breaking strength parameter. Dimensional analysis arguments by *Melville and Rapp* (1985), *Melville* (1994), *Drazen et al.* (2008) show that b is a function of the bandwidth of the breaking wave group, the rate at which focusing occurs, and the wave slope at breaking, S. Following *Drazen et al.* (2008), this is defined as the linear prediction of the slope

at focusing of the wave packet,

$$S = \sum_n a_n k_n, \tag{2.2}$$

where the summation is over all amplitudes a_n and wavenumbers k_n of the input wave packet.

Drazen et al. (2008) proposed an inertial scaling model for plunging quasi two-dimensional breaking based only on the local slope hk at breaking, finding

$$\mathrm{b} = \beta(hk)^{\frac{5}{2}}, \tag{2.3}$$

where β is a constant of order unity, h is the wave height at breaking, and k is the characteristic wavenumber of the breaking wave defined through the linear dispersion relation, $c^2 = g/k$. The slope at breaking hk does not necessarily relate to S, the linear prediction of the slope at breaking, in a simple way, since wave breaking is an inherently non-linear process, especially as the point of breaking is approached; however, the experiments and analysis of *Drazen et al.* (2008, see §5) and *Tian et al.* (2010, §3.1.5) show that within the scatter of the laboratory data the two quantities are approximately linearly related.

Equation (2.3) has been corroborated through analysis of laboratory experiments for plunging breaking waves by *Drazen et al.* (2008). *Romero et al.* (2012) showed (see Figure 2.1) that when combined with a threshold for breaking, this power law extends to the data for the onset of breaking from *Banner and Peirson* (2007); that is, it applies across the whole available range of breaking strength data. *Melville and Rapp* (1985) and *Rapp and Melville* (1990) measured the loss of momentum and energy fluxes from surface waves due to breaking by using dispersive focusing of a wave packet to induce unsteady, quasi-two-dimensional breaking. In particular, *Rapp and Melville* (1990, §5.4) found that for three different strengths of wave breaking (two of which were described as plunging and one as spilling) more than 90% of the energy lost by the wave field due to breaking was dissipated within four wave periods of the breaking event. Meanwhile, they found that between 58% and 86% of the momentum lost by the wave field was present in the

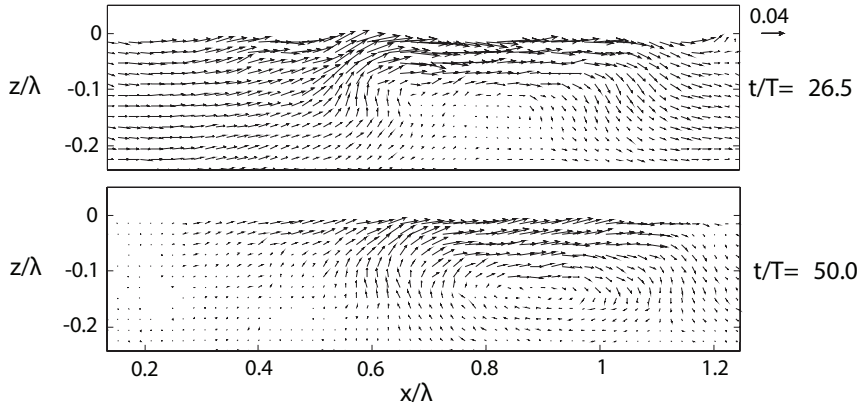

Figure 2.2: Laboratory measurements of the ensemble averaged, non-dimensionalized, velocity field induced by breaking, from Melville et al. (2002: MVW). Here, λ and T represent the characteristic wavelength and period of the breaking wave, respectively, and the vector density is reduced by a factor of 10 for clarity of presentation; see MVW for further details. The figure shown is for times $t/T = 26.5, 50$ for top and bottom plots, respectively. The main feature of the flow is a coherent vortex, which lasts for more than 50 wave periods after the breaking event and slowly propagates downstream through the action of its image in the free surface.

breaking induced currents four wave periods after the breaking event. Additionally, the authors found that the magnitudes of the induced mean and turbulent currents were comparable. *Melville et al.* (2002, hereinafter referred to as MVW) used a similar dispersive focusing technique to study the ensemble averaged flow and turbulence after the breaking event. The post-breaking flow in these studies was dominated by a robust vortex, which is displayed in Figure 2.2, lasting for more than 58 wave periods after breaking (see also *Rapp and Melville* 1990, *Sullivan et al.* 2004). MVW showed that this vortex slowly propagated downstream under the influence of its image in the free surface.

To study the effects of breaking waves on the water column, *Sullivan et al.* (2004, hereinafter referred to as SMM2004) proposed a heuristic model of a breaking wave by the use of a body force. The authors modeled this force based on laboratory experiments of *Rapp and Melville* (1990) and MVW, finding qualitative and quantitative agreement between the large scale response of the flow in the model and the (ensemble-averaged) behavior observed in the laboratory. They

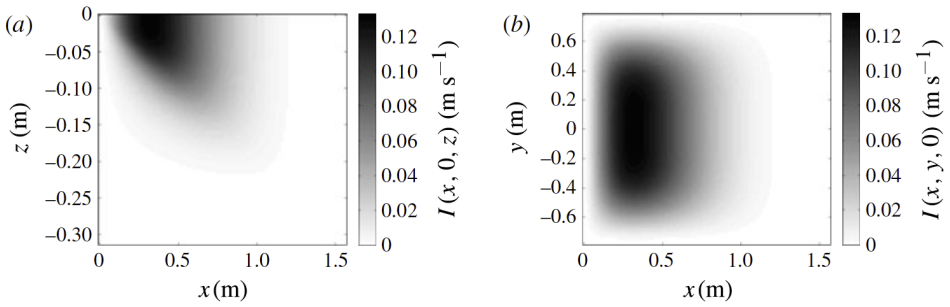

Figure 2.3: Impulse due to the body force parametrizing a breaking event. The plot on the left shows the impulse in the (x, z) plane at $y = 0$ while the plot on the right shows the impulse in the (x, y) plane at $z = 0$; based on forcing given in SMM2004, which is in the $\hat{\mathbf{x}}$ direction.

then compared the effects of the body force with a uniform surface stress of equivalent total momentum transfer, highlighting the marked impact of intermittent body forces, or breaking, on the dynamics of the water column. The impulse per unit mass, $\mathbf{I}$, imparted to a fluid by a body force per unit mass $\mathbf{F}$ is defined as

$$\mathbf{I} = \int_0^{\mathcal{T}} \mathbf{F}(\mathbf{x}, t)\, dt, \tag{2.4}$$

where $\mathcal{T}$ is the duration of the forcing event *Lamb* (1932, §119). Figure 2.3 shows the impulse of the body force, modeled after a deep water breaking wave, proposed by SMM2004. *Sullivan et al.* (2007, hereinafter referred to as SMM2007) then extended the use of their model to include an ensemble of breaking events and explored the ramifications of these impulses on the underlying dynamics, finding upper ocean processes respond strongly to the addition of wave breaking. *Restrepo et al.* (2011) used a qualitatively similar parametrization of the body force, as well as a scaling assumption that the velocity induced by the breaking is weak to analytically solve for the behavior of currents and waves in the presence of wave breaking. Note, while the effects of breaking may be weak in the mean (*Hasselmann* 1974), the velocity due to breaking is $\mathcal{O}(\mathrm{c})$ over short time scales (*Rapp and Melville* 1990).

The ability to reproduce the vortical behavior found in the laboratory (MVW) using an impulsive body force (SMM2004) implies that this is a viable

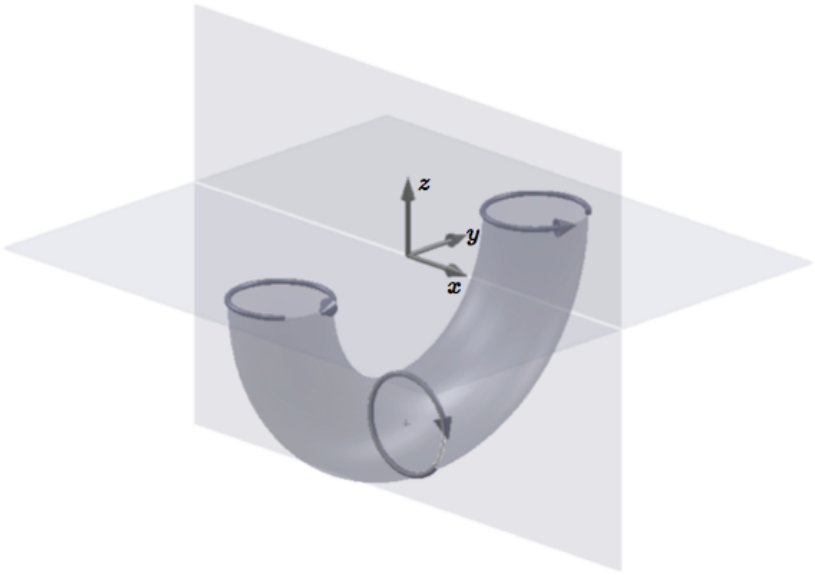

Figure 2.4: Description, proposed by *Peregrine* (1999), of the topological shape (a half vortex ring) of the flow shortly after a breaking event. The surface of the torus denotes the vortex filament and the arrows indicate the direction of the velocity.

model of wave breaking. The dynamics of impulsively forced fluids, and in particular the relationship between impulse and vorticity, is well known and in cases where the impulse has an axial symmetry, the resulting structures are known as vortex rings (see for instance, Batchelor 1967, §7.1, 7.2; Saffman 1992).

The most striking feature of the vortex ring is its robust coherence (*Shariff and Leonard* 1992). Theoretical investigations of vortex dynamics are complicated by the details of the vorticity distributions within their cores; however, for certain simple systems, closed form equations describing integral scalar quantities of the vortex ring (i.e. impulse, energy, circulation) exist (*Batchelor* 1967, §7.2). For instance, *Helmholtz* (1858) described, and *Taylor* (1953) quantified, a simple experiment to create a half vortex ring by forcing a partially submerged disk along its axis of symmetry in a fluid and then quickly removing it (see Figure 2.5).

Theoretical descriptions of vorticity generation by breaking deep-water waves have been sparse, although descriptive models have been hypothesized. *Csanady* (1994) argued that breaking will generate vertical eddies at the surface, contributing to the Craik-Leibovich II (CL II) mechanism (*Craik and Leibovich*

1976, *Leibovich* 1983) and enhancing Langmuir circulation; a suggestion supported by the numerical modeling of SMM2007. Similarly, *Peregrine* (1999) noted that Helmholtz's vorticity theorems imply that the vortex filament generated by a deep water breaking wave is topologically equivalent to a half vortex ring (see Figure 2.4). These studies, however, have stopped short of making quantitative predictions about the vorticity and circulation generated by breaking waves except in the case of shallow water, where the vorticity is bounded by the surface and the bottom (see, for instance, *Peregrine* 1998). The recent numerical efforts mentioned above have started to elucidate the importance of breaking in mixed layer processes, but many of the basic theoretical mechanisms are still unclear (*Thorpe* 2005). In this chapter we make progress in this direction by following SMM2004 and SMM2007 in assuming that the effects of a breaking wave can be modeled by an impulsively forced fluid, allowing us to find a relationship between the energy lost due to breaking and the circulation that is generated.

The organization of this chapter is as follows: In section 2.2 we introduce governing equations for a homogeneous incompressible fluid and derive from this an equation for the generated circulation. In section 2.3, we associate the forcing with the effects due to a breaking wave and make scaling arguments supporting a relationship between the circulation and the characteristic variables of a breaking wave. Next, we compare the theoretical predictions with the available laboratory data. The results are discussed in section 2.4.

2.2 The breaking circulation model

2.2.1 Governing equations

Consider an incompressible homogeneous inviscid fluid with a free surface. The governing equations (i.e. Euler's equations) are

$$\frac{D\mathbf{u}}{Dt} = -\frac{1}{\rho}\boldsymbol{\nabla} p + g\hat{\mathbf{z}}; \qquad \boldsymbol{\nabla}\cdot\mathbf{u} = 0, \tag{2.5}$$

where $\mathbf{u}$ is the fluid velocity, ρ is the density of water, g is the acceleration due to gravity, and p is the pressure.

The present study is intended to characterize the post-breaking, ensemble-average, large scale flow response to a breaking wave. To this end, we define the ensemble-averaging operator $\overline{(\ \ )}$ such that

$$\overline{\mathbf{G}(\mathbf{x},t;N)} \equiv \frac{1}{N}\sum_{n=1}^{N} \mathbf{G}(\mathbf{x},t,n), \tag{2.6}$$

where $\overline{\mathbf{G}}$ is the ensemble-average of the variable $\mathbf{G}(\mathbf{x},t,n)$, measured during the $n\text{-}th$ realization of the experiment (where each realization has identical initial and boundary conditions), with total number of repeats N. The measured fluctuating component of the variable, $\mathbf{G}'(\mathbf{x},t,n)$, is then defined as

$$\mathbf{G}'(\mathbf{x},t,n) = \mathbf{G}(\mathbf{x},t,n) - \overline{\mathbf{G}(\mathbf{x},t;N)}. \tag{2.7}$$

The true ensemble-average and fluctuating components are just the limits of equations (2.6) and (2.7) as $N \to \infty$. Note, the error associated with keeping N finite can be estimated by conducting a number of repeat realizations of the experiment and then estimating the convergence of the measured quantity as a function of N (see further discussion in §2.3.2).

Now, we decompose the breaking induced velocity $\mathbf{u}$ into mean, $\overline{\mathbf{u}}$, and fluctuating (i.e. turbulent), $\mathbf{u}'$, components, with respect to this averaging operator, so that

$$\mathbf{u}(\mathbf{x},t,n) = \overline{\mathbf{u}(\mathbf{x},t;N)} + \mathbf{u}'(\mathbf{x},t,n), \tag{2.8}$$

where, by definition, $\overline{(\mathbf{u}')} = 0$. If we substitute this decomposition into equation (2.5), and then take the ensemble-average of the resulting equation, we find (see, for instance, Pope 2000, §4):

$$\frac{\partial \overline{u_i}}{\partial t} + \frac{\partial}{\partial x_j}\left(\overline{u_i}\ \overline{u_j}\right) + \frac{\partial}{\partial x_j}\overline{\left(u_i' u_j'\right)} = -\frac{1}{\rho}\frac{\partial \overline{p}}{\partial x_i} + g\hat{x}_3, \tag{2.9}$$

where the subscript i ($i = 1, 2, 3$) denotes the $i\text{-}th$ cartesian component of a vector

(e.g. $x_1 = x,\ x_2 = y,\ x_3 = z$), summation over repeated indices is assumed, and $\overline{p}$ represents the ensemble-average pressure. Note, the averaging operator and space and time derivatives commute (see, for instance, *Kundu et al.* 2012, §12.3). For a thorough discussion of the properties of this averaging operator, see also *Andrews and McIntyre* (1978, §2). The influence of the turbulent velocity fluctuations on the mean flow is represented by the forcing associated with the Reynolds stress tensor $\overline{(u_i' u_j')}$. We note that equation (2.9) is an inviscid version of the Reynolds-averaged Navier-Stokes equations (see *Pope* 2000) with a free surface.

Now, instead of solving equation (2.9) directly, we will consider the circulation, Γ, of the ensemble-average velocity field. As will be shown below, the circulation is an integral scalar quantity governed by (an ensemble-average version of) Kelvin's circulation theorem and has established closed forms for vortex rings, which can be written solely in terms of the characteristic variables of a breaking wave.

Consider the circulation of the ensemble-average velocity field, defined as

$$\Gamma \equiv \oint_{\overline{C}} \overline{\mathbf{u}} \cdot d\boldsymbol{\ell}, \tag{2.10}$$

where $\overline{C}$ is a closed material contour moving with velocity $\overline{\mathbf{u}}$, which will be further specified below. Next, the ensemble-average total derivative is defined as

$$\frac{\overline{D}}{Dt} = \frac{\partial}{\partial t} + \overline{\mathbf{u}} \cdot \boldsymbol{\nabla}, \tag{2.11}$$

so that the evolution of equation (2.10) is then given by

$$\frac{\overline{D}\Gamma}{Dt} = \oint_{\overline{C}} \frac{\overline{D}\overline{\mathbf{u}}}{Dt} \cdot d\boldsymbol{\ell} + \oint_{\overline{C}} \overline{\mathbf{u}} \cdot \frac{\overline{D}}{Dt} d\boldsymbol{\ell}. \tag{2.12}$$

The second term on the right hand side of equation (2.12) can we rewritten as (*Batchelor* 1967, §3.1, 5.2)

$$\oint_{\overline{C}} \overline{\mathbf{u}} \cdot \frac{\overline{D}}{Dt} d\boldsymbol{\ell} = \oint_{\overline{C}} \overline{\mathbf{u}} \cdot (d\boldsymbol{\ell} \cdot \boldsymbol{\nabla}\overline{\mathbf{u}}) = \oint_{\overline{C}} \boldsymbol{\nabla} \left(\frac{\overline{\mathbf{u}} \cdot \overline{\mathbf{u}}}{2} \right) \cdot d\boldsymbol{\ell}, \tag{2.13}$$

which, by application of Stokes' theorem and the fact that the curl of the gradient of a scalar function vanishes, is identically zero.

Next, we substitute equation (2.9) into the first term on the right hand side of equation (2.12), so that we find

$$\oint_{\overline{C}} \frac{\overline{D}\overline{\mathbf{u}}}{Dt} \cdot d\boldsymbol{\ell} = \oint_{\overline{C}} \left(-\frac{\partial}{\partial x_j} \overline{\left(u_i' u_j'\right)} - \frac{1}{\rho} \frac{\partial \overline{p}}{\partial x_i} + \frac{\partial (g x_3)}{\partial x_i} \right) d\ell_i. \tag{2.14}$$

First, we note that the second and third terms on the right hand side of equation (2.14), involving the ensemble-average pressure $\overline{p}$ and the acceleration due to gravity g, will be zero because, again by Stokes' theorem, the argument of these integrals is the curl of the gradient of a scalar function, and hence zero.

Next, we perform the canonical decomposition of the Reynolds stress tensor into isotropic and deviatoric anisotropic components (see, for instance, *Pope* 2000, §4.2):

$$\overline{\left(u_i' u_j'\right)} = \left(\Pi \ \delta_{ij} + \mathcal{D}_{ij}\right), \tag{2.15}$$

where

$$\Pi \ = \frac{1}{3} \overline{(u_i' u_i')} \ = \frac{2}{3} e(\mathbf{x}, t), \tag{2.16}$$

$\Pi \ \delta_{ij}$ (with $\delta_{ij} = 1$ for $i = j$, 0 otherwise) is the isotropic (normal) stress, Π is a scalar function proportional to the turbulent kinetic energy $e(\mathbf{x}, t) \equiv \frac{1}{2} \overline{(\mathbf{u}' \cdot \mathbf{u}')}$ and $\mathcal{D}_{ij}$ is the anisotropic (shear) stress, given by

$$\mathcal{D}_{ij} = \overline{(u_i' u_j')} - \frac{2}{3} e(\mathbf{x}, t). \tag{2.17}$$

Therefore, the term related to the Reynolds stresses in the governing equation for the circulation, i.e. equation (2.14), is equivalent to

$$\oint_{\overline{C}} -\frac{\partial}{\partial x_j} \overline{\left(u_i' u_j'\right)} d\ell_i = \oint_{\overline{C}} -\frac{\partial}{\partial x_j} \left(\Pi \ \delta_{ij} + \mathcal{D}_{ij}\right) d\ell_i. \tag{2.18}$$

The contour integral of the normal component of the Reynolds stress tensor, $\boldsymbol{\nabla}\Pi$, will be zero, which again can be seen by application of Stokes' theorem and noting that the curl of the gradient of a scalar function vanishes, so that equation

(2.18) reduces to

$$\oint_{\overline{C}} -\frac{\partial}{\partial x_j}\overline{\left(u_i' u_j'\right)} d\ell_i = \oint_{\overline{C}} -\frac{\partial \mathcal{D}_{ij}}{\partial x_j} d\ell_i. \tag{2.19}$$

Now, the laboratory studies under consideration in this chapter use dispersive focusing of compact unidirectional wave groups to induce unsteady quasi two-dimensional breaking waves. For times much less and much greater than the time at which breaking occurs, the wave groups are accurately described by linear theory, which predicts that the momentum transported by these wave packets is solely in the direction of wave propagation (see, for instance, *Phillips* 1977, §3), which throughout this work is along the x-axis.

That is, if $\boldsymbol{\mathcal{M}}^o(\mathbf{x}, t \ll t_b) = \mathcal{M}^o(\mathbf{x}, t \ll t_b)\ \hat{\mathbf{x}}$, where t_b represents the time at which the breaking event occurs, is the momentum in the wave field before breaking, and $\boldsymbol{\mathcal{M}}^f(\mathbf{x}, t \gg t_b) = \mathcal{M}^f(\mathbf{x}, t \gg t_b)\ \hat{\mathbf{x}}$ is the momentum in the wave field after breaking, the difference $\Delta\boldsymbol{\mathcal{M}} = (\mathcal{M}^o - \mathcal{M}^f)\hat{\mathbf{x}}$ is transferred to the water column by the breaking process. Note, as mentioned in the introduction, some of the momentum lost from the wave field due to breaking will go into other phenomena besides current generation. See §2.4 for further discussion (see also SMM2004, §4; SMM2007, §3). If the breaking event occurs for a time $\mathcal{T}$, then we see that $\Delta\boldsymbol{\mathcal{M}}/\mathcal{T}$ represents the average force exerted by the breaking wave on the water column during the breaking event. Now, the details of the momentum loss from the wave field are unknown *during* the highly nonlinear breaking process, where locally, vertical exchanges of momentum can occur. However, by the above arguments, the average forcing corresponding to the change in the wave packet's momentum is entirely in the direction of wave propagation.

Furthermore, during the breaking process the exact form of the Reynolds stress tensor is unknown, so that we must choose how to *close* these equations. Note, *after* the breaking event, the turbulent Reynolds stresses due to quasi two-dimensional breaking deep-water waves have been reported by, for instance, *Rapp* (1986), *Melville et al.* (2002), *Drazen and Melville* (2009). These studies find that for times after the breaking event, these stresses lead to a weak downward transport of positive horizontal momentum. Based on the above discussion of the momentum lost by the wave field, we will assume that mean flow induced during the breaking

event is solely in the direction of wave propagation, so that the forcing, associated with the shear Reynolds stresses of the breaking induced turbulent velocities, also acts along the x-axis.

Therefore, we parametrize the forcing terms, related to the shear Reynolds stresses in our governing equation for the mean flow, i.e. equation (2.19), as

$$\oint_{\overline{C}} -\frac{\partial \mathcal{D}_{ij}}{\partial x_j} d\ell_i \equiv \oint_{\overline{C}} \overline{F}\delta_{i1} d\ell_i, \tag{2.20}$$

where the anisotropic stress term is related to the body force $\overline{\mathbf{F}}$, with $\overline{\mathbf{F}} = \overline{F}\hat{\mathbf{x}}$.

Therefore, the governing equation for the circulation reduces to

$$\frac{\overline{D}\Gamma}{Dt} = \frac{\overline{D}}{Dt}\oint_{\overline{C}} \overline{\mathbf{u}} \cdot d\boldsymbol{\ell} = \oint_{\overline{C}} \overline{\mathbf{F}} \cdot d\boldsymbol{\ell}, \tag{2.21}$$

which is an inhomogeneous form of Kelvin's circulation theorem, describing the evolution of the circulation of the ensemble-average flow generated by the body force $\overline{\mathbf{F}}$, where the body force will model the bulk scale effects of a breaking wave on the water column. Note, a body force acting on a fluid with a free surface can lead to the generation of both waves and vortices (see, for instance, *Bühler* 2007). Post-breaking flow is analyzed in the laboratory experiments of *Rapp and Melville* (1990) and MVW, where wave breaking is due to compact wave groups, which focus, break and then propagate away. Based on this we can assume that after the breaking event, in the compact region where the forcing occurred and beyond, the free surface effectively acts like a rigid lid (see also SMM2004).

To accurately model the long time evolution of the flow one must also include effects due to viscosity. However, we note that the laboratory experiments of MVW (see their Figure 14) show that circulation decreases by less than an order of magnitude for a time interval of more than 50 wave periods after breaking.

2.2.2 Vortex generation

The exact functional form of the ensemble-average body force $\overline{\mathbf{F}}$ cannot be resolved, but following SMM2004, can be guided by laboratory data. We assume

that the body force is compact in space and time, and is symmetric, about $y = 0$, along the crest of the breaking wave (see Figure 2.3). It is natural to then consider the simple model proposed by *Helmholtz* (1858, see also *Tait* 1867), and quantified by *Taylor* (1953, see also Saffman 1992, §6.4), in which a half vortex ring is generated by impulsively forcing a thin disk, half submerged, through a perfect fluid with no flow separation. Breaking waves may have an asymmetry between the horizontal and vertical scales, so that a generalization of Taylor's (1953) work to elliptical vortex rings, by *Dhanak and Bernardinis* (1981), is more applicable to our study. Elliptical vortex rings can be generated by slightly modifying the thought experiment of *Helmholtz* (1858) to consider the flow generated by impulsively forcing a thin *elliptical* disk, submerged along its major axis to the depth of its semi-minor axis, through a fluid.

More precisely, we assume the forcing, $\overline{\mathbf{F}}$, acts like a thin elliptical disk submerged along its major axis, of length $2A$, to the depth of its semi-minor axis, of length B, being impulsively forced from rest to a speed U in a perfect fluid (see Figure 2.5) with no flow separation. This problem was considered by *Dhanak and Bernardinis* (1981) in their work on elliptical vortex rings. Note, *Dhanak and Bernardinis* (1981) found that elliptical vortex rings will oscillate in shape as they propagate, and for cases where the vortex ring has large eccentricity, can potentially break-up into multiple rings. The time scale of these oscillations is on the order of $4\pi A^2/\Gamma$, where we recall A is the semi-major axis of the elliptical vortex and Γ is its circulation. For the laboratory experiments considered in this chapter, $4\pi/\Gamma$ is on the order of $10^2\ m^{-2}s$ (see §2.3) while A is taken to be large, so that the time scale of these oscillations is much much larger than the times in which we are interested in describing the circulation. They find that the velocity potential at the surface of the disk is:

$$\phi(x = 0^{\pm}, y, z) = \mp \frac{U\mathrm{B}}{\mathcal{E}(e)} \sqrt{1 - \frac{y^2}{A^2} - \frac{z^2}{B^2}}, \tag{2.22}$$

where $\pm$ refers to the front and rear of the disk, respectively; e is the eccentricity

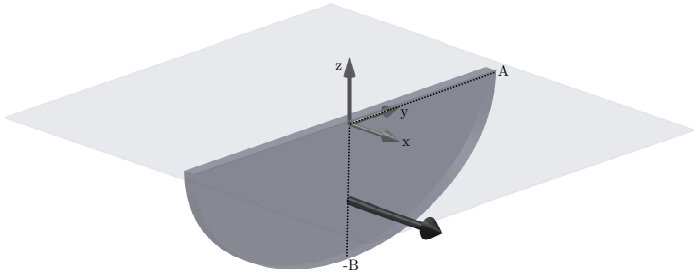

Figure 2.5: Sketch of a thin elliptical half disk of major axis length $2A$ and minor axis length $2B$ being forced from rest to a velocity $U\hat{\mathbf{x}}$ through a fluid with surface at $z = 0$. $z < 0$ corresponds to water while $z > 0$ corresponds to air.

and $\mathcal{E}(e)$ is the complete elliptic integral of the second kind:

$$\mathcal{E}(e) = \int_0^{\frac{\pi}{2}} \sqrt{1 - e^2 \sin^2\theta}\; d\theta; \qquad e^2 \equiv \frac{A^2 - B^2}{A^2}. \tag{2.23}$$

The circulation around a contour starting at $(x, y, z) = (0^+, 0, 0)$ and ending at $(0^-, 0, 0)$ is given by (*Dhanak and Bernardinis* 1981)

$$\Gamma = \phi(0^-, 0, 0) - \phi(0^+, 0, 0) = \frac{2UB}{\mathcal{E}(e)}. \tag{2.24}$$

Following *Taylor* (1953), we assume the disk is suddenly dissolved, so that the induced motion may now be described as being due to a collection of elliptic vortex lines, with axis ratios the same as that of the disk, over the plane of the disk. From (2.22) it is clear that the velocity is strongest at the edge of the disk, implying that the flow will tend to roll up around this region (see also *Saffman* 1992, §6.3, 8.4), forming an elliptical vortex ring.

We assume the rolling up of the vortex sheet will not change the circulation

around the core (*Taylor* 1953, *Saffman* 1992) so that the circulation of the generated vortex ring will be the same as the circulation of the forced disk, as given in (2.24).

2.3 Circulation of breaking waves

Vortex lines must start and end on the boundaries, or be closed loops within the fluid. This implies that for three-dimensional deep-water breaking waves the distribution of vorticity must be topologically equivalent to a half vortex ring, since the vortex lines induced by the event will not reach the bottom (*Peregrine* 1999, *Csanady* 1994, *Thorpe* 2005, see also Figure 2.4). Note that in two dimensions the vorticity induced by breaking takes a form such that the kinematics can be described by those of a point vortex, which is a limiting case of the three dimensional vortex ring as $A \to \infty$ with B finite (see Figure 2.2; *Rapp and Melville* 1990, *Melville et al.* 2002). Along with the considerations of the structure of the impulse due to breaking discussed in §2.2, we now see that there is a direct relationship between the flow response to an impulsively forced thin disk moving through a fluid and that due to a breaking wave. Therefore, we are in a position to apply the relationship established in (2.24), between the circulation and the characteristic variables of the forced disk, to the problem of wave breaking.

Now, from the laboratory experiments of *Rapp and Melville* (1990), and the scaling arguments of *Drazen et al.* (2008), we expect the variables parametrizing the forced disk to be related to those describing a breaking wave; but precisely how is not immediately clear. In order to make progress, we turn to scaling arguments.

2.3.1 Scaling of circulation

We present two separate scaling arguments to quantify, to within a constant, the circulation induced by a breaking wave. First, we will make a scaling argument based on dynamical considerations relating the momentum lost from the wave field due to breaking to the variables describing the generated vortex. Second, we make scaling arguments based on the geometry and kinematics of both

a plunging and spilling breaking wave.

Scaling based on dynamical considerations

A fully three-dimensional breaking wave will start to break at a point in space and subsequently this breaking spreads along the length of the crest of the breaking wave, with associated time scale τ. We assume that this occurs on a much faster time scale than the wave period, T, of the breaking wave (i.e. $\tau \ll T$), so that following SMM2004, the crest length is taken to be constant. Finally, we assume the initial depth of penetration of a breaking wave is generally much smaller than the resulting length scale of the crest; that is, $A \gg B$, so that $\mathcal{E}(e) \approx 1$ in (2.24):

$$\Gamma \approx 2UB. \tag{2.25}$$

Note, as mentioned above we are assuming the circulation is conserved during the roll-up process, so that equation (2.25) is also the circulation of the vortex generated by the impulsive event.

The fluid impulse $\mathcal{P}$ (Batchelor 1967, §7.2), associated with the flow of the forced elliptical disk presented in §2.2 is given by (Dhanak and Bernardinis 1981)

$$\mathcal{P} = \frac{2\pi\rho AB^2U}{3\mathcal{E}(e)}, \tag{2.26}$$

where the variables are as defined in that section (see also Figure 2.5). Accounting for the above assumption that the major axis of the disk is much larger than the minor axis, (2.26) reduces to

$$\mathcal{P} = \rho\frac{2\pi AB^2U}{3}. \tag{2.27}$$

Comparing this to (2.25), we see that

$$\Gamma = \frac{1}{\rho}\frac{3\mathcal{P}}{2\pi AB}. \tag{2.28}$$

By considering the reduction of energy and momentum densities of the wave field due to breaking, the total energy lost by a breaking event per unit length of breaking crest is given by (*Phillips* 1985, *Sullivan et al.* 2007)

$$E_l = cM_l, \tag{2.29}$$

where M_l is the total momentum loss per unit length of breaking crest and c is the phase speed of the breaking wave. E_l is related to the energy dissipation rate per unit length of breaking crest ϵ_l by

$$E_l = \int_0^{\mathcal{T}} \epsilon_l \, dt, \tag{2.30}$$

where the $\mathcal{T}$ is a constant of $\mathcal{O}(T)$ (*Rapp and Melville* 1990, *Sullivan et al.* 2004, 2007), T is the period of the breaking wave, and the energy dissipation rate ϵ_l is given by equations (2.1) and (3.1), that is (*Drazen et al.* 2008):

$$\epsilon_l = \beta \frac{(hk)^{\frac{5}{2}} \rho c^5}{g}. \tag{2.31}$$

Now, the loss of momentum from the wave field will go into the generation of the rotational flow under consideration (*Rapp and Melville* 1990, §5.4), which implies that M_l can be related to the impulse of the forced disk $\mathcal{P}$:

$$\mathcal{P} = \int M_l dy = \int \int_0^{\mathcal{T}} \frac{\epsilon_l}{c} \, dt \, dy, \tag{2.32}$$

where the last equality comes from equations (2.29), (2.30) and (2.31), and the spatial integrals are over the entire region where the forcing acts.

Based on *Rapp and Melville* (1990), we assume the semi-minor axis of the disk B scales with the depth of the penetration of the fluid, and hence the height of the wave at breaking h. Also, we assume that the major axis of the elliptical disk $2A$ scales with the crest length of the breaking wave.

Therefore, substituting (2.31) into (2.32) and equating with (2.28), we find

$$\Gamma \sim (hk)^{\frac{3}{2}} c\lambda \sim (hk)^{\frac{3}{2}} \frac{c^3}{g}, \tag{2.33}$$

where the linear dispersion relation was used to rewrite the wavelength in terms of the phase speed and the gravitational constant. From (2.33) we conclude

$$\Gamma = \varpi \frac{(hk)^{\frac{3}{2}} c^3}{g}, \tag{2.34}$$

where ϖ is a constant. Recall, the forced disk corresponds to the ensemble-average body force model $\overline{\mathbf{F}}$, so that Γ is the generated circulation corresponding to the ensemble-averaged velocity field $\overline{\mathbf{u}}$, i.e. equation (2.10). Therefore, to within a scaling constant, we have described this circulation in terms of the characteristic variables of the breaking wave.

Plunging breaking waves

Next, we present scaling arguments for the generation of circulation by both plunging and spilling quasi-two-dimensional breakers, using models based on the geometry and kinematics of breaking. This follows the work of *Melville* (1994) and especially *Drazen et al.* (2008), who hypothesized and tested a functional form of the breaking parameter b, equation (3.1), based on an inertial model for *plunging* breakers. *Romero et al.* (2012) then showed that by introducing a threshold slope for breaking, these results held over the available laboratory data extending from the onset of weak breaking to very strong plunging breaking waves (see Figure 2.1).

We assume that the plunging breaker has amplitude a and height at breaking h (see Figure 2.6a), the toe of the breaking wave follows a ballistic trajectory once it begins to form and has velocity $w = \sqrt{2gh}$ at impact with the water (*Drazen et al.* 2008). Before breaking, the flow is irrotational, with vorticity being introduced when the toe of the breaker reconnects with the surface (*Hornung et al.* 1995).

Inertial scaling of the vorticity just after the breaking event implies $\omega = \zeta \tilde{u}/\tilde{l}$

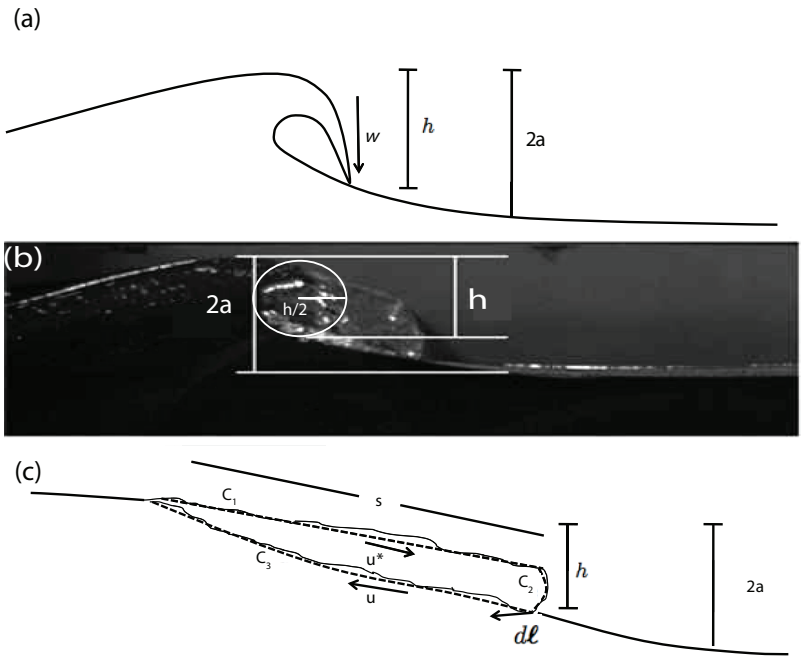

Figure 2.6: Schematic of (a) the geometry of a plunging breaker, following *Drazen et al.* (2008) where w is the velocity of the toe of the breaker as it penetrates the water and (b) a video frame of a plunging breaking wave as the toe connects with the surface, adapted from *Drazen et al.* (2008), where we see the turbulence cloud corresponding to the vorticity induced by the breaking, i.e. the dashed white circle, has the approximate cross section $\pi h^2/4$. (c) shows a spilling breaker based on *Longuet-Higgins and Turner* (1974): u^* and u denote the velocity of the whitecap and underlying motion due to the wave, respectively, in a reference frame moving at the phase speed of the breaking wave and s is the downslope distance as measured from the crest of the wave. The dashed lines represents the contour of integration C with tangent vector $d\boldsymbol{\ell}$. See the text for details. In (a)-(c), a and h represent the amplitude and height of the breaking wave.

where ω is the magnitude of vorticity, $\tilde{u}$ and $\tilde{l}$ are the characteristic velocity and length scales of the flow, respectively, and ζ is a constant parameter of order unity. Drazen et al. (2008) assumed the velocity scale is set by $w = \sqrt{2gh}$, the length scale by h and the area of the cloud of turbulence induced by the breaking, $\mathcal{A}$, is $\frac{1}{4}\pi h^2$ (see Figure 2.6a and 2.6b; see also Figure 2.3 in *Drazen et al.* 2008).

Now, we are interested in finding the circulation of the ensemble-average velocity field, which we recall is given by equation (2.10):

$$\Gamma = \oint_{\overline{C}} \overline{\mathbf{u}} \cdot d\boldsymbol{\ell} = \int_{\overline{\mathcal{A}}} \overline{\boldsymbol{\omega}} \cdot d\boldsymbol{\mathcal{A}} \tag{2.35}$$

where the second equality is from Stokes' theorem, $\overline{\boldsymbol{\omega}} \equiv \boldsymbol{\nabla} \times \overline{\mathbf{u}}$ and $\overline{\mathcal{A}}$ is the area bounded by $\overline{C}$.

Recall, *Rapp and Melville* (1990, §5) found that the mean and turbulent velocities induced by wave breaking had comparable magnitudes, so that we assume the generated ensemble-average velocity is of the same order as the integral velocity scale, w, used by *Drazen et al.* (2008). Furthermore, *Rapp and Melville* (1990, §4.3) found that the deviation in the area of mixing of the broken fluid, for an individual realization of a breaking event, was within an order one constant of the ensemble-average value. This implies that the mean area of entrainment induced by the breaking event $\overline{\mathcal{A}}$ is of the same order as the turbulent cloud used by *Drazen et al.* (2008), $\mathcal{A}$. Therefore, equation (2.35) becomes

$$\Gamma = \int_{\overline{\mathcal{A}}} \overline{\boldsymbol{\omega}} \cdot d\boldsymbol{\mathcal{A}} \sim \int_{A} \omega \; d\mathcal{A} = \zeta \frac{\pi}{4} h \sqrt{2gh}, \tag{2.36}$$

so that, using the linear dispersion relation, we find

$$\Gamma = \alpha \frac{(hk)^{\frac{3}{2}} c^3}{g}, \tag{2.37}$$

where α is a constant. This result, up to the scaling constant, is in accordance with (2.34).

Spilling breaking waves

Spilling breakers appear to be markedly different from their plunging counterparts; nevertheless, an analogous scaling model can be constructed to find a functional form for the circulation. *Longuet-Higgins and Turner* (1974) modeled a spilling breaker as a steady turbulent gravity current riding down the forward fixed slope of the underlying breaking wave, and assumed the flow remained similar as it developed in time. Although this theory is formulated for steady motion, it was shown to approximately describe both the acceleration of the front of an unsteady spilling breaker, as well as the geometry of the breaking region (*Longuet-Higgins and Turner* 1974, §6,7, see also *Duncan* 2001), prompting its use as a possible model describing the geometry and kinematics of an unsteady spilling breaking wave.

Longuet-Higgins and Turner (1974) proposed that the speed along the slope, in a reference frame moving with the phase speed of the breaking wave, is $u^* = U^*\sqrt{gs'}$ and $u = U\sqrt{gs'}$ for the whitecap and underlying fluid, respectively. U^* and U are constants and $s' \in (0, s)$ represents the distance downslope from the crest of the wave, where s is proportional to h, the height of the breaking wave (see Figure 2.6c).

Now, the scaling of the ensemble-average velocity, and area of entrainment of the broken fluid, discussed in the section on plunging breaking waves were also observed by *Rapp and Melville* (1990) to be true for spilling breaking waves. Therefore, we assume that the mean induced velocity $\overline{\mathbf{u}}$ scales with the total induced velocity $\mathbf{u}$ and that the mean contour $\overline{C}$ scales with C, so that

$$\Gamma = \oint_{\overline{C}} \overline{\mathbf{u}} \cdot d\boldsymbol{\ell} \sim \oint_{C} \mathbf{u} \cdot d\boldsymbol{\ell}. \tag{2.38}$$

Assuming the whitecap remains thin (*Longuet-Higgins and Turner* 1974) and the velocity along the front remains finite, the circulation generated along C_2 will be small compared to the contributions along C_1 and C_3, so that the circulation

around the contour, $C = C_1 + C_2 + C_3$, is approximated by

$$\Gamma = \oint_{\overline{C}} \overline{\mathbf{u}} \cdot d\boldsymbol{\ell} \sim \oint_{C} \mathbf{u} \cdot d\boldsymbol{\ell} \approx \int_{C_1} \mathbf{u} \cdot d\boldsymbol{\ell} \; + \int_{C_3} \mathbf{u} \cdot \; d\boldsymbol{\ell} \tag{2.39}$$

$$= \int_0^s U^* \sqrt{gs'} \; ds' + \int_s^0 U \sqrt{gs'} \; ds' = \frac{2}{3}(U^* - U)\sqrt{gs^3}, \tag{2.40}$$

to give

$$\Gamma = \varkappa \frac{(hk)^{\frac{3}{2}} c^3}{g}, \tag{2.41}$$

where we have again used the linear dispersion relationship and $\varkappa$ represents a constant of proportionality. We note that a similar argument, based on this model, gives the same functional form of the energy dissipation rate found by *Drazen et al.* (2008) for plunging breaking waves, that is, equation (2.31).

As was discussed in §2.2, we assume the circulation imparted by the breaking will be conserved, so that the above relationships will describe the circulation of the post breaking flow. Therefore, we conclude that (2.34), (2.37) and (2.41) are all equivalent, up to a scaling constant, and characterize the generated circulation, corresponding to the ensemble-average velocity, for both spilling and plunging breakers, based on the characteristic variables of the breaking wave.

It should be noted that a simpler dimensional analysis argument, in the spirit of *Drazen et al.* (2008), can give us this same functional form for the circulation by assuming that it is a function of only gravity and the height of the breaking wave; namely, $\Gamma = \Gamma(g, h)$.

Through the wave slope at breaking hk, we can find a connection between the wave energy dissipation and the circulation. To this end, equating (2.34), (2.37) or (2.41) with (2.31), we have

$$\Gamma = \frac{\Xi}{g} \left(\frac{g\epsilon_l}{\rho} \right)^{\frac{3}{5}}, \tag{2.42}$$

where Ξ is a constant of proportionality. This simple relationship establishes a con-

nection between the wave energy dissipated by a breaking event and the resulting circulation.

2.3.2 Comparison with laboratory studies

We now compare our model with the limited available laboratory data. The main features of the laboratory experiments, consistent with this study, are shown in Table 2.1 and we refer the reader to the original papers for full details on the experimental techniques and laboratory configurations. The accessible laboratory experiments were conducted for quasi-two-dimensional breaking waves using a dispersive focusing technique, with breaking strength ranging from spilling to plunging. The studies under consideration also employed a technique to obtain spatial measurements of the induced velocity field, thus allowing for the calculation of the circulation generated by a breaking wave. For each experiment, an ensemble of runs (between 10 and 20 depending on the study) were conducted for a fixed set of initial wave parameters.

We consider the circulation of the vortex generated by the breaking wave, corresponding to the ensemble-averaged velocity field, at the earliest measured time after the breaking event (c.f equation (2.21)). Also, in order to obtain a consistent comparison amongst the different experiments, we sought to calculate the circulation at a common time after the breaking event. This occurred for times in the interval $\tilde{t} \in [3, 4]$, where $\tilde{t} \equiv t/T_c$ (T_c is the centre period of the input wave group), after the breaking event, with the specific time dependent on the available data from the experiment in question (see Table 2.1). Recall, *Rapp and Melville* (1990) found that four wave periods after the breaking event, more than 90% of the energy lost by the wave field had been dissipated, while most of the momentum lost by the wave field was in the breaking generated mean flow.

Rapp and Melville (1990), *Rapp* (1986) used a laser doppler anemometer to measure the velocity field of the flow induced by breaking. The three cases from these experiments include both spilling and plunging breaking waves (see Table 2.1). Each breaking scenario was repeated 10 times (the authors reported negligible differences between the mean velocity for 10 repeats versus 40 repeats).

Table 2.1: Summary of relevant laboratory experiments and wave parameters for the circulation generated by quasi-two-dimensional breaking waves, with quantities as given in the original papers, used to test the model for circulation generated by breaking, i.e. (2.43). S is as defined in (2.2) while f_c represents the centre frequency of the input wave packet. RM, DM and Rapp correspond to *Rapp and Melville* (1990), *Drazen and Melville* (2009), *Rapp* (1986), respectively, and all other names are as denoted in the text. Notice, the available data includes both plunging and spilling breaking waves.

Experiment	S	Description	f_c	Ensemble size	Time after breaking
RM	0.278	Spilling	0.88	10	4
RM	0.352	Plunging	0.88	10	4
MVW	0.320	Plunging	0.99	15	3
DM	0.360	Plunging	1.08	20	3.42
Rapp	0.420	Plunging	1.28	10	4

The original data from these laboratory experiments is unavailable, so that a description of the circulation was inferred from the published figures depicting the ensemble average velocity field induced by breaking (specifically figures 43b and 45b in *Rapp and Melville* 1990 and figure 5.3.6b in *Rapp* 1986). In particular, the average velocity along each segment of a rectangular contour, encompassing the vortex in question, was computed, from which the circulation was estimated.

Next, the laboratory experiments of MVW (see also *White* 1996) used digital particle image velocimetry (DPIV) to measure the velocity field induced by a plunging breaking wave. The authors found that the mean square velocity rapidly converged over an ensemble of events (see their figure 2.4), so that the mean square velocity of a 15 member ensemble had a relative error of approximately 2% compared to a total sample size of 24 repeats. The authors then computed the circulation, corresponding to the ensemble average of 15 repeats, of the induced vortex three wave periods after the breaking event (see their figure 5).

Finally, *Drazen and Melville* (2009) used a similar DPIV technique to analyze properties of the flow induced by a plunging breaking wave. Drazen (personal communication) has provided us with archived data of 20 repeats of the velocity field induced by breaking from the study of *Drazen and Melville* (2009, see their figure 2). Following the analysis of MVW, for each realization we compute the circulation around a closed rectangular contour that encompasses

the vortex under consideration. We find that the circulation (non-dimensionalized by g/c^3) corresponding to the ensemble averaged velocity field is 0.152, with a standard deviation of 0.022, which also corroborates the assumptions made to derive equation (2.37). This is shown in the error bar in Figure 2.7.

Now, equation (2.34), (2.37) or (2.41) implies that the (non-dimensional) circulation is

$$\Gamma \frac{g}{c^3} = \mathcal{C}(hk)^{\frac{3}{2}}, \tag{2.43}$$

where $\mathcal{C}$ is a constant. Based on the laboratory results of *Banner and Peirson* (2007, Appendix B, see also *Rapp and Melville* 1990) and the analysis of *Drazen et al.* (2008, §5), we assume that the characteristic speed of the breaking wave is given by the phase speed of the centre frequency of the input wave packet. Next, as mentioned in the introduction, and following *Drazen et al.* (2008), instead of using the slope at breaking hk, which depends on nonlinear processes leading up to breaking, we consider the maximum predicted linear slope at breaking S, since this parameter is known a priori. Following *Romero et al.* (2012), a slope threshold and scaling factor for S were introduced and obtained by a least squares fit with the data, giving

$$\Gamma \frac{g}{c^3} = 0.85(S - 0.058)^{\frac{3}{2}}. \tag{2.44}$$

Figure 2.7 shows a comparison between the model described in equation (2.44) with the data given in Table 2.1. Although only a limited amount of data is available, the relative agreement with the model is encouraging.

2.4 Discussion

We have proposed a simple relationship for the ensemble-averaged circulation generated by breaking deep-water surface gravity waves as a function of the characteristic variables of the breaking wave. Through scaling arguments, we also clarify why the form of the governing equation for energy dissipation rate, as well

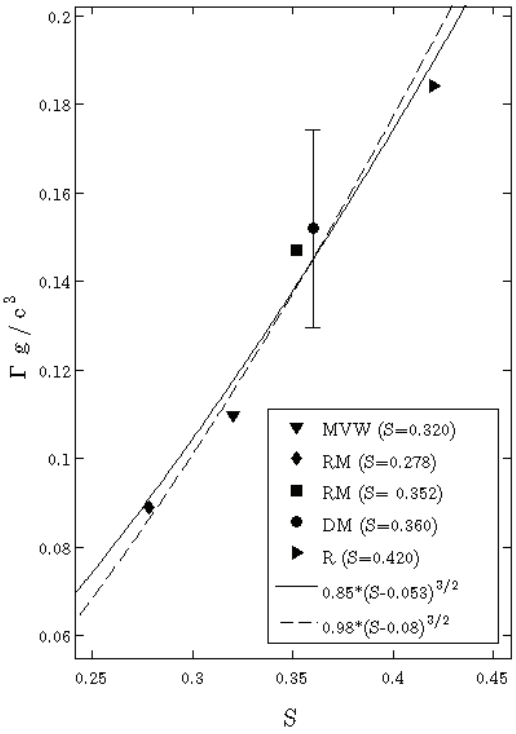

Figure 2.7: Comparison of normalized circulation versus maximum linear slope at breaking S for the available laboratory data, which includes both spilling and plunging breaking waves. The sources of data in the legend are explained in Table 2.1. The error bar on the DM data denotes the standard deviation of individual realizations versus the 20 member ensemble average. The solid line is given by equation (2.44) while the dashed line is based on the breaking strength parameter b, from *Romero et al.* (2012), and is given by equation (2.46). See text for more details.

as the generated circulation, should hold over the entire range of breaking, that is for both plunging and spilling breaking waves.

Note, *Romero et al.* (2012, their equation 24, see also Figure 2.1) found, via a visual fit, that the parameters that best fit, with respect to the available laboratory data for the energy dissipation rate per unit length of breaking crest, the model of *Drazen et al.* (2008) was $b(S) = 0.4(S - 0.08)^{\frac{5}{2}}$. Substituting this relation into equation (2.31), and subsequently equation (2.42), gives

$$\Gamma \frac{g}{c^3} = 0.58\Xi(S - 0.08)^{\frac{3}{2}}. \tag{2.45}$$

A least squares fit of Ξ with the laboratory data gives $\Xi \approx 1.64$, so that

$$\Gamma \frac{g}{c^3} = 0.98(S - 0.08)^{\frac{3}{2}}, \tag{2.46}$$

which is displayed by the dashed line in Figure 2.7. Note, the scaling factor Ξ is of order unity, and not inconsistent with the $\mathcal{O}(1)$ scaling of constants in equations (2.34), (2.37) and (2.41).

It should also be noted that energy and momentum lost from the wave field to the water column due to breaking will go into other phenomena besides that which explicitly creates the large scale flow that is analyzed in this chapter. Principal amongst these is the work done against the buoyancy force associated with bubble entrainment. *Lamarre and Melville* (1991) found that up to half of the energy lost to the water column may be expended this way. However, they also found that the proportion of maximum volume entrained versus total energy lost due to breaking scales with the characteristic variables of the breaking wave. This implies that we can absorb these effects into the constant of proportionality, Ξ, relating circulation and wave energy dissipation in equation (2.42), just as they are included in the dissipation data of Figure 2.1. Also, breaking waves will generate both currents and *waves* (*Bühler* 2007); however, these waves were measured in the case of a plunging breaking wave by *Rapp and Melville* (1990, §3.5) and found to contain less than 1% of the energy of the main packet. Furthermore, the contributions of irrotational waves to the contour integral of the instantaneous

forcing function in equation (2.10) is zero. We note that although these effects were not explicitly taken into account in the scaling argument of *Drazen et al.* (2008), these phenomena are inherent in the laboratory studies used to corroborate the scaling model, shown in Figure 2.1 (see also *Romero et al.* 2012).

Measurements of dissipation due to turbulence associated with breaking waves in the field are now available (see, for instance, *Romero et al.* 2012, *Sutherland and Melville* 2013), so that using the results in this chapter one could potentially estimate the circulation imparted to the underlying surface currents. Also of interest for application in the field is the description of the vertical vorticity at the surface, which can now be measured in the ocean (*Veron et al.* 2009, *Sutherland and Melville* 2013), and has been hypothesized to seed the so-called CL II instabilities leading to Langmuir circulations (*Csanady* 1994, *Sullivan et al.* 2007), an important feature of upper ocean dynamics. We note that in the absence of outside forcing, the circulation predicted by (3.1) is invariant along the core. This implies that surface signatures of vorticity can be proxies for the vorticity and mixing at depth, a result which could be used to corroborate the estimate of generated circulation based on the energy dissipated by breaking waves.

The text in chapter 2 is a reprint of the material as it appears in Pizzo, N.P. and Melville, W.K. (2013), Vortex generation by deep-water breaking waves, *Journal of Fluid Mechanics*, **734**, p.p. 198-218.

3 Current generation by deep-water breaking waves

3.1 Introduction

The flow induced by deep-water wave breaking is characterized by the generation of turbulence, and a coherent vortex associated with the mean flow. In the case of quasi-two-dimensional breaking, it is a line vortex ending at the lateral boundaries of the flow (*Rapp and Melville* 1990, *Melville et al.* 2002, *Pizzo and Melville* 2013). For three-dimensional deep-water breaking it is a half vortex ring with dipolar vorticity at the surface (*Peregrine* 1999). Vortex rings are defined by their integral properties (*Linden and Turner* 2001), so that we can connect the circulation in this breaking-induced half-ring vortex with the hydrodynamical impulse necessary to generate it (*Lamb* 1932). By connecting this impulse with the momentum (and subsequently the energy) lost from the wave field due to breaking, we can describe the energy in the mean flow vortex in terms of the characteristic variables of the breaking wave, and obtain a simple model for the ratio of the energy in the breaking induced current to the total energy lost by breaking. That is the focus of this chapter.

Breaking waves transfer momentum and energy from the quasi-irrotational surface wave field to the rotational underlying currents (*Phillips* 1977, *Melville* 1996). A better understanding of this process is crucial for an improved description of air-sea interaction, especially for coupled ocean-atmosphere models (*Cavaleri et al.* 2012). Breaking waves, however, are two-phase turbulent flows, making detailed theoretical analysis very difficult. Therefore, numerical and laboratory

studies are invaluable for gaining knowledge about these processes. Based on fundamental fluid dynamics and experiments, simple scaling models can be developed and are useful for understanding the physics of the observed integral properties of the breaking-induced flow.

Drazen et al. (2008) studied the breaking strength parameter b, associated with the energy dissipation rate per unit length of breaking crest ϵ_l (see also *Duncan* 1981, *Phillips* 1985) and based on an scaling model for plunging breaking waves, they found

$$\epsilon_l = b\frac{\rho c^5}{g}; \qquad b = \beta(hk)^{\frac{5}{2}}, \tag{3.1}$$

with ρ the density of water, c the phase velocity, h the height of the wave at breaking, k the wavenumber and β an order-one scaling constant. The first relationship in equation (3.1) was proposed by *Duncan* (1981, see also *Phillips* (1985)), but b was taken to be a constant. *Drazen et al.* (2008) then extended this relationship to account for the dependence of b on the local slope at breaking.

Based on this work, *Romero et al.* (2012) compared the model given in equation (3.1) with existing laboratory data by equating b with the maximum slope (according to linear theory) at breaking, S, along with a threshold for breaking S_0; that is, $b = \beta(S - S_0)^{\frac{5}{2}}$. (Note, *Drazen et al.* (2008, figure 15) found $(hk) \approx S$ to within the scatter of the data.) Excellent agreement with the existing laboratory data was found, with b ranging over three orders of magnitude, which included both gently spilling and plunging breaking waves (*Drazen et al.* 2008, see also *Romero et al.* 2012, *Grare et al.* 2013). The agreement of the model with measurements of the dissipation of gently spilling breaking waves was surprising, as the scaling argument used to derive the model was based on the geometry of a plunging breaking wave. This prompted *Deike et al.* (2015) to numerically examine the energy dissipation rate of gravity-capillary waves using a direct numerical simulation of the two-phase Navier-Stokes equations. They found that the model continued to agree with the data, even for waves that were dissipating energy mostly through the formation of parasitic capillary waves.

Next, we recall that a coherent vortex characterizes the wave breaking induced ensemble-averaged velocity field in quasi two-dimensional focusing wave

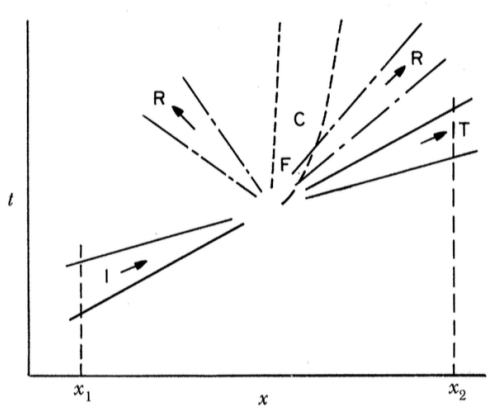

Figure 3.1: A schematic of the focusing wave groups considered in this chapter, from *Rapp and Melville* (1990). The incident wave group, I, focuses at F, radiating, R, and transmitting, T, waves away from this region. In the area of breaking, currents, C, and turbulence will be generated. Far upstream and downstream of the breaking region, (x_1, x_2) respectively, the waves are approximately linear.

breaking laboratory experiments (*Rapp and Melville* 1990, *Melville et al.* 2002). This vortex is the mean flow induced by breaking, and it is observed to be robust, lasting more than 50 wave periods after the breaking event (*Rapp and Melville* 1990, *Melville et al.* 2002, *Pizzo and Melville* 2013). This led *Sullivan et al.* (2004, see also *Sullivan et al.* 2007) to parameterize the bulk effects of a breaking wave on the ensemble-averaged flow by an impulsive body force. By performing a direct numerical simulation of the Navier-Stokes equations for the fluid response to this body force model, they were able to reproduce the characteristic flow observed in the laboratory.

Pizzo and Melville (2013) used similar arguments to those of *Drazen et al.* (2008) to propose a scaling model for the circulation, Γ, induced by both plunging and spilling breaking waves. They found

$$\Gamma = \gamma_0 \frac{(hk)^{\frac{3}{2}} c^3}{g}, \tag{3.2}$$

with γ_0 an order-one scaling constant. The model was shown to be in agreement with the limited available laboratory data. We will further examine this relationship numerically in this chapter. Finally, the arguments in their paper also served

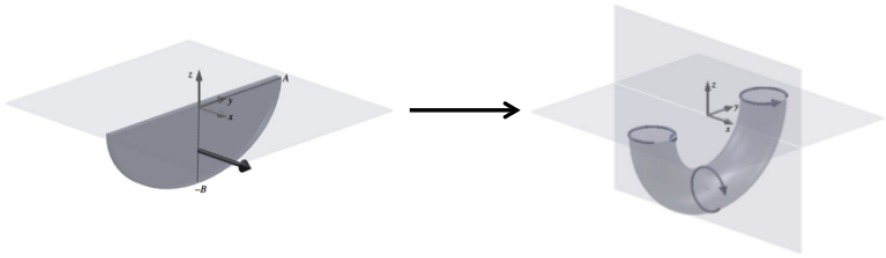

Figure 3.2: A sketch of the bulk scale effects of deep-water breaking on the water column. We assume that breaking acts like a thin impulsively-forced disk of semi-major axis A and semi-minor axis B, being forced from rest to a speed U along the x direction. The disk is then assumed to dissolve, with the flow rolling up where it is strongest, that is along its perimeter, leaving a persistent vortex ring that characterizes the ensemble-averaged post breaking flow.

to clarify the agreement that was found by *Romero et al.* (2012, see also *Grare et al.* 2013, *Deike et al.* 2015) for the scaling of b for both plunging and spilling breaking waves.

The chapter is organized as follows. Section 3.2 discusses the dynamics of the breaking event, and we derive the scaling model for the energy remaining in the vortex induced by breaking. Section 3.3 examines this model through direct numerical simulations of the two-phase Navier-Stokes equations. Section 3.4 presents the conclusions and implications.

3.2 The impulse and energy in the post breaking mean flow

In this section we examine the impulse and energy needed to generate the half-ring vortex induced by breaking, and compare this to the momentum and energy lost from the wave field by the breaking event. This will yield a scaling model for the amount of energy remaining in the mean flow after a breaking event.

3.2.1 Properties of the flow induced by breaking

Consider a wave group that propagates in the x direction, with y denoting the transverse direction and z pointed upwards. A conspicuous feature of the

focusing wave packets sketched in Figure 3.1 is that there is a natural separation between the waves and the breaking induced flow. That is, the waves rapidly propagate out of the region of breaking, so that we assume there is no subsequent interaction between them and the induced flow. Furthermore, we assume that any exchange of energy from the wave field to the water column is confined to the region of breaking. The evolution of the energy of the waves outside of this breaking region is well known (*Whitham* 1962), and we balance this with the energy lost to the water column in the breaking region by dissipation via turbulence (see also *Rapp and Melville* 1990) and current generation. That is,

$$\frac{\partial E}{\partial t} + \frac{\partial F}{\partial x} = \mathcal{D}, \tag{3.3}$$

where E, F are the energy density and energy flux of the waves, respectively, in the regions far from the breaking event. The explicit forms of the energy and energy flux are

$$E = \left\langle \int_{-d}^{\eta} \frac{1}{2}\rho(\boldsymbol{\nabla}\phi)^2 + \rho g z \; dz \right\rangle; \qquad F = \left\langle \int_{-d}^{\eta} \left(p + \frac{1}{2}\rho(\boldsymbol{\nabla}\phi)^2 + \rho g z \right) \phi_x \; dz \right\rangle. \tag{3.4}$$

Here, p is the pressure, ϕ is the velocity potential, η is the free surface displacement, ρ is the density of water, g the acceleration due to gravity and d is the water depth (taken to tend towards infinity). Furthermore, the angled brackets represents the time average over the carrier wave period and $\mathcal{D}$ is a parametrization of the energy that is lost to turbulent dissipation and current generation (*Phillips* 1977, *Rapp and Melville* 1990, *Sullivan et al.* 2007, §3.1). For linear theory, and in the absence of breaking ($\mathcal{D} = 0$), equation (3.3) implies that $F = c_g E$ for $c_g = \omega_0/2k_0$ the group velocity, with ω_0 and k_0 the characteristic angular frequency and wavenumber, respectively (*Phillips* 1977).

Based on laboratory studies of these breaking packets (*Rapp and Melville* 1990, *Melville et al.* 2002, *Drazen et al.* 2008) we assume the term $\mathcal{D}$ takes the form

$$\mathcal{D} = \left\langle \int_{-d}^{\eta} \epsilon \; dz \right\rangle + \frac{\partial E_c}{\partial t}, \tag{3.5}$$

where ϵ is the energy dissipated by the breaking induced turbulence and E_c is the energy of the mean flow in the breaking region.

Following (*Rapp and Melville* 1990), we spatially integrate over the breaking region and then take the long-time average over a prescribed time $\mathcal{T}_0$. The long time average allows a physical separation between the waves and the flow induced by breaking, so that we are left with the relationship

$$\Delta\mathcal{F} = \mathcal{E}_c + \varepsilon, \tag{3.6}$$

where

$$\Delta\mathcal{F} = -\frac{1}{\mathcal{T}_0}\int_0^{\mathcal{T}_0} \left(F(x_2) - F(x_1)\right)\ dt, \tag{3.7}$$

is (minus) the change in energy flux over the volume under consideration and

$$\mathcal{E}_c = \frac{1}{\mathcal{T}_0}\int_{x_1}^{x_2}\int_0^{\mathcal{T}_0} \frac{\partial E_c}{\partial t}\, dt\, dx = \frac{1}{\mathcal{T}_0}\int_{x_1}^{x_2} E_c(\mathcal{T}_0)\, dx; \qquad \varepsilon = \frac{1}{\mathcal{T}_0}\int_0^{\mathcal{T}_0}\int_{x_1}^{x_2}\int_{-d}^{\eta} \epsilon\, dz\, dx\, dt. \tag{3.8}$$

Recall, x_1 and x_2 are locations far upstream and downstream of the breaking location, respectively, where the waves are approximately linear (see Figure 3.1). In this section we will examine the ratio of $\mathcal{E}_c$ and $\Delta\mathcal{F}$, which compares the energy in the mean flow to the total energy lost by the wave packet. In order to do so, we must quantify both of these terms, as a function of the variables characterizing the breaking wave field.

To this end, we consider the impulse associated with a given vorticity field $\mathbf{\Omega} = \boldsymbol{\nabla} \times \mathbf{u}$, where $\mathbf{u}$ is the velocity field induced by the breaking event. The hydrodynamic impulse, $\mathbf{I}$, sometimes referred to as Kelvin's impulse (*Lamb* 1932, *Bühler* 2007), is defined as

$$\mathbf{I} = \frac{1}{n-1}\int_V \mathbf{x} \times \mathbf{\Omega}\ dV, \tag{3.9}$$

where $n > 1$ is the spatial dimension of the system, and V is a volume containing the distribution of vorticity $\mathbf{\Omega}$. Note, unlike the momentum of the fluid, the impulse

is well defined, as it does not contain the surface integral pressure terms which are not absolutely convergent (*Batchelor* 1967, *Saffman* 1992, *Bühler* 2007).

The rate of change of the impulse is given by

$$\frac{d\mathbf{I}}{dt} = \int_V \boldsymbol{f} dV, \tag{3.10}$$

where $\boldsymbol{f}$ is a force necessary to instantaneously generate the prescribed flow from rest. Therefore, the impulse of a given vorticity field can be related to the net force exerted to create it. This allows us to *invert* the vortex ring problem, and find the momentum, and then the energy, needed to generate this vortical flow from rest, to be compared with the total energy lost by breaking. In particular, we will exploit the relationship between the impulse needed to generate the post breaking vorticity field and the momentum lost by the wave field due to breaking (*Bühler* 2014, §12.4.2).

However, in order to make progress in solving for this integral $\mathbf{I}$, we must constrain the form of the breaking-induced vorticity of the mean flow, i.e. $\boldsymbol{\Omega}$, which we will now do.

Recall, *Pizzo and Melville* (2013) found that the evolution of the circulation, Γ, of the breaking-induced mean flow can be modeled as

$$\frac{d\Gamma}{dt} = \oint_{\mathcal{C}} \mathbf{F} \cdot d\boldsymbol{\ell}, \tag{3.11}$$

where

$$\Gamma = \oint_{\mathcal{C}} \mathbf{u} \cdot d\boldsymbol{\ell}. \tag{3.12}$$

Here, $\mathcal{C}$ is a material contour moving with the mean flow, and $\mathbf{F}$ is a parametrization of the breaking-induced body force, responsible for the generation of the mean flow.

There is some choice in how to parameterize the forcing due to breaking, as it is unclear how the final momentum of the packet varies as a function of its characteristic initial parameters. Following the laboratory and numerical studies, *Pizzo and Melville* (2013) sought a function $\mathbf{F}$ that was compact in space and time, had an asymmetry between the x and transverse (y) direction, and was also

symmetric about this transverse direction. Based on these constraints, the authors chose to model **F** using a thin, impulsively-forced half elliptical disk, of semi-major axis A and semi-minor axis B being forced from rest to a speed U along it's axis of symmetry, that is in the x-direction, as shown in Figure 3.2. The disc is assumed to dissolve (*Taylor* 1953), leaving an elliptical vortex ring, whose properties can be easily related to those of the forced disc.

3.2.2 Partitioning of the energy of the flow induced by breaking

Dhanak and Bernardinis (1981, Appendix A, see also *Pizzo and Melville* 2013) found that the impulse, I, of the elliptical disk can be related to the kinetic energy, $\mathbb{T}$, of the generated vortex ring by (c.f. equation 3.9) $I = 2\mathbb{T}U^{-1}$ (this is also consistent with the study of *Linden and Turner* 2001).

Next, we let $\Delta\mathcal{M} = \mathcal{M}(t_2) - \mathcal{M}(t_1)$ be the total momentum lost from the wave field during the breaking process, with (t_1, t_2) being times long before and after breaking, respectively. The wave momentum $\mathcal{M}$ is that which is required to generate the wave packet from rest, so that it is in general non-zero, and for linear waves is equal to the momentum associated with the Stokes drift (*McIntyre* 1981, §4). Note, this quantity is well defined, unlike the scenario for general fluid flows discussed in §3.2.1. Next, some of the momentum lost from the wave field due to breaking will propagate away from the region in the form of surface waves; however, *Rapp and Melville* (1990) found that the energy in these radiated waves was much less than the total energy lost by breaking, so that we ignore this effect. Therefore, we assume that this loss of momentum from the wave field is equivalent to the impulse necessary to generate the post breaking mean flow from rest, that is $I = \Delta\mathcal{M}$.

This allows us to rewrite the kinetic energy of the mean flow as

$$\mathbb{T} = \frac{U\Delta\mathcal{M}}{2} = \frac{\Gamma}{4B}\Delta\mathcal{M}. \tag{3.13}$$

where we have substituted in the formula for the circulation of the elliptical vortex

ring found by *Dhanak and Bernardinis* (1981), i.e. $\Gamma = 2UB$.

We would like to relate this to the total energy lost by breaking. For linear waves, the total wave energy $\mathbb{E}$ can be related to the momentum via the relationship $\mathbb{E}_1 = c_1\mathcal{M}_1$ and $\mathbb{E}_2 = c_2\mathcal{M}_2$ where the subscripts 1 and 2 mean that the functions are evaluated at times $t_{(1,2)}$ (where we recall equipartition holds) and c_i is the phase velocity of the waves in the packet (*Phillips* 1977, 1985, *Sullivan et al.* 2007). Therefore, the total energy lost by breaking is $\Delta\mathbb{E} = (c_1\mathcal{M}_1 - c_2\mathcal{M}_2)$.

The characteristic phase velocities are given by $c_i = \sqrt{g/k_i}$, with k_i the spectrally weighted wavenumber (*Drazen et al.* 2008, *Tian et al.* 2010). Following *Drazen et al.* (2008), we assume that $c_2 = c_1(1 + \mathcal{O}(S))$, which was found to be experimentally true to within 5-10% (see §3.1.1 *Tian et al.* 2011). Therefore, to first order we rewrite this as $\Delta\mathbb{E} = c_1\Delta\mathcal{M}$. Then, the ratio of the energy in the breaking induced vortex to the total energy lost due to breaking is

$$\frac{\mathbb{T}}{\Delta\mathbb{E}} = \frac{\Gamma}{B}\frac{\Delta\mathcal{M}}{c_1\Delta\mathcal{M}} = \frac{\Gamma}{Bc_1}. \tag{3.14}$$

Recall from the introduction that *Pizzo and Melville* (2013) proposed that $\Gamma = \gamma_0(hk)^{\frac{3}{2}}c^3/g$, where γ_0 is an order one constant and c is the characteristic phase velocity of the input wave packet, assumed to be c_1 to within the scatter of the data. Next, from *Rapp and Melville* (1990, see their figure 34), and the scaling arguments of *Pizzo and Melville* (2013), the depth to which the fluid is mixed, i.e. B, scales with h, which implies that

$$\frac{\mathbb{T}}{\Delta\mathbb{E}} = \varkappa_0(hk)^{\frac{1}{2}}, \tag{3.15}$$

where $\varkappa_0$ is a constant.

We now relate this quantity to the measurements taken in the laboratory by connecting the ratio given in equation (3.15) with the ratio of $\Delta\mathcal{F}$ and $\mathcal{E}_c$, as discussed above. Note, these later quantities both have the units of a flux of energy, as opposed to the units of energy in equation (3.15). As the vortex flow is generated by the breaking event, we assume that the characteristic velocity associated with this process, as well as that related to the change in energy of the

waves, are equivalent, so that we can simply equate the flux quantities measured in the lab to the ratio of the energy in the mean flow over the total energy lost, which we define as $\mathcal{R}_c$. That is

$$\mathcal{R}_c \equiv \frac{\mathcal{E}_c}{\Delta\mathcal{F}} = \varkappa(hk)^{\frac{1}{2}}, \tag{3.16}$$

where $\varkappa$ is a constant and we have defined the ratio of the kinetic energy of the mean vortical flow to the total energy lost as $\mathcal{R}_c$. Note, the relationship between $\mathcal{R}_c$ and (hk) is relatively weak, which will be manifest when we examine this model numerically.

3.3 DNS of breaking waves

3.3.1 Numerical experiment

To corroborate our scaling model, we now perform Direct Numerical Simulations (DNS) of the two-dimensional Navier-Stokes equations in a two-phase fluid (air and water) accounting for surface tension and viscous effects using the open source solver Gerris (*Popinet* 2003, 2009), based on a quad/octree adaptive spatial discretization, multilevel Poisson solver. The interface between the high density liquid (water) and the low density gas (air) is reconstructed by a Volume Of Fluid (VOF) method. This solver has been successfully used in various multiphase problems like atomization (*Fuster et al.* 2009), the growth of instabilities at the interface (*Fuster et al.* 2013), capillary wave turbulence (*Deike et al.* 2014), two- and three-dimensional wave breaking (*Fuster et al.* 2009, *Deike and Melville* 2015, *Deike et al.* 2015).

As in *Deike and Melville* (2015), *Deike et al.* (2015), we use nonlinear Stokes waves of wavelength λ as initial conditions to study wave breaking. In order to simulate the laboratory experiments, the waves must be able to propagate freely after breaking without interfering with the turbulent flow created during the breaking event. Thus we consider a 2D rectangular numerical domain, with dimension $L = 8\lambda$ in the horizontal propagation direction and $l = \lambda$ in the vertical direction.

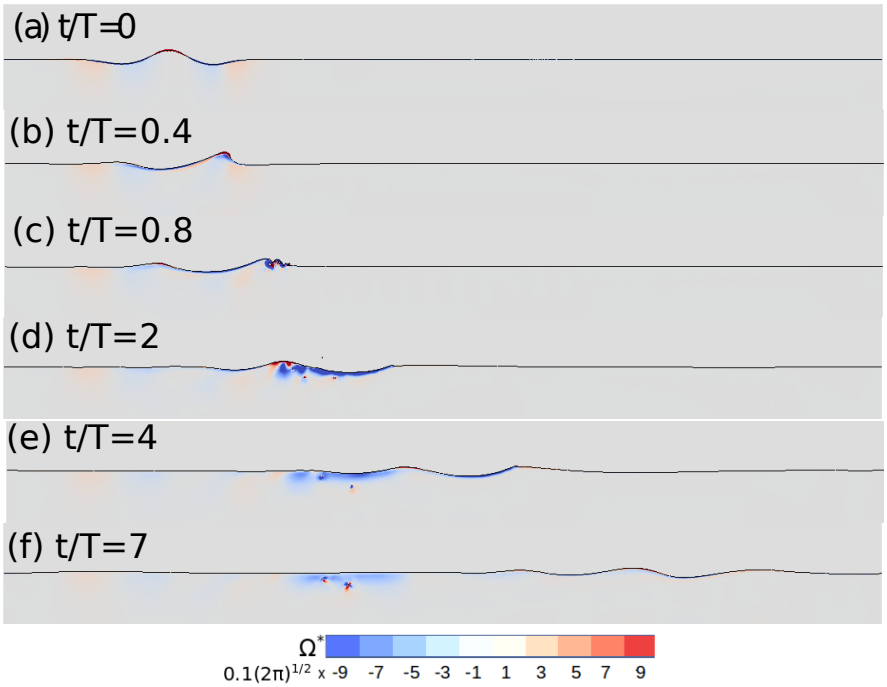

Figure 3.3: Time evolution of a plunging breaker with the vorticity field $\Omega^* = \Omega/\omega_0$ at different time steps. The wave starts at the left of the numerical domain, propagates to the right, and breaks after half a period of propagation. The waves then propagate out of the region where breaking occurred, leaving an active vorticity field that characterizes the post-breaking flow. The initial conditions were chosen such that $S = 0.55$, $Re = 4 \times 10^4$, $Bo = 200$.

The mean water level is set at $\eta = 0$, so that the water depth is $d = \lambda/2$. Boundary conditions are periodic in x, but as we will see the main wave never reaches the end of the numerical domain for times necessary to resolve the properties under investigation. The top and bottom walls are free-slip (at $z = \pm d = \lambda/2$). The total simulation time corresponds to $8T$, where $T = 2\pi/\omega_0$ is the wave period and ω_0 the linear angular frequency of the input wave form.

A third-order Stokes wave solution for the interface $\eta(x,t)$ and the velocity potential $\phi(x,z,t)$ in the water are used as initial conditions at the left of the numerical domain, for $x \in [\lambda/2 : 3\lambda/2]$ and in the rest of the domain, the interface and the velocity are set to 0 by applying a smooth windowing.

The physical properties of the two phases are those of air and water, and this manifests itself through the density and viscosity ratios. The Bond number is defined as $Bo = \Delta\rho g/(\gamma k^2)$, with $\Delta\rho$ the density difference between the two fluids, g the acceleration due to gravity and γ is the surface tension, so that B_0 gives the ratio between gravity and surface tension forces. The Reynolds number in the water is $Re = c\lambda/\nu$, where $c = \sqrt{g/k}$ is the linear gravity wave phase speed and ν is the kinematic viscosity of the water, which is set to $Re = 40000$. This choice is related to spatial resolution constraints, but should not affect the results regarding the wave dissipation, since we are at a sufficiently high Reynolds number (*Deike and Melville* 2015, *Deike et al.* 2015) to capture the phenomena in question. We choose $Bo = 200$ to obtain plunging breakers at high initial wave slope and also to be able to correctly resolve surface tension effects.

We define the characteristic slope to be $S = ak$, with a the initial wave amplitude and $k = 2\pi/\lambda$ the wave-number. S varies from 0.25 to 0.65, i.e. from non-breaking waves to strongly plunging waves (*Deike et al.* 2015). Note that since we are using only the third order Stokes wave solution, slopes higher than the limiting slope for the full Stokes wave solution can be defined. It is useful to recall that the slope at breaking is proportional to the initial wave slope in this configuration (*Deike and Melville* 2015, *Deike et al.* 2015), which is consistent with the laboratory findings of the analogous relationship for focusing packets (*Drazen et al.* 2008).

Adaptive mesh refinement is used to accurately solve for the interface and the vortex structures, with a mesh size of $dx = dy = \lambda/512$. This configuration allows accurate solutions for the dissipative scales, as shown by previous two- and three-dimensional simulations (*Deike and Melville* 2015, *Deike et al.* 2015).

A typical DNS evolution of a breaking wave, with $S = 0.55$ is shown in Figure 3.3. The Stokes wave propagates from the left to the right before undergoing strongly nonlinear behavior leading to breaking. A jet is formed at the front of the wave that subsequently impacts the water surface. The time of the breaking event, or impact with the surface, t_b, occurs between $t/T = 0.5$ and $t/T = 1$, as in *Deike and Melville* (2015), *Deike et al.* (2015), while the jet impacts the free surface at approximately $x_b = x/\lambda \approx 2.5$. Figure 3.3 shows that the breaking event generates turbulent motion and strong vortical structures in the water in the area bounded by $x \in [2.5 : 3.5]\lambda$. This defines the breaking area A. After breaking, the waves are transmitted and radiated from the breaking region, subsequently rendering the free surface as a rigid lid in this area, which is consistent with the laboratory studies and Figure 3.1. However, the breaking induced current, characterized by the vortex, is still present in the breaking region several periods after t_b.

Here, we focus on post-breaking flow properties and the resulting vorticity, and its associated circulation, as well as the kinetic energy flux of the current in the breaking area, for long times after the waves have propagated away.

As was discussed above, the generated vortical structure has been observed experimentally, and was found to be a coherent vortex by *Rapp and Melville* (1990), *Melville et al.* (2002), which was described in more detail by *Pizzo and Melville* (2013). Figure 3.4 shows a close-up of this area several periods after breaking. A coherent vortex is indeed observed and remains stable, slowly moving towards the right of the numerical domain. Its intensity slowly decreases due to viscous dissipation, consistent with *Melville et al.* (2002). Recall, Ω^* is the vorticity field normalized by the characteristic angular frequency ω_0, in the y direction.

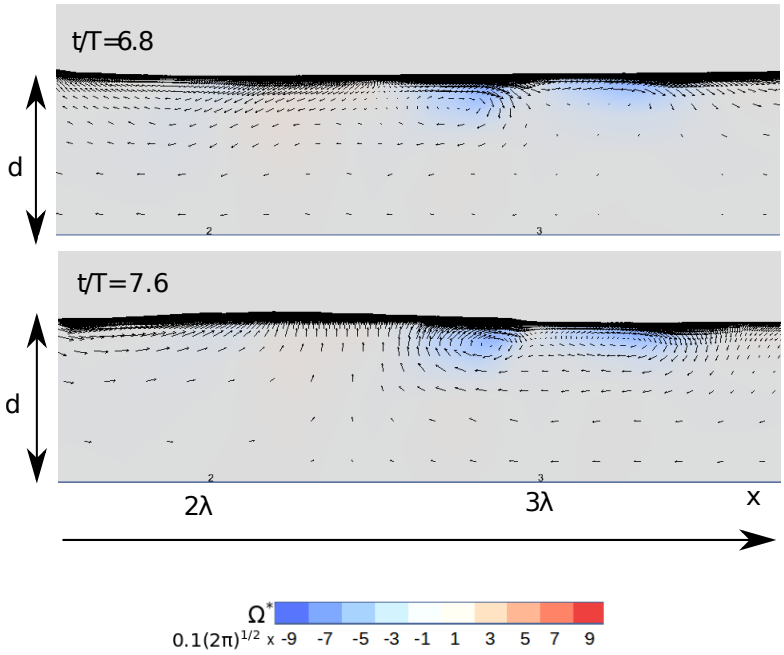

Figure 3.4: The normalized vorticity field Ω^* remaining in the region of breaking for a plunging breaker. The post breaking flow is characterized by a compact region of vorticity, outside of which the flow is largely irrotational. Note, the free surface is approximately quiescent at these times, with the (relatively fast) waves having propagated away. $Re = 4 \times 10^4$, $Bo = 200$ and $S = 0.5$.

3.3.2 Energy dissipated by breaking, circulation and mean currents

We now calculate the integral properties of the breaking waves for various slopes S. To begin, we compute the left hand side of equation (3.7), where we connect the energy flux F with the energy density through linear theory (far upstream and downstream of the breaking event). That is, the energy flux at a given location is then $F(x) = c_g E(x)$ where $c_g = \frac{1}{2}c_0$ is the group velocity of the Stokes wave, c_0 being the phase speed of the Stokes waves. As defined in §3.2, the dissipated energy flux due to breaking is then given by $\Delta\mathcal{F} = c_g \Delta E$. Note, following the laboratory experiments of *Drazen et al.* (2008), this relation assumes that the group velocity is approximately equal before and after breaking. The dissipated energy flux per unit length of breaking crest ϵ_l is given by $\epsilon_l = \Delta\mathcal{F}/\tau_b$, where τ_b is the active breaking time, and in these experiments it is found that $\tau_b \approx T$ which is consistent with other laboratory (*Drazen et al.* 2008) and numerical studies (*Deike and Melville* 2015, *Deike et al.* 2015). The breaking parameter b as a function of the slope S in the present DNS is found in good agreement with previous experimental results and the semi-empirical model of *Drazen et al.* (2008, see also *Grare et al.* (2013)) and *Romero et al.* (2012) for strong breaking waves, as in our previous numerical work (*Deike and Melville* 2015, *Deike et al.* 2015).

The integrated vorticity and the kinetic energy flux over the area A are approximatively constant with time, slowly decreasing due to viscous dissipative effects, which is consistent with the laboratory studies of *Melville et al.* (2002). The circulation Γ over A, given by equation (3.12), is averaged over two wave periods, starting six wave periods after the breaking event when the waves have propagated out of the region of breaking. Figure 3.5a shows Γ as a function of the wave slope, together with the corresponding scaling from *Pizzo and Melville* (2013) for the circulation, $\Gamma = \gamma_0(S - S_0)^{3/2}$, where γ_0 is an order one constant and the threshold for breaking S_0. The constant $\gamma_0 = 0.98$ was found by a best fit with the data presented in *Pizzo and Melville* (2013), while $S_0 = 0.08$ is the threshold that best fits multiple laboratory studies, as discussed in *Romero et al.* (2012). Good agreement is found between the model for Γ and the available experimental data

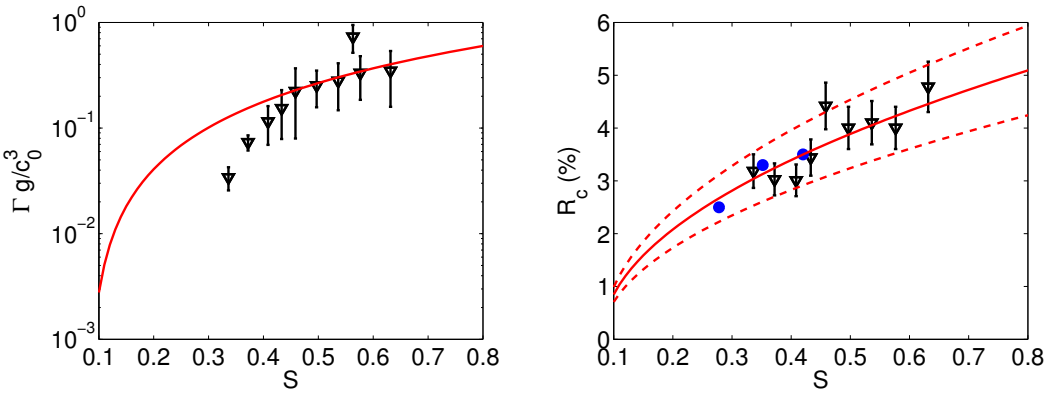

Figure 3.5: (a) Circulation generated by the breaking event Γ (normalized by c_0^3/g) as a function of S. Solid line is the model from *Pizzo and Melville* (2013) fitted to experimental data, $\Gamma g/c_0^3 = \gamma_0(S - S_0)^{3/2}$, where $\gamma_0 = 0.98$ and $S_0 = 0.08$. (b) Ratio of the energy flux in the current (created by the breaking event) and the dissipated energy flux due to the breaking wave, $\mathcal{R}_c$. Triangles are DNS data and closed circles laboratory data from *Rapp and Melville* (1990). Solid line is $\mathcal{R}_c = \mathcal{E}_c/\Delta F = \chi(S - S_0)^{1/2}$ based on the model presented in §3.2, Eq. 3.16 and including an empirical threshold slope, Eq. 3.17, with $S_0 = 0.08$ and $\chi = 0.06$ the best fit to the data. The dashed lines are Eq. 3.17 with $\chi = 0.05$ and $\chi = 0.07$, respectively and $S_0 = 0.08$.

and the numerical results, with the best agreement occurring for larger slopes. This is consistent with the findings of *Deike and Melville* (2015), *Deike et al.* (2015) for the energy dissipation rate, where it is noticed that the different breaking generation methods between the laboratory and the numerical experiments are manifested in the breaking threshold parameter S_0. Note, the outlier occurring at $S = 0.56$ is due to a persistent bubble that remains in the breaking region for long times after the breaking event.

Finally, Figure 3.5b shows the main result of this chapter, namely the ratio of the energy flux transferred to the current to the dissipated energy flux due to breaking wave, i.e. $\mathcal{R}_c$. In particular, this figure shows $\mathcal{R}_c$ as a function of the wave slope, together with the experimental data from *Rapp and Melville* (1990) and the scaling given by equation (3.16),

$$\mathcal{R}_c = \chi(S - S_0)^{1/2}, \tag{3.17}$$

with $\chi = 0.06 \pm 0.01$ and $S_0 = 0.08$ is the critical slope determined by *Romero et al.* (2012). The value $\chi = 0.06$ is the least-squares fit to the laboratory and numerical data.

We find that $\mathcal{R}_c$ varies from 2 to 5 % for slopes corresponding to incipient breaking wave to strong plunging events, in good agreement with the earlier experimental results from *Rapp and Melville* (1990). The scatter in the numerical data comes from the difficulties in properly estimating a small difference between two large quantities (energy flux before and after breaking) and the fact that the ratio $\mathcal{R}_c$ is a small quantity. Finally the agreement with the scaling argument presented in §3.2 is encouraging. In the next section, we discuss some of the implications of these results.

3.4 Discussion

In this study we have proposed a simple model for the energy transferred from the wave field to the mean flow by wave breaking. This serves as another study (*Drazen et al.* 2008, *Romero et al.* 2012, *Pizzo and Melville* 2013, *Deike et al.* 2015) that uses simple scaling arguments (with the relevant parameter being the local slope at breaking S) to describe integral properties associated with wave breaking. That is, S, which is known a priori and is related to the energy available to the water column due to breaking, is the primary variable that characterizes integral properties of the post breaking flow field.

What is perhaps surprising is that for such a complex turbulent flow as wave breaking, so much information can be teased out of a relatively simple vortex dynamics model, or equivalently, that the vortex dynamics has such a constraint on the overall dynamics of the flow. If sustained by further experimental and numerical support, the results of this chapter provide the beginnings of the answer to the question: How is the energy lost from a wave field due to breaking distributed between currents and turbulence? The results suggest that only a very small fraction of that energy is available for generating currents, the rest going into local turbulence and mixing of the near-surface waters.

Ocean currents can be generated by a variety of phenomena, including tidal forcing, buoyancy gradients, wind drift, the irrotational wave induced mean flow (i.e. Stokes drift) and wave breaking. This chapter has focused on the last effect, as it is believed that wave breaking is the dominant contribution to the wind-driven currents. In particular, for wind speeds above (6-8) m s^{-1}, the momentum and energy from the atmosphere is mainly transmitted through the wave field, with nearly 100% of these quantities being passed directly to the water column through the action of wave breaking (*Terray et al.* 1996, *Donelan* 1998, *Banner and Tian* 1998, *Sullivan et al.* 2007, *Sullivan and McWilliams* 2009). That is, just a small amount of energy is radiated away in the form of surface waves. We have found that most of the energy lost locally from the wave field (greater than 95% for the waves considered in this chapter) is dissipated through turbulence, with the remainder going into the breaking induced mean flow.

Phillips (1985) proposed that a statical description of wave breaking could be used to deduce bulk scale features of the equilibrium range of the surface wave field (where, by definition, 100% of the wind input is passed locally to the water column), including the total energy dissipated by the wave field due to breaking. This description relies crucially on the statistical distribution of breaking, as a function of the variables characterizing the local ocean and atmospheric conditions. In a recent paper, *Sutherland and Melville* (2013), using a scaling argument motivated by field data, took the relevant variables to be the atmospheric friction velocity, the significant wave height, the phase velocity of the waves at the peak of the wind-wave spectrum, and gravity. The resulting form of the probability distribution function for wave breaking based on these variables was found to collapse the existing field data onto a single curve.

Therefore, the framework derived in this chapter could be extended, in the spirit of *Romero et al.* (2012), to give a spectral statistical description of the energy transferred to the mean flow due to wave breaking in a wind-wave model. This would also be important for constraining global energy budgets in more sophisticated wave resolving ocean-atmosphere models (*Sullivan et al.* 2007, *Cavaleri et al.* 2012).

The text in this chapter has been submitted to the Journal of Fluid Mechanics as "Current generation by deep-water breaking waves" by Pizzo, N.E., Deike, L. and Melville, W.K. The dissertation author wrote the paper and developed the theoretical model. Luc Deike performed the numerical simulations and contributed to the writing of the paper.

4 Wave modulation: the geometry, kinematics, and dynamics of surface-wave focusing

4.1 Introduction

This chapter reports on a theoretical and numerical study of the properties of weakly nonlinear narrow-banded deep-water wave packets (i.e. compact wave groups). Weakly nonlinear Stokes waves are subject to the Benjamin-Feir instability (*Benjamin and Feir* 1967, *Lighthill* 1965), so that the subsequent nonlinear evolution of the wave field is of considerable interest from both a mathematical (*Zakharov* 1968, *Sulem and Sulem* 1999, *Tao* 2006) and physical point of view (*Melville* 1982, *Su et al.* 1982, *Yuen and Lake* 1982).

The evolution of these wave groups can lead to highly nonlinear dissipative processes, most notably wave breaking (*Melville* 1982, *Dold and Peregrine* 1986, *Rapp and Melville* 1990). This study is motivated by the properties of these waves, and wave groups, as they focus and breaking is *approached*. However, wave breaking is a turbulent two phase process, leaving a full analytic description out of reach using current techniques. Therefore, much progress has been made through numerical (*Iafrati* 2011, *Perić et al.* 2015, *Deike et al.* 2015) and laboratory studies (*Melville* 1982, *Rapp and Melville* 1990, *Perlin et al.* 2013) in elucidating fundamental properties of these waves. Although these experiments have been pivotal for understanding features of wave focusing and breaking, the importance of the

geometry, kinematics, and dynamics in characterizing relevant scales of the wave field evolution leading up to breaking motivates the need for simple analytical tools to describe the evolution of these features of the wave group.

In this chapter we will consider dispersive focusing wave packets, which are commonly used in a laboratory setting to generate focusing and breaking waves (*Longuet-Higgins* 1974, *Rapp and Melville* 1990). The waves are inherently unsteady, with rapid variations in space and time in the region of focusing. However, many laboratory studies in the last 30 years (see, for instance, *Rapp and Melville* 1990, §1.2) have concentrated on examining the wave envelope to deduce bulk-scale characteristics of wave focusing, as many features of the focusing event are conspicuous in the behavior of the wave group. This prompts our use of a reduced set of equations governing the evolution of the wave envelope.

To this end, our model equation in this study is the spatial modified nonlinear Schrodinger equation (MNLSE; *Dysthe* 1979), originally derived by *Lo and Mei* (1985), and given by

$$\frac{\partial A}{\partial \chi} + i\frac{\partial^2 A}{\partial \tau^2} + i|A|^2 A + \beta_0 |A|^2 \frac{\partial A}{\partial \tau} + i\alpha_0 A \mathbb{H}\left(|A|_\tau^2\right) = 0, \tag{4.1}$$

where $A = A(\epsilon^2\chi, \epsilon\tau)$ is a slowly varying complex valued function, related to the lowest order coefficient of the first mode of the velocity potential expansion, $\mathbb{H}$ is the Hilbert transform, $\chi = k_0 x$, $\tau = \omega_0(2k_0/\omega_0 x - t)$, $\beta_0 = 8\epsilon, \alpha_0 = \epsilon$ and $\epsilon = a_0 k_0$ is a small parameter for (a_0, ω_0, k_0) the characteristic amplitude, angular frequency and wavenumber, respectively. This equation is a spatial (fetch) version of the MNLSE, and can be derived by either making a coordinate transformation of the MNLSE (*Lo and Mei* 1985), or can be found explicitly from a spatial version of Zakharov's equation (*Kit and Shemer* 2002). In the supplementary material, we provide an alternative derivation of this equation using Whitham's method. When $\beta_0 = \alpha_0 = 0$ equation (4.1) reduces to the nonlinear Schrodinger equation (NLSE). Finally, we note that the use of the lowest order term in the first mode of the velocity potential as a dependent variable has offered a variety of theoretical advantages, as has been repeatedly emphasized by Trulsen and colleagues (*Trulsen and Dysthe* 1997, *Trulsen* 1999, 2006), which is also found to be true in this study,

as it allows us to put the system into a variational form.

Equation (4.1) governs weakly nonlinear narrow-banded surface gravity waves and has been shown (*Lo and Mei* 1985, *Shemer et al.* 2002) to predict certain features of wave train evolution that are not apparent at lower order (i.e. when $\epsilon = 0$), including asymmetric wave envelope growth, a better prediction of the modulation instability growth rate (*Dysthe* 1979), asymmetric spectral growth, and the coupling of an Eulerian mean flow to the wave amplitude evolution. These asymmetries arise from the term in equation (4.1) with coefficient β_0, while the induced mean flow is related to the term with coefficient α_0.

The utility of the MNLSE was established by *Lo and Mei* (1985) and *Shemer et al.* (2002), who found good agreement between the MNLSE and laboratory and higher-order numerical schemes, respectively, including in regions where equation (4.1) was not explicitly valid. When the bandwidth of the wave group became very large, *Shemer et al.* (2002) found that the MNLSE was a poor predictor of the spectral evolution compared to higher order spectral method numerical simulations (see also *Clamond et al.* 2006). Finally, we note that in the spatial coordinates, the linear dispersion is *exactly* represented (*Kit and Shemer* 2002), allowing for the possibility of describing broader bandwidth wave packets (*Dysthe et al.* 2003). This should be compared to the analogous case in the canonical time evolution reference frame, where an infinite number of terms in a Taylor expansion must be used in order to represent the full linear dispersion operator (*Trulsen et al.* 2000, *Kit and Shemer* 2002).

The complexity of the MNLSE makes theoretical predictions difficult, so one must often resort to numerical computations in order to study the properties of wave fields governed by this equation. Here, we gain further insight through the development of moment evolution equations, which offer additional information about the constraints on the evolution of the wave groups. The moment evolution technique has been used extensively in the optics community (*Agrawal* 2007), as well as in the mathematics community (*Sulem and Sulem* 1999) and has been applied to the study of water waves governed by the two-dimensional NLSE (*Ablowitz and Segur* 1979).

The geometry, kinematics, and dynamics of these focusing packets are analyzed based on the following moments:

$$\mathcal{M} = \frac{1}{\mathcal{E}} \int_{-\infty}^{\infty} \tau |A|^2 \, d\tau; \qquad \mathcal{I} = \frac{1}{\mathcal{E}} \int_{-\infty}^{\infty} (\tau - \mathcal{M})^2 |A|^2 \, d\tau; \tag{4.2}$$

where $\mathcal{E} = \int_{-\infty}^{\infty} |A|^2 d\tau$ is proportional to the linear energy density of the wave packet and $\mathcal{M}$ is the centroid of this density, where its evolution is shown to quantify the speed of the wave group. Next, $\mathcal{I}$ is the variance of the wave packet, and its second derivative with respect to χ will be shown to relate packet convergence to the dynamics of the wave packet.

The concept of group velocity for nonlinear waves has been a source of theoretical ambiguity (*Peregrine and Thomas* 1979), as various definitions, consistent for linear waves, give different results when nonlinearity is considered. This is problematic as the group velocity has implications for measurements of integral properties of breaking waves, such as the energy dissipation rate (*Drazen et al.* 2008, *Tian et al.* 2010). Part of the confusion arises due to the lack of an unambiguous point representation (c.f. geometrical optics) of the wave train location. These issues are alleviated by the use of the centroid of the linear energy density as a marker of the location of the wave group which arises naturally in our theory. In the case of very narrow-banded wave groups, our theory reduces to the classical definition of the group velocity (*Whitham* 1974).

The variance of the wave packet, $\mathcal{I}$, and its second derivative will be shown to relate packet convergence to the breakdown of equipartition of the wave group. The breakdown of equipartition for permanent progressive periodic waves (i.e. Stokes waves) has been noted by *Longuet-Higgins* (1975, figure 4.2; see also the very interesting discussion in *Lighthill* 1978, Epilogue Part 2). Furthermore, the evolution of the kinetic and potential energy of focusing waves, leading up to breaking, has been reported in several numerical experiments (*Longuet-Higgins and Cokelet* 1976, *Dommermuth and Yue* 1987, *Deike et al.* 2015). In this work, we connect the asymptotic form of the difference of the kinetic and potential energy with the geometry of the wave packet, so that we associate packet focusing with deviations from energy equipartition.

The outline of this manuscript is as follows: in §4.2 the governing equation, (4.1), is shown to have an associated variational structure. Based on this formalism, we connect symmetries of the action to conservation laws, and subsequently derive conserved integral quantities. In §4.3 we derive evolution equations for the moments of the governing equation. In §4.4 we describe the numerical schemes and initial conditions that are used to examine the theoretical models. Next, in §4.5 a numerical experiment for a weakly nonlinear narrow-banded wave packet is studied within the context of our theoretical predictions. In §4.6, we examine a broadband, highly nonlinear wave packet, and analyze the predictions of our theory outside of its strict region of validity. Finally, in §4.7 we discuss our findings in the context of existing numerical and laboratory experiments. An alternative derivation of the spatial MNLSE, based on Whitham's method, is presented in the supplementary material, while certain properties of linear dispersive focusing wave packets are also discussed in this section.

4.2 Modified nonlinear Schrodinger equation and its variational structure

In this section we present the MNLSE and discuss its variational formulation. An alternative derivation of the spatial MNLSE is provided in the supplementary material.

4.2.1 The spatial MNLSE

The equation governing weakly nonlinear narrow-banded wave groups to fourth order in the small parameter $\epsilon = a_0 k_0$, in spatial (fetch) coordinates is given by (*Lo and Mei* 1985, *Kit and Shemer* 2002)

$$\frac{\partial A}{\partial \chi} + i\frac{\partial^2 A}{\partial \tau^2} + i|A|^2 A + \beta_0 |A|^2 \frac{\partial A}{\partial \tau} + i\alpha_0 A \mathbb{H}\left(|A|_\tau^2\right) = 0, \tag{4.3}$$

where $\beta_0 = 8\epsilon$ and $\alpha_0 = \epsilon$ and the Hilbert transform $\mathbb{H}$ is defined as

$$\mathbb{H}(|A|^2_\tau) = \frac{1}{\pi} P.V. \int_{-\infty}^{\infty} \frac{\partial |A(\tau')|^2}{\partial \tau'} \frac{d\tau'}{\tau - \tau'}, \tag{4.4}$$

with *P.V.* meaning we are to take the principal value of the integral (*Titchmarsh* 1948). The constants (α_0, β_0) will also make it easy to track the influence of the induced mean flow (which is related to the term with coefficient α_0), and the asymmetric self-steepening term (which is related to the term with coefficient β_0) in the ensuing calculations.

The variables in this fetch coordinate system can be related to the usual time evolution reference frame through the transformations

$$(2x' - t') = \tau; \quad x' = \chi; \tag{4.5}$$

where $x' = k_0 x,\ t' = \omega_0 t$, with (a_0, k_0, ω_0) representing the characteristic amplitude, wavenumber, and angular frequency of the packet, respectively. Throughout the rest of this section we drop the primes, for clarity of presentation. Note, we have mapped into a reference frame traveling at the linear group velocity, and for a fixed position x, τ is proportional to the negative of the elapsed time, while χ is related to the fetch (or stretched distance), and finally the complex valued function $A = A(\epsilon^2 \chi, \epsilon\tau)$ is nondimensionalized by the amplitude a_0. Formally, the scaling is such that $A \sim \mathcal{O}(\epsilon)$, while $A_\tau \sim \mathcal{O}(\epsilon^2)$ and $A_\chi \sim \mathcal{O}(\epsilon^3)$.

This equation is usually written as a set of coupled PDEs in two dependent variables, $(A, \overline{\Psi}\big|_{z=0})$, where $\overline{\Psi}$ is the velocity potential of the mean flow. To third order in ϵ, the two variables are connected by the relation

$$\left.\frac{\partial \overline{\Psi}}{\partial z}\right|_{z=0} = \frac{\partial |A|^2}{\partial \tau}, \tag{4.6}$$

which implies that gradients in the radiation stress lead to the generation of a mean flow (*Dysthe* 1979, *McIntyre* 1981). Following *Janssen* (1983), this allows us to write our governing equation as a PDE in one variable by recognizing that $4\overline{\Psi_\tau}$ and $\overline{\Psi_z}$ are harmonic conjugates, that is they are real and imaginary parts of

an analytic function. Therefore, we connect the two variables, evaluated at $z = 0$, via the Hilbert transform, $\mathbb{H}$, and hence we arrive at (4.3). Note, the explicit relationship between $\overline{\Psi_\tau}$ and A at the mean surface height (which to this order occurs at $z = 0$) is given by

$$\overline{\Psi_\tau}\big|_{z=0} = \frac{1}{4}\mathbb{H}(|A|^2_\tau). \tag{4.7}$$

4.2.2 Variational formulation

In this section we consider a variational formulation of equation (4.3). This follows, and extends, the classical work on the variational formulation of the NLSE.

By employing Whitham's method, presented in the supplementary material, we find that the following Lagrangian density governs fourth order weakly nonlinear narrow-banded waves in the complex valued dependent variable A and independent variables (χ, τ):

$$\mathcal{L} = \frac{i}{2}\left(A\frac{\partial A^*}{\partial \chi} - A^*\frac{\partial A}{\partial \chi}\right) - \mathcal{H}, \tag{4.8}$$

where $\mathcal{H}$ is defined as (c.f. *Gramstad and Trulsen* 2011, Appendix C)

$$\mathcal{H} = |A_\tau|^2 - \frac{1}{2}|A|^4 - \frac{\alpha_0}{2}|A|^2\mathbb{H}(|A|^2_\tau) + i\frac{\beta_0}{4}|A|^2(A^*A_\tau - AA^*_\tau), \tag{4.9}$$

and * denotes the complex conjugate. The action associated with this Lagrangian density is defined as

$$\mathcal{S}(A, A^*) = \int_{\chi_0}^{\chi_f}\int_{\mathbb{R}} \mathcal{L}\; d\tau\; d\chi, \tag{4.10}$$

which is a functional over all admissible functions satisfying the prescribed conditions at $A(\tau, \chi_0)$ and $A(\tau, \chi_f)$. Hamilton's principle states that the governing equations of the system are found by requiring that $\mathcal{S}$ be stationary. That is, we seek solutions (A, A^*), such that

$$\delta\mathcal{S} = \mathcal{S}(A + \delta A, A^* + \delta A^*) - \mathcal{S}(A, A^*) = 0, \tag{4.11}$$

for infinitesimal $(\delta A, \delta A^*)$. Substituting the Lagrangian density into the action,

then applying Hamilton's principle, and recalling the anti-self-adjoint nature of the Hilbert transform (*Titchmarsh* 1948), gives us equation (4.3).

The variational formalism allows us to look at the symmetries of the action, i.e. equation (A.8), and their associated conservation laws and conserved integrals.

4.2.3 Conserved quantities

In this subsection we will derive several local conservation laws, as well as their associated conserved integrals.

Noether's theorem connects continuous symmetries of the action with conserved quantities. In particular, consider a mapping of independent and dependent variables

$$\tau \to \tilde{\tau}; \qquad \chi \to \tilde{\chi}; \qquad A \to \tilde{A}, \tag{4.12}$$

and its associated action $\tilde{\mathcal{S}}(\tilde{A}(\tilde{\chi},\tilde{\tau}),\tilde{A}^*(\tilde{\chi},\tilde{\tau}))$. We look for transformations that leave $\Delta\mathcal{S} = \tilde{\mathcal{S}} - \mathcal{S}$ invariant, i.e. $\Delta\mathcal{S} = 0$.

We begin by considering phase translation invariance which is shown by letting $\tilde{A} = e^{is}A$, for s a real constant, and noting that the action remains invariant. This transformation, to first order, implies $A \to \tilde{A} = A + \delta A = A + isA$, and $\tilde{\tau} = \tau,\ \tilde{\chi} = \chi$, whence we find

$$\Delta S = \int_D \left(\frac{\partial |A|^2}{\partial \chi} + \frac{\partial \mathcal{J}}{\partial \tau} \right)\, d\chi\, d\tau = 0, \tag{4.13}$$

where the flux $\mathcal{J}$ is

$$\mathcal{J} = i\left(A^* A_\tau - A A_\tau^*\right) + \frac{\beta_0}{2}|A|^4, \tag{4.14}$$

and D is the domain of integration. This is true for arbitrary integration domains D, so that we have a local conservation law corresponding to phase translation invariance, namely

$$\frac{\partial |A|^2}{\partial \chi} + \frac{\partial}{\partial \tau}\left(i\left(A^* A_\tau - A A_\tau^*\right) + \frac{\beta_0}{2}|A|^4 \right) = 0. \tag{4.15}$$

Note, if $(A^* A_\tau - A A_\tau^*)$ is constant in τ, then equation (4.15) takes the form of the

inviscid Burger's equation. This equation admits shock solutions (see, for example, *Whitham* 1974, §4), which are characterized by the steepening of the forward face of the initial condition, with the modulus of the slope going to infinity in finite time. The term $(A^*A_\tau - AA^*_\tau)$ arises due to the dispersion in equation (4.3), which acts to retard the shock formation, so that a detailed analysis of the relative strength of the dispersion, compared to the nonlinearity, must be carried out to see if shocks do occur. The conditions under which envelope shocks occur could have mathematical (see, e.g., *Constantin and Escher* 1998) and physical implications (*Whitham* 1974, §13.14); however, this topic is outside of the scope of the current chapter, and will not be pursued here.

We note that the tendency for wave groups to lean forward as focusing occurs is commonly observed in laboratory experiments (see, for instance *Melville* 1983, figure 1), and will be shown to be the case for the wave packets considered in this chapter in §4.5 and §4.6. The description of the asymmetric wave modulus evolution for these focusing groups is one of the results of this manuscript.

Next, as we are exclusively considering compact wave groups in this chapter, we can rewrite (4.15) as

$$\frac{d\mathcal{E}}{d\chi} \equiv \frac{d}{d\chi}\int |A|^2 \, d\tau = 0. \tag{4.16}$$

This quantity is related to the *linear* energy density of the wave group.

Secondly, we look at the quantity associated with action invariance to τ translations. That is, we consider the transformation $A \to \tilde{A}$, $\chi \to \tilde{\chi}$ and $\tau \to \tilde{\tau} = \tau + \delta\tau$ to first order in $\delta\tau$. In this case, invariance of the action implies

$$\int_D \left(\frac{\partial \mathcal{P}}{\partial \chi} + \frac{\partial \mathcal{G}}{\partial \tau} + \alpha_0 |A|^2_\tau \mathbb{H}(|A|^2_\tau) \right) \, d\chi \, d\tau = 0, \tag{4.17}$$

where

$$\mathcal{P} = i(A^*A_\tau - AA^*_\tau), \tag{4.18}$$

and $\mathcal{G}$ is given by

$$\mathcal{G} = 2|A_\tau|^2 - (AA^*_{\tau\tau} + A^*A_{\tau\tau}) - |A|^4 \tag{4.19}$$

$$+i\beta_0|A|^2\left(A^*A_\tau - AA^*_\tau\right) - \alpha_0|A|^2\mathbb{H}(|A|^2_\tau).$$

Now, for D arbitrary, we notice that we do not have a conservation law, as the last term in parentheses in equation (4.17) cannot be written as a perfect derivative in τ. However, when D is chosen such that $\tau \in (-\infty, \infty)$, we can exploit the anti-symmetric nature of the Hilbert transform so that this term disappears, which implies

$$\frac{dP}{d\chi} = \frac{d}{d\chi}\int \mathcal{P}\, d\tau = 0. \tag{4.20}$$

Note, the conservation of P is equivalent to the statement that the mean frequency of the system does not change (*Trulsen and Dysthe* 1997, Appendix A).

Next, by using the governing equation, i.e. equation (4.3), we can confirm that

$$\frac{\partial \mathcal{P}}{\partial \chi} + \frac{\partial \mathcal{G}}{\partial \tau} + \alpha_0|A|^2_\tau\mathbb{H}(|A|^2_\tau) = 0, \tag{4.21}$$

which does not take the form of a conservation law, due to the (nonlocal) Hilbert Transform operator, which we recall arises due to the induced mean flow.

Finally, we look at the conservation law associated with χ-shift invariance. To this end, consider the transformation $A \to \tilde{A}$, $\tau \to \tilde{\tau} = \tau$, and $\chi \to \tilde{\chi} = \chi + \delta\chi$ to first order in $\delta\chi$. Following the same methodology outlined above, this invariance tells us that the conserved integral is

$$\frac{dH}{d\chi} = \frac{d}{d\chi}\int \mathcal{H}\, d\tau = 0, \tag{4.22}$$

which is the integral of the density given in equation (4.9). For clarity of presentation, the local equation corresponding to the evolution of the density $\mathcal{H}$ is not derived, as it does not contribute to the analysis given below.

4.3 Evolution of the moments of the spatial MNLSE

In this section we derive evolution equations for the first and second moments of the linear energy density.

4.3.1 Evolution of the centroid of the linear energy density

We begin by considering the motion of the *centroid* of the linear energy density of the wave packet, $\mathcal{M}$, defined as

$$\mathcal{M} = \frac{1}{\mathcal{E}} \int \tau |A|^2 \, d\tau, \tag{4.23}$$

so that, from (4.15), we have

$$\frac{d\mathcal{M}}{d\chi} = -\frac{1}{\mathcal{E}} \int \tau \frac{\partial \mathcal{J}}{\partial \tau} \, d\tau = \frac{1}{\mathcal{E}} \int \left(i \left(A^* A_\tau - A A_\tau^* \right) + \frac{\beta_0}{2} |A|^4 \right) \, d\tau \tag{4.24}$$

$$= \frac{P}{\mathcal{E}} + \frac{1}{\mathcal{E}} \int \frac{\beta_0}{2} |A|^4 \, d\tau.$$

Unlike the lower order NLSE, this quantity is in general not a constant, and depends on the magnitude of the integral of the fourth power of the modulus of the wave amplitude. Whereas $P/\mathcal{E}$ arises due to finite bandwidth effects, the second term is exclusively due to amplitude dependent nonlinear effects. We define the integral

$$\mathcal{K} = \frac{1}{\mathcal{E}} \int |A|^4 \, d\tau, \tag{4.25}$$

which serves as another measure of the distribution of the linear energy density of the wave packet. $\mathcal{K}$ is a central object in our study, and will be discussed in more detail below.

This allows us to we rewrite our evolution equation as

$$\frac{d\mathcal{M}}{d\chi} = \frac{P}{\mathcal{E}} + \frac{\beta_0}{2} \mathcal{K}. \tag{4.26}$$

The second term on the right hand side of equation (4.26) contains the coefficient β_0, which we recall arises due to the asymmetric self-steepening term in the spatial MNLSE. The integral quantity $\mathcal{K}$ is positive definite, so it will always lead to an increase in $\partial \mathcal{M}/\partial \chi$, compared to the lower order case where $\beta_0 = 0$. This is consistent with the numerical results of *Lo and Mei* (1985, see also *Trulsen* (1998), *Chereskin and Mollo-Christensen* (1985)).

We would like to connect the packet evolution in the (χ, τ) fetch reference

frame to that in the (x,t) laboratory reference frame. To this end, we define B to be the complex-valued dependent variable in the laboratory frame, so that $a_0 A \to B$. Next, we recall that the laboratory and fetch coordinate reference frames are connected by the relations given in equation (4.5). Furthermore, we define the centroid of the linear energy density in the laboratory frame as M_0, where

$$M_0 = \frac{\int t\ |B|^2 dt}{\int |B|^2\ dt}, \tag{4.27}$$

and the integration is over the duration of the wave packet. Next, we define the velocity of M_0 as U, where

$$U = \left(\frac{dM_0}{dx}\right)^{-1}. \tag{4.28}$$

This quantity can be computed in terms of $\mathcal{M}$ by noting that

$$\mathcal{M} = \epsilon 2k_0 x - \epsilon\omega_0 M_0, \tag{4.29}$$

so that

$$\frac{d\mathcal{M}}{d\chi} = \frac{1}{\epsilon^2 k_0}\frac{d}{dx}\left(\epsilon 2k_0 x - \epsilon\omega_0 M_0\right). \tag{4.30}$$

Therefore, the velocity of the centroid is given by

$$U = \frac{\omega_0}{2k_0}\left(1 - \frac{\epsilon}{2}\frac{d\mathcal{M}}{d\chi}\right)^{-1} = \frac{\omega_0}{2k_0}\left(1 - \frac{\epsilon}{2}\left[\frac{P}{\mathcal{E}} + \frac{\beta_0}{2}\mathcal{K}\right]\right)^{-1}. \tag{4.31}$$

Note, we can always choose ω_0 so that $\mathcal{P} = 0$, and will make this choice in the remainder of this subsection. Next, we map $\mathcal{K}$ back into the laboratory frame, so that at a fixed position x, we have

$$K = \frac{\int |B|^4\ dt}{\int |B|^2\ dt} = a_0^2\mathcal{K}. \tag{4.32}$$

Therefore, we arrive at one of the main results of this chapter, namely,

$$U = \frac{\omega_0}{2k_0}\left(1 - \frac{\epsilon}{2}\frac{d\mathcal{M}}{d\chi}\right)^{-1} = \frac{\omega_0}{2k_0}\left(1 - 2k_0^2 K\right)^{-1}. \tag{4.33}$$

This equation says that changes in the speed of the centroid depend on the evolu-

tion of the distribution of linear energy density in the wave group, and in particular on the integral term $K = K(x)$. As was mentioned above, K is a measure of the focusing of the linear energy density, so we expect it to increase as the packet focuses. Finally, we note that in the limit of very narrow-banded waves ($\epsilon \to 0$), our theory reproduces the linear prediction that $U = c_{go} = \partial\omega/\partial k$ (see also §4.8.2).

Note, equation (4.31) is a prescription one could apply to, for example, wave gauge measurements of the free surface elevation for waves generated in a laboratory wave channel (with the appropriate choice of ω_0).

4.3.2 Evolution of the variance for the spatial MNLSE

Next, we consider the second moment of the linear energy density. Following the literature in plasma physics (*Goldman and Nicholson* 1978, *Sulem and Sulem* 1999), the variance of the wave packet is defined as

$$\mathcal{I} \equiv \frac{1}{\mathcal{E}} \int (\tau - \mathcal{M})^2 |A|^2 \, d\tau, \tag{4.34}$$

with the nomenclature based on similar results from the N-body problem (*Robinson* 1997). The variance is sensitive to the point about which it is calculated, so that $\mathcal{M}$ provides a rational choice for the origin of our computations.

Now, differentiating $\mathcal{I}$ with respect to χ, and making use of (4.14) and integrating by parts, we have

$$\frac{d\mathcal{I}}{d\chi} = \frac{2}{\mathcal{E}} \int \tau \mathcal{J} \, d\tau - \frac{d\mathcal{M}^2}{d\chi}. \tag{4.35}$$

Next, we note that, via equation (4.15),

$$\frac{d}{d\chi}|A|^4 = 2|A|^2 \frac{\partial |A|^2}{\partial \chi} = -2|A|^2 \frac{\partial \mathcal{P}}{\partial \tau} - \frac{2\beta_0}{3} \frac{\partial |A|^6}{\partial \tau}, \tag{4.36}$$

which implies

$$\frac{\partial \mathcal{J}}{\partial \chi} = -\frac{\partial \mathcal{G}}{\partial \tau} - \alpha_0 |A|_\tau^2 \mathbb{H}(|A|_\tau^2) - \frac{\beta_0}{2} \left(2|A|^2 \frac{\partial \mathcal{P}}{\partial \tau} + \frac{2\beta_0}{3} \frac{\partial |A|^6}{\partial \tau} \right) \tag{4.37}$$

Note, the second and third terms in the above equation cannot be written as a perfect derivative in τ. Differentiating (4.35) with respect to χ again, and making use of (4.21) and (4.36), we find (ignoring terms of $\mathcal{O}(\beta_0^2)$)

$$\frac{1}{8}\frac{d^2\mathcal{I}}{d\chi^2} = \frac{H}{\mathcal{E}} - \frac{1}{8}\frac{d^2\mathcal{M}^2}{d\chi^2} + \tag{4.38}$$

$$\frac{1}{\mathcal{E}}\int \frac{1}{4}|A|^4 - \frac{\tau}{4}\left(\alpha_0|A|_\tau^2\mathbb{H}(|A|_\tau^2) - i\beta_0|A|^2\left(A^*A_\tau - AA_\tau^*\right)_\tau\right)\, d\tau.$$

When $\alpha_0 = \beta_0 = 0$, we reproduce the identity for the NLSE (see, e.g., *Sulem and Sulem* 1999). The higher order terms in the the integral in equation (4.38), i.e. those with coefficients α_0 and β_0, arise due to the inability to write them as perfect derivatives in equation (4.37). The integral $\mathcal{K}$ again arises in this relationship, which led us to search for a more physical interpretation of its origins.

Using the form of the velocity potential and free surface displacement generated in our derivation of the spatial MNLSE (see §4.8.1), we find $\mathcal{K}$ is proportional to the Lagrangian $L = L(\chi) \equiv \mathcal{T}(\chi) - \mathcal{V}(\chi)$, for $(\mathcal{T}, \mathcal{V})$ the kinetic and potential energy, respectively.

Finally, for clarity of presentation we define the last two terms on the right hand side of equation (4.38) as Ξ. Therefore, we rewrite the variance identity as

$$\frac{1}{8}\frac{d^2\mathcal{I}}{d\chi^2} = \frac{H}{\mathcal{E}} - \frac{1}{8}\frac{\partial^2\mathcal{M}^2}{\partial\chi^2} + \frac{2L}{\mathcal{E}} + \Xi. \tag{4.39}$$

Heuristically, we can think of equation (4.39) as relating changes in packet geometry to *internal* changes in the dynamics of the wave packet. Note, L is positive definite which implies that the kinetic energy will always be greater than the potential energy. Furthermore, this term provides support against the focusing of the packet. That is, we arrive at the result that the (integral) dynamical response of wave packet focusing is that the system is driven away from energy equipartition.

The behavior of the remaining terms on the right hand side of equation (4.39) are nontrivial, as they change signs throughout the focusing process. Therefore, in sections 4.5 and 4.6 we numerically integrate the MNLSE for focusing wave packets, to gain further insight into their evolution.

4.4 Numerical experiments: Numerical schemes and initial conditions for focusing packets

4.4.1 Numerical Schemes

To examine the implications of the equations derived in the previous sections we numerically solve the spatial MNLSE, i.e. (4.3) and compare these results with the wave evolution predicted by the fully-nonlinear irrotational inviscid potential flow equations for deep-water waves using the numerical scheme of Dold and Peregrine (*Dold and Peregrine* 1986, *Dold* 1992, which we denote by DP). We now briefly discuss these models.

First, the numerical scheme used to integrate the spatial MNLSE is that of *Lo* (1985, Appendix D) and *Lo and Mei* (1985, §3). This is a split-step spectral method, based on *Fornberg and Whitham* (1978). That is, the linear part of equation (4.3) is mapped into spectral space, where differentiation becomes multiplication and the subsequent ordinary differential equation is solved, and then transformed back into physical space. The nonlinear terms are more conveniently computed via pointwise multiplication (as opposed to double convolution sums in spectral space) at half time steps, where a midpoint finite-difference approximation is then used to solve for A. The integration scheme is accurate to second order in integration step size, $\Delta\tau$, and we have found that no numerical instability occurs if $\Delta\tau$ is kept sufficiently small. Note, to have the motion be 2π periodic in τ, for ease of computation, we must introduce a scale constant γ_0 into the numerics. See *Lo and Mei* (1985, see also *Lo* 1985, *Trulsen and Dysthe* 1997) for more details.

The numerical model was validated by Lo and Mei in several ways, which we have reproduced. For the examples given below, we use 2^{11} modes, with a time step on the order of 10^{-4} and take $\tau \in (0, 2\pi)$, which we ensure at the very least satisfies the Courant-Friedrichs-Lewy (CFL) condition for waves governed by linear theory, that is $N\Delta\tau/2 \leq 1$. The resolution in τ and χ were both doubled for the simulations presented below, and suitable convergence of the model was corroborated. Finally, we numerically confirmed the first integral of the spatial

MNLSE, $\mathcal{E}$, is conserved to one part in $\mathcal{O}(10^5)$ while the second integral, P, is conserved to one part in $\mathcal{O}(10^4)$.

Secondly, we used the numerical scheme of *Dold* (1992) to integrate the fully nonlinear irrotational inviscid equations governing periodic deep-water surface-gravity waves. Cauchy's integral formula is used iteratively to solve Laplace's equation, while time stepping is achieved by a truncated Taylor series, allowing for a variable time step which constrains the system to obey accuracy specifications. This is an efficient model that has been used extensively in the literature (e.g. *Dold and Peregrine* 1986, *Dold* 1992, *da Silva and Peregrine* 1990, *Cooker and Peregrine* 1992, *Banner and Song* 2002, see also *Perlin et al.* 2013). As is discussed in detail in *Dold* (1992), the model suffers from certain numerical instabilities, which are effectively removed by filtering. We monitored the total energy in the system as one way of tracking the accuracy of the model predictions. Furthermore, the resolution of the model is based on the number of surface points considered, which has the added advantage that surface points tend to cluster in regions of high curvature (*Longuet-Higgins and Cokelet* 1976), increasing the effective resolution. In our simulations, the number of points varied between 2^{11} and 2^{12}, and for all of the runs shown here we doubled the resolution to ensure suitable convergence was achieved. Finally, we note that some of the quantities we considered necessitated (up to second order) numerical differentiation, so that in some instances low pass filtering was applied to remove noise from the signal.

4.4.2 Initial conditions

Our model set of initial conditions was dispersive focusing wave packets, based on the laboratory technique originally proposed by *Longuet-Higgins* (1974) and used extensively in laboratory studies (see, for instance *Rapp and Melville* 1990, *Perlin et al.* 2013). For analytical simplicity, we assumed that there is a continuum of waves in the input packet (in the laboratory the number of waves in the input packet is typically taken to be 32: *Rapp and Melville* 1990). The initial

(linear) free-surface displacement was taken to be

$$\eta(x,t) = \int a(\omega) e^{i(k(x-x_b)-\omega(t-t_b))} + c.c.\ d\omega, \tag{4.40}$$

where x_b and t_b are phase constants that set the distance and time to breaking respectively, and ω and k are related via the linear dispersion relation for deep-water gravity waves, i.e. $\omega^2 = gk$ and *c.c.* means complex conjugate, while the reality condition demands $a(-\omega) = a^*(\omega)$ (see §4.8.2 for more details). Two parameters characterize these packets, namely the maximum linear slope predicted at breaking, S (to be defined below), and the normalized bandwidth, Δ, where

$$\Delta \equiv \frac{\omega_{max} - \omega_{min}}{\frac{1}{2}(\omega_{min} + \omega_{max})}, \tag{4.41}$$

with $\omega_{min,max}$ the minimum and maximum angular frequency, respectively, in the input wave group. The characteristic angular frequency, ω_0, is defined to be consistent with equation (4.18) (see also *Longuet-Higgins* 1957 §1.5 and *Tian et al.* 2010) so that

$$\omega_0 \equiv \frac{\int \omega |a(\omega)|^2\ d\omega}{\int |a(\omega)|^2\ d\omega}, \tag{4.42}$$

where the integration is over all frequencies. Several other features of these wave packets are discussed in §4.8.2 in the supplementary material.

The maximum linear slope, S, occurs at (x_b, t_b) according to linear theory and is given by

$$S = \int \left| a(\omega) \frac{\omega^2}{g} \right|\ d\omega. \tag{4.43}$$

Finally, the spectrally-weighted group velocity, originally proposed by *Drazen et al.* (2008), is defined as

$$c_{gs} = \frac{\int_{-\infty}^{\infty} c_g |a(\omega)|^2 d\omega}{\int_{-\infty}^{\infty} |a(\omega)|^2 d\omega}, \tag{4.44}$$

and a derivation of this equation is provided in §4.8.2. *Drazen et al.* (2008) showed that this velocity accurately described the bulk-scale evolution of the focusing wave packets they considered in the laboratory (see also *Tian et al.* 2010, *Perlin et al.* 2013). We will use c_{gs} as a reference for comparison of the results of our theory.

Next, in order to avoid the complexities associated with wave generation in our numerical schemes (see, for example, *Dommermuth et al.* 1988), we start with a packet that is fully generated at $t = 0$, so that the spatially-integrated energy is constant throughout the simulation, while the packet is windowed to make it compact in space and time (*Rapp and Melville* 1990). To generate an initial condition for the spatial evolution equations, we choose a location far enough downstream such that the entire packet passes by this point. At this location, the packet is still approximately linear, so that we use the Hilbert transform to derive a real and imaginary part of the wave packet envelope, following the procedure outlined in *Melville* (1983, §2). Note, this allows us to define a phase of the dependent variable of the MNLSE, B. Namely,

$$\theta = tan^{-1}\left(\frac{Im[B]}{Re[B]}\right), \tag{4.45}$$

where Im, Re mean imaginary and real parts, respectively. Based on this definition, we define the angular frequency ω as

$$\omega = \omega_0 - \theta_t. \tag{4.46}$$

Therefore, θ_t is the modulation to the characteristic angular frequency. Note, as one approaches the edges of these compact wave groups, $|B| \to 0$, and hence the phase is no longer well-defined (*Nye and Berry* 1974, *Melville* 1983, *Trulsen* 1998). These wave front dislocations manifest themselves as large jumps in the angular frequency (*Melville* 1983, see their figures 2b, 2c), so that to clearly display the main characteristics of the phase modulations we window these curves near the edges of the wave group.

In the next section we present a focusing wave packet with parameters $S = \Delta = 0.1$, and $f_0 = 1.0\ Hz$, while $\epsilon = 0.1$. The initial conditions are displayed in Figure 4.1, where the top panel shows η and $|B|$, at the initial spatial location. The waves and wave envelope are compact in time, and the packet is nearly symmetric. Next, the lower panel of Figure 4.1 presents the modifications to the angular frequency, and shows slower, higher frequency waves occurring before

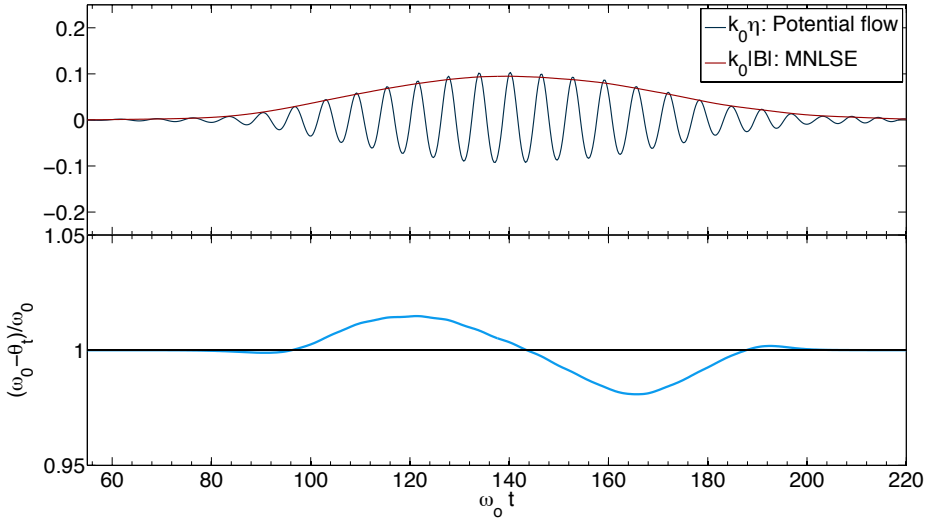

Figure 4.1: Initial conditions for a focusing wave packet with $S = \Delta = 0.1$, $f_0 = 1.0\ Hz$. Longer faster waves are put in after shorter slower waves, with constant phase parameters chosen such that (based on linear theory) the waves meet at a point in space and time. The full potential flow solution is shown in dark blue, while the wave packet governed by the MNLSE is shown in red. Note, the modulus of the envelope, $|B|$, does not contain nonlinear corrections to the free surface displacement which accounts for the discrepancy between η and $|B|$. The bottom plot shows the normalized modulations to the characteristic angular frequency $(\omega_0 - \theta_t)/\omega_0$, as predicted by the MNLSE. We see that slower (higher frequency) waves occur before faster (lower frequency) waves, which leads to packet convergence.

longer, lower frequency waves, making the packet converge in space and time.

In §4.6, we will consider a broadband wave packet, outside of the region of validity of the MNLSE, by choosing $(S = 0.25, \Delta = 0.75)$, to test the limits of our theoretical models.

4.5 Results

In this section we discuss the results of the numerical simulation when $S = \Delta = 0.1$. First, we look at the general features of the focusing event, and inspect the asymmetric evolution of the wave packet as the group converges. Secondly, we corroborate the prediction that the wave group accelerates as it focuses, appointing

the centroid of the linear energy density as an unambiguous geometric demarkation to be used in the group velocity calculation. Lastly, we look at the evolution of the variance of the wave packet.

The utility of these results are strengthened by the observation that the predictions from the theoretical models, based on the MNLSE, also accurately describe the simulations of the fully-nonlinear potential flow equations.

4.5.1 General features of the focusing wave group

An x-t diagram of the evolution of the free surface, and the wave envelope, is shown in Figure 4.2. The dark blue line represents the free surface evolution generated by the DP simulation, while the dark red line line is the behavior of the wave group, as predicted by the MNLSE. Note, we define the centroid of the DP simulations as M_D, where

$$M_D = \frac{\int t\ \eta^2\ dt}{\int \eta^2\ dt}. \tag{4.47}$$

From Figure 4.2 we see that as the wave group propagates, the longer faster waves catch up to the slower shorter waves, so that the group focuses. In the region of focusing the waves are undergoing rapid variations in space and time. The behavior of the envelope is more conspicuous, and clearly compresses as the packet focuses, and elongates after the focusing event. Finally, we define the focusing location, x_f, as the minimum of the variance, I_0, where

$$I_0 = \frac{\int (t - M_0)^2 |B|^2\ dt}{\int |B|^2\ dt}, \tag{4.48}$$

which will be discussed in more detail in §4.5.3.

The waves propagate downstream, with the wave group becoming localized as the longer faster waves catch up to the shorter slower waves. To illustrate the nature of the dispersive focusing, in Figure 4.2 the light blue lines show the angular frequency ω (equation 4.46) of the wave packet at three locations downstream. Initially, the frequency modulations are weak, and imply that higher frequency, slower waves, occur before lower frequency faster waves, leading to packet con-

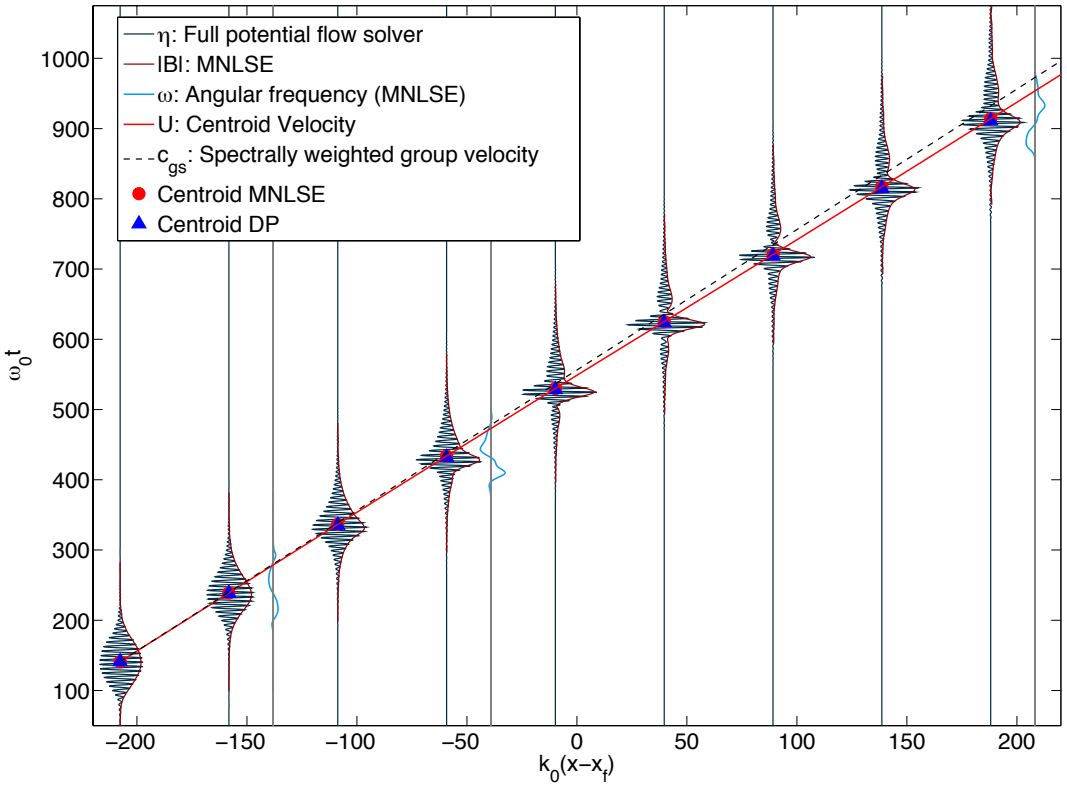

Figure 4.2: The evolution of a focusing wave packet with $S = \Delta = 0.1$. The free surface evolution from the fully-nonlinear potential flow (DP) simulation is shown in dark blue, while the wave envelope from the MNLSE simulation is in red. The centroid of these waves (DP), and the wave envelope (MNLSE), are marked by the blue triangles and the red circles, respectively. The spectrally-weighted group velocity c_{gs} (equation 4.44), is shown by the dashed black line, while U (equation 4.33), is shown by the red line. We see that c_{gs} does not capture the evolution of the centroid as the packet focuses. The locations of the centroids of the MNLSE and DP simulations are virtually indistinguishable. The light blue lines present the modulation to the angular frequency, predicted by the MNLSE, corresponding to the group shown immediately upstream of their graph. At $k_o x \approx -141$ this shows that longer waves come after shorter waves, leading to focusing, while further downstream ($k_0 x \approx 185$) this curve implies that the longer waves come before the shorter waves, implying the packet is diverging.

vergence. In the region of focusing, modulations to the frequency are relatively large, while far from the focusing event the modulations are weaker, and show the shorter slower waves occurring *after* the longer faster waves, consistent with packet divergence.

The simulation of the MNLSE agrees very well with the results of the DP simulation of the fully-nonlinear potential flow equations. At the bulk scale shown in Figure 4.2, any discrepancies between $|B|$ and the behavior of the group defined by η are nearly indiscernible, with the envelope describing the main features of the fully-nonlinear predictions. Furthermore, the motion of the centroids of both simulations (shown by the blue triangles for the DP simulation, and red discs for the MNLSE) are in good agreement. Careful inspection shows that there are differences between the two simulations as the packet focuses, which is to be expected, as $|B|$ does not contain higher order nonlinear corrections to the free surface η.

The dashed line shows the linear spectrally-weighted group velocity, c_{gs} (equation 4.44), which we see describes the evolution of the wave packet until the packet starts to experience strong modulations as it focuses. Then, it is clear that c_{gs} *underpredicts* the speed of the centroids, which is consistent with our theoretical model (to be discussed in more detail below).

Next, the evolution of the modulus of the envelope is shown in more detail in Figure 4.3. This plot is in the (χ, τ) reference frame, where we recall χ is a spatial coordinate while τ goes like minus time for fixed position (see §4.2.1). As the packet focuses, we see that it becomes asymmetric (e.g. Figure 4.3, $\chi = 4.50$), with the packet leaning backward, and steepening on its rear face (i.e. that which occurs at larger values of τ). This corresponds to the forward face in the laboratory frame, that is the face of the envelope that arrives first, being steeper than the rear face. This is consistent with equation (4.15). Initially, nonlinearity dominates dispersion and equation (4.15) behaves approximately like the inviscid Burger's equation, leading to the observed asymmetric self-steepening. As the packet continues to become more localized in τ, the terms corresponding to dispersion in equation

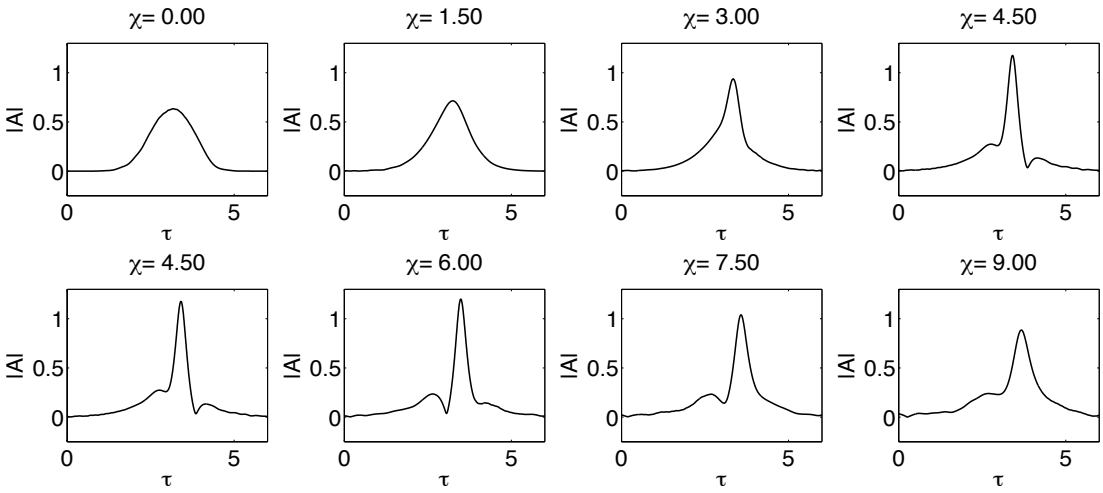

Figure 4.3: The evolution of the modulus of the wave envelope, $|A|$, in (χ, τ) coordinates. As the packet focuses, the envelope becomes asymmetric with the face at larger τ leaning forward. Recall, in the laboratory reference frame this corresponds to the forward face of the group being steeper than the rear face. This is consistent with equation (4.15), which takes the form of the inviscid Burger's equation plus a term related to dispersion. Initially, the nonlinearity dominates and leads to the observed asymmetric steepening, but as the packet localizes dispersion becomes more important and inhibits further focusing.

(4.15) become more important, and inhibit further focusing. This characterization of the forward leaning of the wave packet during focusing is in agreement with existing laboratory observations (see, for example, *Melville* 1983, *Rapp and Melville* 1990).

4.5.2 The kinematics of a focusing wave packet

We now consider modifications to the group velocity due to wave focusing. It is apparent in Figure 4.2 that there are deviations of the evolution of the centroid compared with the (constant) spectrally weighted group velocity c_{gs}. This is shown more clearly in Figure 4.4, where we present a comparison between our theoretical prediction U (equation 4.33), the spectrally weighted group velocity c_{gs}, and the predictions of the evolution of the centroids M_0, M_D. We find that U differs from c_{gs} by up to 4%, and is not constant as the wave field evolves. This is corroborated by the observations of the evolution of M_0 and M_D. We see that the two simulations

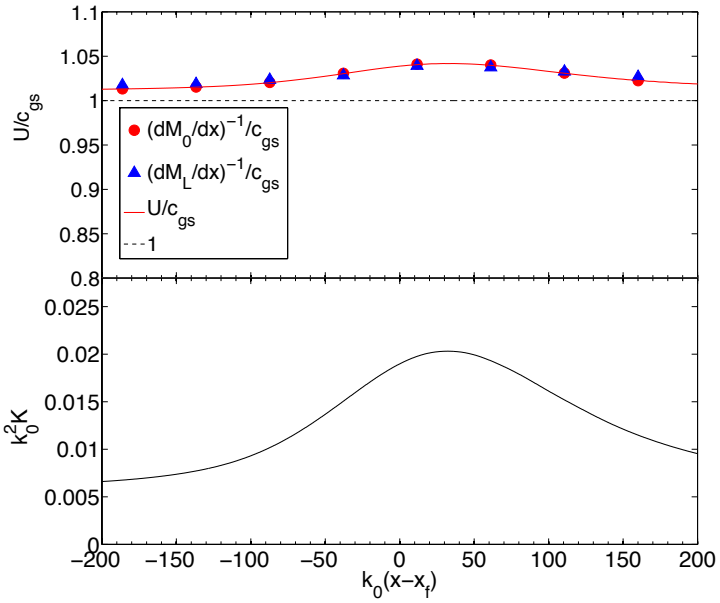

Figure 4.4: The evolution of the (normalized) speed of the centroid of the potential flow theory (blue) and the MNLSE (red), versus downstream position, for the locations shown in Figure 4.2, compared to theoretical model U, shown by the solid red line. It can be seen that both the full potential flow equations and the MNLSE are in good agreement with the theoretical model, predicting that the centroid accelerates as the packet focuses. At its maximum, U is 4% larger than c_{gs}. The bottom plot shows the quantity $k_0^2 K$, which is responsible for the modification to the speed of the packet, and increases as the packet focuses.

are in good agreement, with some small discrepancies far from the focusing region. Finally, the packet acceleration is due to variations in the integral quantity K, as discussed in §4.3.1, which is shown in the bottom half of Figure 4.4.

Note, for *breaking* wave packets, the wave spectrum downshifts as the packet focuses and breaks (*Melville* 1983, *Lo and Mei* 1985, *Trulsen and Dysthe* 1997, *Meza et al.* 2000, *Tian et al.* 2010), as breaking predominantly dissipates the shorter waves in the packet (*Rapp and Melville* 1990, *Tian et al.* 2011), leading c_{gs} to increase. Also, *Trulsen and Dysthe* (1997) found that for three dimensional wave trains, a frequency downshift can occur in the absence of dissipation. However, in our theoretical and numerical analysis of the spatial MNLSE, we have noted that the frequency remains fixed, yet the group velocity still undergoes significant variations, which we can then completely characterize as being due to the nonlinear self-steepening mechanism (see equation 4.33). The relative importance of the modification of the group velocity due to dissipation, compared with the nonlinear mechanism proposed here, is of importance, but is beyond the scope of these models and the current analysis.

4.5.3 Evolution of the variance of the wave packet

The focusing event shown in Figure 4.3 can be characterized by inspecting the local slope of the free surface. The maximum local slope, defined as $|\eta_x|$, is 0.19, and occurs at $k_0 x = 24.7$. Alternatively, we can look at a global measure of this event, namely the variance of the wave packet, and avoid the complexities associated with differentiating quantities that are rapidly varying in space and time. Furthermore, the variance will be shown to link the geometry of the wave packet to its dynamics.The variance of the packet governed by the full potential flow equations, I_D, is defined as

$$I_D = \frac{\int (t - M_D)^2 \ \eta^2 \ dt}{\int \eta^2 \ dt}. \tag{4.49}$$

Figure 4.5 shows the variance of both simulations, which monotonically decreasing until they reach a minimum. These minima are more than 25% less than their

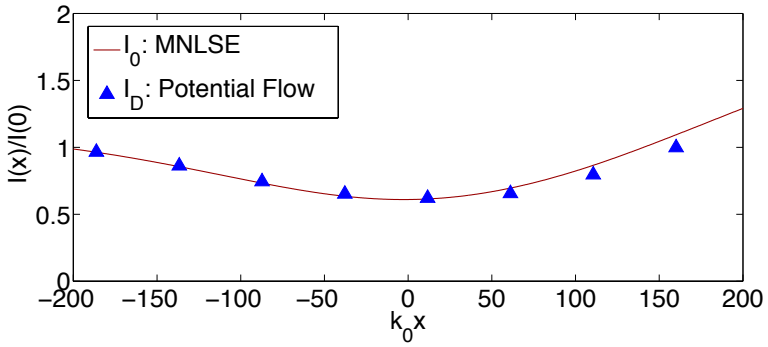

Figure 4.5: The evolution of the (normalized) variance of the wave packet governed by the MNLSE (red) and the full potential flow equations (blue triangles), the later of which is shown at the locations where the free surface is displayed in Figure 4.2. Both predictions are normalized by their values at $k_0x = -221$. The variance of both simulations monotonically decrease into the region of focusing, until they reach their minima. This occurs at $k_0x = 0$ for the MNLSE model and $k_0x = -2.1$ for the full potential flow simulation. After the focusing event, there is a slight discrepancy between the simulations, as the envelope equations do not contain the bound harmonics and higher order nonlinear corrections to the surface displacement; however, there is good agreement between the two simulations during focusing.

initial values. The MNLSE predicts that the maximum focusing occurs at $k_0x = 0$ (by definition) while the DP model predicts it occurs at $k_0x = -2.1$. We notice that the predictions of the two models differ slightly after the focusing event, as the higher harmonics generated by the DP model are not captured by the evolution of $|B|$. However, there is good agreement between the two models as the group focuses. Note, the predictions of the location of the minimum point of the variance, for both simulations, are roughly 4 wavelengths upstream of the location of the maximum slope, as well as the location of the maximum of K (which occurs at $k_0x = 31.9$), both alternative metrics for the focusing event. This is interesting, as it implies that the local signature of the focusing event, i.e. the wave slope, as well as the deviation from equipartition, are most pronounced as the packet starts to defocus.

We next examine $\mathcal{I}_{\chi\chi}$, as predicted by the MNLSE, i.e. equation (4.39). This function and the terms on the right hand side of equation (4.39) are shown in Figure 4.7. The evolution of the variance is constrained by the balance between the

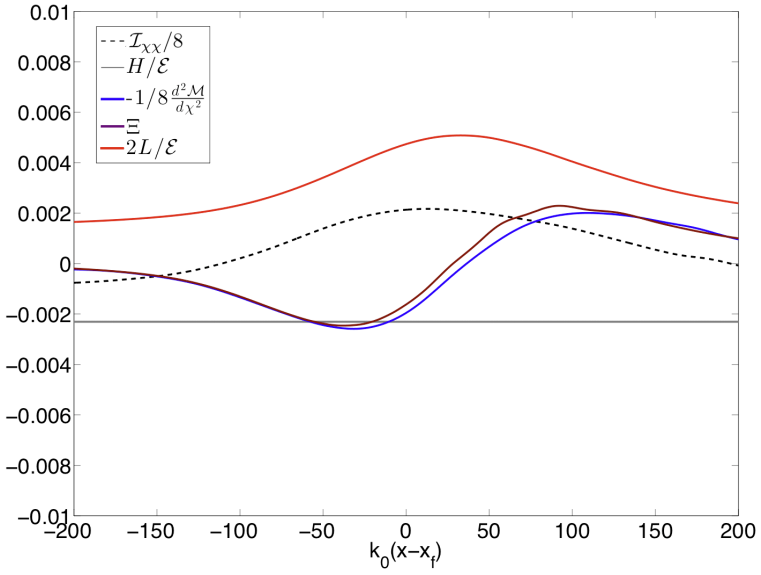

Figure 4.6: $\mathcal{I}_{xx}$, as well as the terms that govern its evolution (see equation 4.39). We see that the motion of this second derivative (dashed black line) is a balance between the tendency towards localization, provided by $\Xi, \mathcal{M}, H$ during focusing and the resistance to this focusing from the term related to the Lagrangian L. Note, the maximum of $\mathcal{I}_{xx}$ occurs downstream of the minimum of I_0.

resistance to deformation, provided by the term related to L, and the remaining terms on the right hand side of equation (4.39). H is shown numerically to be negative for this example, implying that the homogeneous solution to the variance identity (i.e. when $L = \Xi = \mathcal{M} = 0$) is a parabola with negative concavity, enhancing the tendency towards localization. The behavior of the forcing term Ξ closely follows the behavior of the evolution of the centroid squared. Both of these terms act to decrease the values of $\mathcal{I}$ during the focusing event, before changing signs. The location of their minima, which are upstream of the focal point x_f, are what lead to the discrepancy between the locations of the maximum local slope and the minimum value of I_0.

4.6 Discussion

To test the limits of our theoretical models, we consider a broadband focusing wave packet that is outside the region of validity of the MNLSE, with $S = 0.25$

and $\Delta = 0.75$ while $f_o = 0.82\ Hz$, and we choose $\epsilon = 0.25$. An x-t diagram of this wave packet is shown in Figure 4.7. The local slope, $|\eta_x|$ reaches a value of 0.31, which exceeds the steepness where one would expect the generation of parasitic capillary waves (*Fedorov and Melville* 1998) as well as 3 dimensional class II instabilities (*Melville* 1982, *Su* 1982, *McLean et al.* 1981).

From Figure 4.7a, we observe that the predictions of the MNLSE simulation agree well with those of the DP scheme. We see that the geometry of the two packets differs in several regions, yet the centroids are nearly indistinguishable. This is of considerable interest, as it implies that the bulk scale features of the fully nonlinear wave packet for this broadband initial condition are qualitatively reproduced by a significantly simpler system, namely the MNLSE.

A closer inspection of the evolution of the centroid velocity is shown in Figure 4.7b. Here, we see that the packet again accelerates as it focuses, with U reaching a value approximately 6% larger than the constant linear prediction c_{gs}. The evolution of centroid of both simulations is again well described by U, but now with some small discrepancies far from the focusing region. The variance is shown in Figure 4.7c. Analogous to the example considered in §4.5, there is good agreement between the two simulations as the packets focus, with differences becoming clear after focusing. Both have minimum values that are more than 60% less than their initial values (c.f. Figure 4.5).

The broader bandwidth allows the packet to focus more rapidly than the narrow-banded wave packet considered in §4.5, based on linear dispersion. This is clearly shown in the behavior of I. In section 5, the packet has a variance reduction that is approximately 25% of its initial value, as compared to the packet in §4.6 which experiences more than a 60% reduction in variance in the maximum region of focusing. One implication is that the weaker focusing event allows nonlinearities to act over a greater amount of space and time, compared with the broader bandwidth wave packet, which undergoes strong nonlinearities in a localized region around x_f. However, the characteristic features of both focusing events are described by our theoretical models.

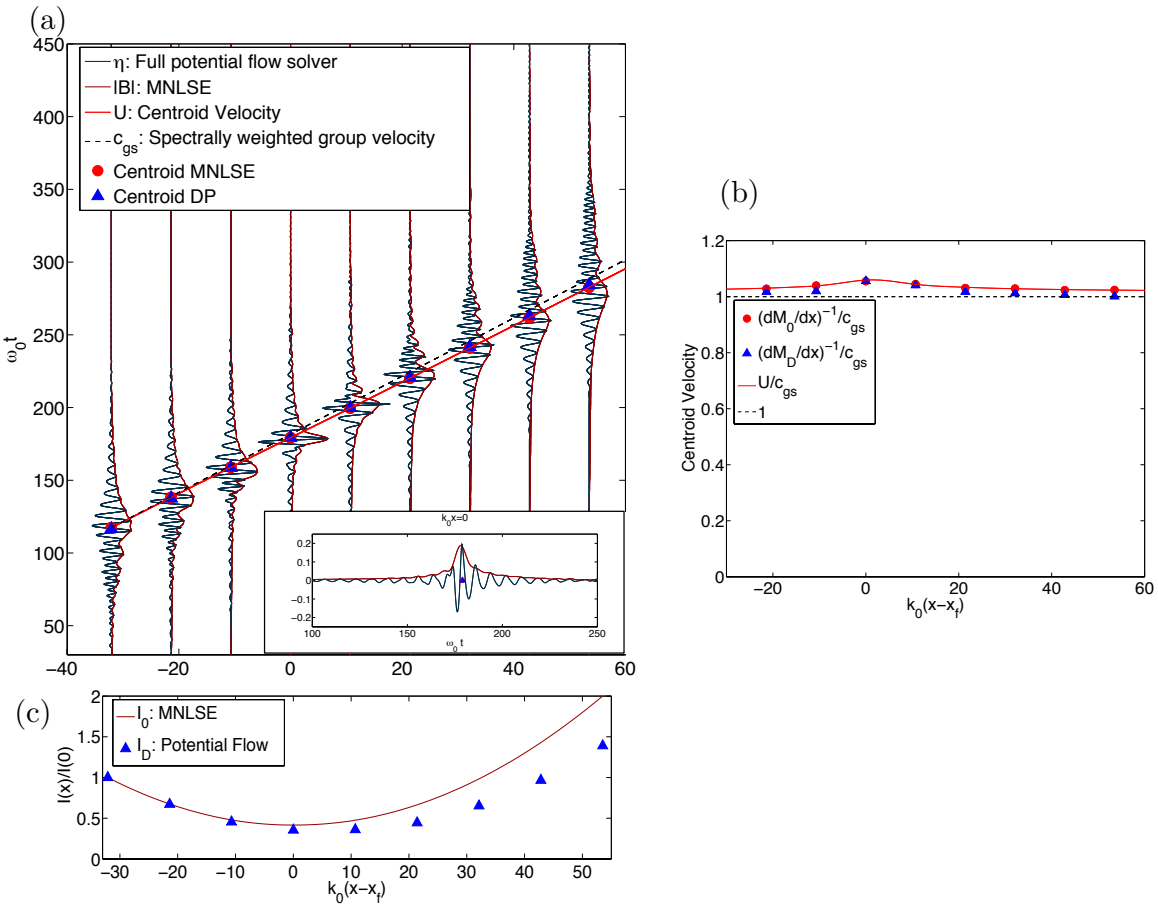

Figure 4.7: (a) An x-t diagram of a broadband focusing wave packet with $S = 0.25$, $\Delta = 0.75$, and $f_o = 0.82\ Hz$, which is outside of the region of validity of the MNLSE. The characteristic features of the focusing event are captured by the MNLSE. (b) The evolution of the normalized theoretical centroid velocity U (red line), compared with the predictions of the two numerical schemes. We see that U models the bulk-scale features of the centroid evolution of the two simulations, with the packet accelerating as it focuses, reaching a maximum value about 6% greater than the linear prediction, c_{gs}. (c) The evolution of the (normalized) variance, as predicted by the MNLSE (red line) and the DP scheme (blue triangles). There is good agreement between the two schemes as the packet focuses, with noticeable discrepancies becoming manifest in the region of maximum focusing and then during packet defocusing. Both schemes predict a reduction in variance of more than 60% their initial values in the maximum region of focusing.

4.7 Conclusion

In this study we have examined the geometry, kinematics and dynamics of focusing wave packets. Mapping the MNLSE into a spatial reference frame, with the dependent variable being the first order coefficient of the first mode of the velocity potential, has elucidated the variational structure of these equations, and allowed us to find conserved quantities and integrals of the spatial MNLSE. This then yields evolution equations for the first and second moments of the energy density of the wave group. Furthermore, inspection of these equations gives us information on the properties of waves and groups as focusing occurs.

The first conclusion is that evolution of the first moment yields a theoretical model U, accurately describing the acceleration of the energy density centroid during focusing, as simulated by *both* the MNLSE and the fully-nonlinear potential flow equations. This acceleration occurs due to the asymmetric self-steepening term in the spatial MNLSE, and the integral that governs this mechanism is a measure of the concentration of the linear energy density. The centroid velocity can be easily computed in solutions to the full nonlinear equations, or in laboratory experiments.

Secondly, the conservation law for the linear energy density yields an equation that takes the form of the inviscid Burger's equation, plus a dispersive term. This helps us characterize the asymmetric leaning of the envelope of these wave groups, which steepen on the forward face as the packet focuses.

Next, the evolution of the second moment has related the geometry of the free surface to the dynamics of the packet. Packet convergence was associated with the break down of equipartition within the wave group, with the kinetic energy becoming greater than the potential energy as the packet focuses. This inherently unsteady situation is of considerable interest in understanding the dynamics of these waves as they focus.

Finally, comparisons between simulations of the MNLSE and the fully-nonlinear potential flow equations show good agreement in the region of validity of the MNLSE. Furthermore, the qualitative features of a broadband wave packet were also described by the theoretical models, and numerical predictions, of the

MNLSE.

4.8 Supplementary material

4.8.1 Derivation of the spatial MNLSE based on Whitham's method

In this subsection we will provide a derivation of the spatial MNLSE using a variant of Whitham's method (*Whitham* 1965, 1974).

Zakharov (1968) and *Miles* (1977) showed that the governing equations for irrotational inviscid deep-water waves (see, for example *Phillips* 1977) can be derived from the action

$$S = \int \psi' \frac{\partial \eta}{\partial t} - \left(\frac{1}{2} \int_{-\infty}^{\eta} (\boldsymbol{\nabla} \phi')^2 \, dz' + \frac{1}{2} (\eta - \bar{\eta})^2 \right) \, dx \, dt, \tag{4.50}$$

where ϕ' is the velocity potential, η the free surface displacement, $\overline{\eta}'$ its phase averaged mean, and $\psi' = \phi'(x, z' = \eta, t)$, i.e. the velocity potential evaluated at the free surface. Note, the terms in the parentheses are the kinetic and potential energy densities, respectively, and that *Zakharov* (1968) showed that (η, ψ') are canonical variables of the system. Finally, the spatial scales are nondimenionalized by k_0, while temporal scales are nondimensionalized by ω_0.

Now, we would like to describe the evolution of the system in fetch coordinates, so that as in §4.2 we define $(\chi, \tau) = (x, 2x - t)$. Therefore, our new action takes the form

$$S = \int -\psi \frac{\partial \zeta}{\partial \tau} - \left(\frac{1}{2} \int_{-\infty}^{\zeta} (2\phi_\tau + \phi_\chi)^2 + \phi_{z'}^2) \, dz + \frac{1}{2} \zeta^2 \right) \, d\chi \, d\tau. \tag{4.51}$$

Next, we expand ϕ and ζ in a series (see for example *Chu and Mei* 1970)

$$\phi = \sum_{m=0}^{4} \sum_{n \geq m}^{4} \epsilon^n \phi_{nm}(\epsilon^2 \chi, \epsilon \tau) f_{nm}(z) e^{im\vartheta} e^{mz} + c.c., \tag{4.52}$$

$$\zeta = \sum_{m=0}^{4} \sum_{n \geq m}^{4} \epsilon^n \zeta_{nm}(\epsilon^2 \chi, \epsilon\tau) e^{im\vartheta} + c.c.,$$

where $\vartheta = \tau - \zeta$ and *c.c.* denotes the complex conjugate. Finally, $f_{nm}(z) = \sum_{j=1}^{n} \kappa_{nm} z^{j-1}$, for κ_{nm} constant, are introduced in order to satisfy conservation of mass (*Trulsen* 1999). The mean terms are those corresponding to $m = 0$, and we note that they have a functional dependence on a slow vertical scale, ϵz, as discussed in *Dysthe* (1979).

We choose $\phi_{11} \equiv A$ and substitute these expansions into the action, i.e. equation (4.51). The remaining terms $(\phi_{nm}, \zeta_{nm}, \kappa_{nm})$ can be found by varying the action with respect to each of these dependent variables (*Whitham* 1974, see section §14.5). This is facilitated by the symbolic manipulation software Mathematica, whence it is found that

$$\phi(\chi, \tau, z) = \epsilon^2 \bar{\phi}^{(2)} + \frac{1}{2} \left(\left[A - 2izA_\tau - \left(\frac{1}{4} + 2z^2 \right) A_{\tau\tau} - \frac{1}{2}|A|^2 A - \right. \right. \tag{4.53}$$

$$\left. \left. izA_\chi \right] e^{i\vartheta} e^z + c.c. \right).$$

The free surface is given by

$$\zeta(\chi, \tau) = \overline{\Psi_\tau}\big|_{z=0} + \frac{1}{2} \left(\left[iA + A_\tau - i\frac{3}{8}|A|^2 A + \frac{i}{4} A_{\tau\tau} + \frac{1}{2} A_\chi \right] e^{i\vartheta} + \right. \tag{4.54}$$

$$\left. \left[-\frac{1}{2} A^2 + 2iAA_\tau \right] e^{2i\vartheta} - \frac{3i}{8} A^3 e^{3i\vartheta} + c.c. \right),$$

Note, the mean term in the expansion of ζ represents the wave set up and set down.

Substituting these expansions into the action, we find that

$$S = \frac{1}{4} \int \left(\frac{i}{2} \left(AA_\chi^* - A^* A_\chi \right) - \mathcal{H} \right) \, d\tau \, d\chi \tag{4.55}$$

with $\mathcal{H}$ given by equation (4.9).

There are a number of conserved integrals for the full nonlinear inviscid irro-

tational water wave equations (*Benjamin and Olver* 1982, *Whitham* 1962, *Phillips* 1977). Integral properties of certain classes of permanent progressive waves, governed by different asymptotically valid simplified equations, derived from the full equations, have been presented by several authors (*Longuet-Higgins* 1975, *Bridges* 1992). Finally, we note that several integrals of the water wave equations have been connected to the conserved integrals of the NLSE (*Ablowitz and Segur* 1979, §2).

However, our system is more complex than the solitary wave systems considered by *Longuet-Higgins* (1975) and *Bridges* (1992), as the waves evolve in space and time. Furthermore, at higher order the phase averaging destroys the form of the conservation laws (*Whitham* 1962, §3), and significant care must be taken. Due to these difficulties, we will not derive a set of integrals, but will instead present several physically important quantities that are related to the theme of the chapter.

We consider momentum density $\mathbb{M}_0$, the kinetic energy density T_0 and the potential energy density V_0, given by

$$\mathbb{M}_0 = \int_{-\infty}^{\eta} \rho \phi_x' dz' = \int_{-\infty}^{\zeta} \rho(2\phi_\tau + \phi_\chi)\ dz, \tag{4.56}$$

$$T_0 = \frac{1}{2}\int_{-\infty}^{\zeta} \rho(2\phi_\tau + \phi_\chi)^2 + \phi_z^2\ dz; \qquad V_0 = \frac{\rho}{2}(\zeta^2 - \overline{\zeta}^2),$$

with $\overline{\zeta}$ the phase averaged mean surface height. Substituting in the expansions for (ϕ, ζ) found above, taking $\rho = 1$ from now on, and averaging over the phase ϑ, we find (where the phase averaged quantities are denoted without the subscript naught symbol)

$$m = \overline{\eta} = \frac{1}{4}\mathbb{H}(|A|_\tau^2), \tag{4.57}$$

$$\mathbb{M} = 0 + \mathcal{O}(\epsilon^3),$$

$$T = \frac{1}{4}|A|^2 + \frac{i}{4}(AA_\tau^* - A^*A_\tau) + \frac{i}{8}(AA_\chi^* - A^*A_\chi) + \frac{1}{8}|A_\tau|^2 + \mathcal{O}(\epsilon^5),$$

$$V = \frac{1}{4}|A|^2 + +\frac{i}{4}(AA_\tau^* - A^*A_\tau) + \frac{i}{8}(AA_\chi^* - A^*A_\chi) + \frac{1}{8}|A_\tau|^2 - \frac{1}{8}|A|^4 + \mathcal{O}(\epsilon^5),$$

$$L' = T - V = \frac{1}{8}|A|^4 + \mathcal{O}(\epsilon^5), \tag{4.58}$$

and

$$E = T + V = \tag{4.59}$$
$$\frac{1}{2}|A|^2 + \frac{i}{2}(AA^*_\tau - A^*A_\tau) + \frac{i}{4}(AA^*_\chi - A^*A_\chi) + \frac{1}{4}|A_\tau|^2 - \frac{1}{8}|A|^4 + \mathcal{O}(\epsilon^5).$$

Finally, we define

$$L = \int L' \, d\tau; \qquad \mathcal{T} = \int T \, d\tau; \qquad \mathcal{V} = \int L \, d\tau, \tag{4.60}$$

with the integration ranging over the duration of the wave packet.

There are several things to note. First, the integral of $\overline{\eta}$ over τ is 0, as this term can be written as a gradient. Next, the momentum is exactly zero to third order, as the momentum in the mean flow cancels that in the waves (*Longuet-Higgins and Stewart* 1962, *McIntyre* 1981). Also, as this term is linear in the velocity potential, we can only consistently calculate it to second order, as vertical integration over mean terms *reduces* the order by 1. Also, we note that equipartition breaks down at fourth order, which is analogous to the case for Stokes waves (*Longuet-Higgins* 1975, see equation (6.16)). Furthermore, we see that the integral $\mathcal{E}$ is proportional to the integral of the energy density corresponding to linear waves.

Finally, we note that the energy cannot be written as a sum of the conserved integrals found in §2.3. However, if we define a quantity analogous to the *wave action* (*Bretherton and Garrett* 1968), which we denote as $\mathcal{A}$, then we have

$$\mathcal{A} = \frac{E}{1 + \Theta_\chi} = \frac{1}{2}|A|^2 + \frac{i}{2}(AA^*_\tau - A^*A_\tau) + \frac{1}{4}|A_\tau|^2 - \frac{1}{8}|A|^4 + \mathcal{O}(\epsilon^5), \tag{4.61}$$

where we have defined Θ as the angle of A, i.e. $A = ae^{i\Theta}$, where $a = a(\epsilon^2\chi, \epsilon\tau)$ and $\Theta = \Theta(\epsilon^2\chi, \epsilon\tau)$ are real functions, while $a \sim \mathcal{O}(\epsilon)$ and $\Theta \sim \mathcal{O}(1)$.

Equation (4.61) should be compared with the classic definition of wave action in the laboratory reference frame, $E_0/\hat{\omega}$ with E_0 the energy and $\hat{\omega}$ the intrinsic frequency of the waves (*Longuet-Higgins and Stewart* 1964). In our case,

it is not the presence of a mean flow that has led to the modified conserved quantity $\mathcal{A}$, but rather it is the second order modifications to the wavenumber, Θ_χ.

Integrating $\mathcal{A}$ over all of τ, we find

$$\int \mathcal{A}\, d\tau = \frac{1}{2}\mathcal{E} + \frac{1}{2}P + \frac{1}{4}\mathcal{H}^{(4)}, \tag{4.62}$$

where $\mathcal{H}^{(4)}$ is given in equation (4.9) with $\alpha_0 = \beta_0 = 0$, so that to this order the integral of $\mathcal{A}$ is conserved.

4.8.2 Linear theory of dispersive focusing wave packets

In this subsection we highlight certain linear predictions of the dispersive focusing wave packets discussed in this work.

We begin by defining the spatial centroid of the energy density of a wave packet in the laboratory reference frame as

$$M_o' = \frac{1}{E_o}\int_{-\infty}^{\infty} x|\eta|^2\, dx, \tag{4.63}$$

where $\eta(x,t)$ is the free surface elevation and E_o is proportional to the linear energy density, which is defined as

$$E_o = \int_{-\infty}^{\infty} |\eta|^2\, dx. \tag{4.64}$$

The definition of free surface displacement is as in equation (4.40), with $x_b = t_b = 0$ here, for clarity of presentation. Now, analogous to *Drazen et al.* (2008) we define the Fourier coefficients of the surface displacement via the relations

$$a(\omega)k \;= \begin{cases} \frac{S}{2\omega_o\Delta}, & \text{If } (1-\Delta/2) \le |\frac{\omega}{\omega_o}| \le (1+\Delta/2), \\ 0, & \text{If } |\frac{\omega}{\omega_o}| \ge (1+\Delta/2) \text{ or } |\frac{\omega}{\omega_o}| \le (1-\Delta/2). \end{cases} \tag{4.65}$$

By substituting (4.40) into (4.63), we have

$$M_0' = \frac{1}{E_o}\int\int a(\omega)a^*(\omega')e^{-i(\omega-\omega')t}\left(\int_{-\infty}^{\infty} xe^{i(k-k')x}\, dx\right)\, d\omega\, d\omega', \tag{4.66}$$

We know that (see, for example, *Pope* (2000, Appendix D))

$$\int_{-\infty}^{\infty} x e^{i(k-k')x}\, dx = i\frac{\partial \delta(k-k')}{\partial k}, \tag{4.67}$$

where δ is the Dirac delta function. Putting this into (4.66), we find

$$M_0' = \frac{1}{E_o}\int_{-\infty}^{\infty} t\frac{\partial \omega}{\partial k}|a(\omega)|^2 d\omega. \tag{4.68}$$

Next, inserting equation (4.40) into (4.64), we find (via Parseval's identity)

$$E_0 = \int_{-\infty}^{\infty} |a(\omega)|^2 d\omega. \tag{4.69}$$

Note that for linear waves this term is proportional to the energy of the wave packet, and in the absence of forcing or dissipation, will be a constant in time. Therefore, we conclude

$$M_o' = \frac{t}{E_o}\int_{-\infty}^{\infty} c_g |a(\omega)|^2 d\omega. \tag{4.70}$$

where for linear waves we define $c_g = \frac{\partial \omega}{\partial k} = 1/2\sqrt{g/k}$. Now, the evolution of the centroid will be given by the time rate of change of this quantity, that is

$$\frac{dM_o'}{dt} = \frac{\int_{-\infty}^{\infty} c_g |a(\omega)|^2 d\omega}{\int_{-\infty}^{\infty} |a(\omega)|^2 d\omega}, \tag{4.71}$$

which is precisely the quantity (in the continuum limit) that *Drazen et al.* (2008) used to quantify the group velocity of a focusing wave packet. Specifically, with

$$a(\omega) = \frac{\delta(\omega - \omega_i)}{2}\frac{S}{32}\frac{g}{\omega^2}, \tag{4.72}$$

where $\omega_i = \omega_o + (i - 32/2) * d\omega/32$ and $i = 1, 2, ...32$, we return to the discrete spectrally weighted group velocity of (*Drazen et al.* 2008, their equation 4.5), c_{gs}:

$$c_{gs} = \frac{\sum_{n=1}^{32} c_{gn} a_n^2}{\sum_{n=1}^{32} a_n^2}; \qquad c_{gn} = \frac{\sqrt{g}}{2\sqrt{k_n}}. \tag{4.73}$$

Note, this relation can be derived by classical methods, by considering the

ratio of the energy flux density, to the energy flux, for these linear focusing wave packets.

This chapter has been submitted for publication to the Journal of Fluid Mechanics as "Wave modulation: The geometry, kinematics, and dynamics of surface-wave focusing" by Pizzo, N.E. and Melville, W.K. The dissertation author was the primary investigator and author of this paper.

A A Lagrangian for deep-water waves

A.1 Introduction

In this appendix, we analytically develop an exact set of equations describing deep-water irrotational surface gravity waves, originally proposed by *Balk* (1996), and advanced for the case of standing waves by *Longuet-Higgins* (2000, 2001), and put them in a form more suitable for practical applications. A truncated model for permanent progressive waves is examined, and conditions under which solutions exist are presented. Furthermore, we use Stokes waves to corroborate our numerical scheme, and model the overturning of a steep Stokes wave due to a superharmonic perturbation. Future work will involve using this model to investigate the predictability of the onset of wave breaking for these perturbed steep Stokes waves.

Nonlinear surface wave models are a powerful tool for studying complex wave scenarios, and in particular for investigating wave properties as waves become highly nonlinear and break. An improved description of the dynamics of surface water waves, and their behavior under these nonlinear conditions, is crucial for a better understanding of air-sea interaction processes (*Melville* 1996). Nonlinear surface waves pose a formidable theoretical problem, and analytical studies of weakly nonlinear waves have led to a better understanding of water wave phenomena, but these results are limited by their restriction to weak nonlinearities. That is, many of these theoretical predictions are far outside of their region of validity as wave breaking is approached and during the subsequent breaking event. For

this reason, numerical models of surface waves can provide insight into the physics of highly nonlinear waves processes. In this appendix we analyze, and develop, the model of *Balk* (1996), based on a Lagrangian for deep-water surface gravity waves.

Irrotational inviscid surface waves are governed by Laplace's equation, together with conditions along the boundary of the fluid. Although Laplace's equation is linear, the two free surface boundary conditions, namely the kinematic condition constraining fluid particles on the surface to stay on the surface, and the dynamic boundary condition, mandating continuity of pressure at the interface, are: (i) coupled to the velocity potential; (ii) nonlinear; (iii) evaluated at one of the dependent variables of the system, namely the (spatially and temporally dependent) free surface. In particular, condition (iii) makes solving these equations a formidable challenge.

The pioneering study of *Longuet-Higgins and Cokelet* (1976) showed that the equations of motion could be numerically integrated, allowing for the systematic examination of properties of waves up to and past the point of overturning. The method employed by *Longuet-Higgins and Cokelet* (1976) used a Green's identity to solve Laplace's equation, which was then used to time-step the velocity potential and the free surface displacement. This scheme is Lagrangian in nature, with particles on the free surface serving as the dependent variables of the system. Additionally, this method is advantageous because the points tend to cluster around the regions of highest curvature, so that one can resolve wave overturning with relatively few surface points.

The method of *Balk* (1996) takes a different approach to describing two dimensional surface gravity waves. At each point in time, the free surface is conformally mapped to a periodic lower-half plane in the complex domain. The geometry of this domain makes solving Laplace's equation trivial, greatly reducing the work needed for this operation. The governing equations then can be simply written as a set of coupled low order polynomial ordinary differential equations in the dependent variables, which are Fourier coefficients of the free surface displacement. The computational cost of the model is then related to the speed at which the Fourier series converge. These convergence rates are related to the proxim-

ity of the nearest singularity (which lie above the free surface) to the free surface (*Fornberg* 1980, *Meiron et al.* 1981, *Sulem et al.* 1983, *Balk* 1996) in the complex plane. As a wave overturns, a curvature singularity approaches the free surface (*Baker and Xie* 2011), which greatly reduces the speed at which the Fourier series converges, making the model computationally expensive for these wave scenarios. Therefore, one must be careful to optimize the numerical implementation of the model.

The scheme of *Balk* (1996) is derived from Hamilton's principle, applied to the action describing irrotational inviscid water waves. This is advantageous as one knows the form of the conserved quantities (e.g. energy, mass and momentum) when numerical approximations are necessarily applied. Furthermore, the set of coupled equations one arrives at are all lower order polynomials in the dependent variables, making the numerical implementation straight forward (*Longuet-Higgins* 2000). Before developing the model, it is prudent to review the variational structure of water waves.

A.1.1 A review of the variational principle applied to water waves

The governing equations for two-dimensional irrotational surface gravity waves can be found via Hamilton's principle (see, for instance, *Whitham* 1974) by finding stationary points of the action S, where

$$S = \int \mathcal{L}\, dxdt, \tag{A.1}$$

and $\mathcal{L}$ is the Lagrangian density. Here, we take x to be the along wave direction and let y be pointed vertically upwards. *Luke* (1967) first wrote down the Lagrangian (density) for these waves:

$$\mathcal{L} = -\int_{-\infty}^{\eta} \left(\phi_t + \frac{1}{2}(\nabla\phi)^2 + gy \right)\, dy, \tag{A.2}$$

where $\eta(x,t)$ is the height of the free surface from the quiescent level $y = 0$, $\phi(x,y,t)$ is the velocity potential, and g is the acceleration due to gravity.

Variations of S give us the governing equations for irrotational two-dimensional surface gravity waves (via integration by parts and Leibniz's rule)

$$\delta S = \int dxdt\ \delta\eta \left(\phi_t + \frac{1}{2}(\nabla\phi)^2 + gy\right)\Big|_{y=\eta} \tag{A.3}$$

$$+ \int dxdt \left[\left(\int_{-\infty}^{\eta} -\delta\phi(\phi_{xx} + \phi_{yy})\ dy\right) - \delta\phi\ (\eta_t + \phi_x\eta_x - \phi_y)|_{y=\eta} - \delta\phi\ \phi_y|_{y\to-\infty}\right],$$

where δ is the functional derivative (see, for instance, *Salmon* 1998).

Hamilton's principle requires the action to be stationary under these variations, which implies

$$\phi_{xx} + \phi_{yy} = 0, \tag{A.4}$$

with dynamic boundary condition

$$\left(\phi_t + \frac{1}{2}(\nabla\phi)^2 + gy + \frac{P}{\rho} = 0\right)\Big|_{y=\eta}, \tag{A.5}$$

(we assume the atmospheric pressure, surface tension and viscosity are 0, so that $P = 0$) as well as the kinematic boundary condition

$$(\eta_t + \phi_x\eta_x - \phi_y = 0)|_{y=\eta}, \tag{A.6}$$

and finally the requirement of no flow at the bottom:

$$\phi_y \to 0 \quad \text{as} \quad y \to -\infty. \tag{A.7}$$

These equations govern inviscid irrotational two-dimensional deep water surface gravity waves.

Zakharov (1968) and *Miles* (1977) noted that the variational description proposed by *Luke* (1967) was not canonical, in the sense that the variables (η, ϕ) did not lead to the standard form of Hamilton's equations (see also, for instance, *Goldstein* 1965). Instead, they found that the action (which is a dynamical exten-

sion of Dirichlet's principle for potential theory, see *Serrin* 1959, §34)

$$S' = \int \mathcal{L}\, dxdt = \int \psi\eta_t - \mathcal{H}(\psi,\eta)\, dxdt = \int (\mathcal{T}-\mathcal{V})\, dxdt, \tag{A.8}$$

where $\psi \equiv \phi(x,\eta,t)$, $\mathcal{H}$ is the Hamiltonian density defined as

$$\mathcal{H} = \frac{1}{2}\int_{-\infty}^{\eta} (\nabla\phi)^2 dy + \frac{1}{2}g\eta^2 \tag{A.9}$$

and is given as $\mathcal{T}+\mathcal{V}$, which represent the kinetic and potential energy density, respectively, yields the canonical form of Hamilton's equations. That is

$$\frac{\partial\eta}{\partial t} = \frac{\delta\mathcal{H}}{\partial\psi}; \qquad \frac{\partial\psi}{\partial t} = -\frac{\delta\mathcal{H}}{\partial\eta}. \tag{A.10}$$

We now use this formulation of the Lagrangian to derive the equations for surface waves in a conformally mapped reference frame.

The purpose of the current appendix is to show how the equations of Balk can be put in a more suitable form for theoretical and numerical development. Furthermore, we will examine some of the applications of this description of water waves. The outline of this appendix is as follows. First, in §A.2 we derive the model of Balk. In §A.3 the equations are put in a form more suitable for numerical implementation. We then explore some of the implications of this formulation of the water wave problem in §A.4. Next, in §A.5 we consider a truncated model. Finally, in §A.6 we examine an overturning surface gravity wave. Further areas of interest are then discussed in §A.7.

A.2 Derivation of the equations of Balk

In this section we derive the governing equations for irrotational surface gravity waves in a conformally mapped reference frame. This formulation has a number of distinct advantages, including the ability to model wave overturning, a knowledge of the (necessarily) truncated properties of the waves (i.e. energy,

momentum), and a relatively straightforward recipe for numerical implementation. That is, although the model is algebraically intensive, the tools needed to derive these results are classical (c.f. the boundary integral methods of *Longuet-Higgins and Cokelet* (1976) and *Dold and Peregrine* (1986)).

Instead of following Balk directly, we make use of some results from *Dyachenko et al.* (1996) and show how this approach leads to a more natural formulation of the governing equations originally found by Balk.

To this end, we consider irrotational two-dimensional inviscid flow in a fluid of infinite depth with a free surface. Density and the gravity constant are set to 1 and the flow is assumed to be λ periodic in the x-coordinate, with this wavelength set to $\lambda = 2\pi$.

The domain in the complex plane of the fluid is given by $z = x + iy$, which can be considered to be the conformal image of the lower half plane described by $\zeta = \xi + i\mu$ (these variables are time dependent, but this is not explicitly written now for clarity of presentation).

The transformation from the (ξ, μ) plane to the (x, y) plane is given by $z(\zeta) = x(\xi, \mu) + iy(\xi, \mu)$. The velocity of fluid $w = u + iv$ is given by the complex potential $f(z) = \alpha(x, y) + i\beta(x, y)$ (here α and β represent the velocity potential and stream function, respectively, and we assume they satisfy the condition $v \to 0$ as $y \to -\infty$). That is,

$$w^* = \frac{df}{dz} = \left(\frac{d\mathcal{C}}{d\zeta}\right)\left(\frac{dz}{d\zeta}\right)^{-1}, \tag{A.11}$$

where $\mathcal{C}(\zeta) = a(\xi, \mu) + ib(\xi, \mu)$ is the complex potential in the ζ plane and * denotes the complex conjugate. The surface of the fluid is going to be the image of the real axis in the ζ-plane, i.e.

$$X(\xi) \equiv x(\xi, 0); \quad Y(\xi) \equiv y(\xi, 0), \tag{A.12}$$

and the surface values of the velocity potential and stream function are

$$A(\xi) \equiv a(\xi, 0); \quad B(\xi) \equiv b(\xi, 0). \tag{A.13}$$

We note that (X, Y, A, B) completely determine the state of the fluid. Actually, knowledge of $(Y(\xi), B(\xi))$ are sufficient to completely characterize the fluid, since the boundary values of the real parts of analytic functions can be found from the imaginary parts via the Hilbert Transform.

Recall, in the x-y plane, we have from *Miles* (1977) that the action for water waves can be written as

$$S = \int \left(\psi \eta_t - \int_{-\infty}^{\eta} \frac{1}{2} (\nabla \phi)^2 \, dy + \frac{1}{2} \eta^2 \right) \, dx \, dt, \tag{A.14}$$

where, $\psi = \phi(x, \eta, t)$.

Now, the time derivative of the free surface η can be rewritten in terms of the conformal variables as (c.f. *Dyachenko et al.* 1996, equation (2.14))

$$\begin{aligned} \eta_t dx &= \left(\frac{dY}{dt} \frac{dX}{d\xi} - \frac{dX}{dt} \frac{dY}{d\xi} \right) d\xi \\ &= \dot{Y} X' d\xi - \dot{X} Y' d\xi, \end{aligned} \tag{A.15}$$

where dots and primes represent differentiation with respect to time and ξ, respectively. Therefore, this term in the action becomes

$$\int \psi \eta_t \, dx = \frac{1}{2\pi} \int_0^{2\pi} A(\dot{Y} X' - \dot{X} Y') d\xi. \tag{A.16}$$

Next, the kinetic and potential energy densities, per unit wavelength, can be written as

$$V = \frac{1}{2} \int \eta^2 \, dx = \frac{1}{2} \frac{1}{2\pi} \int_0^{2\pi} Y^2 X' \, d\xi, \tag{A.17}$$

while the kinetic energy density is given by (via a Green integral identity)

$$T = \frac{1}{2} \int \left\{ (\alpha_x)^2 + (\alpha_y)^2 \right\} \, dy \, dx = -\frac{1}{2} \frac{1}{2\pi} \int_0^{2\pi} A B' \, d\xi. \tag{A.18}$$

Finally, exploiting the analyticity of $\mathcal{C}$, we can use the Cauchy-Riemann equations

to rewrite (A.14) as

$$S = \int_{t_a}^{t_b} \left\{ \frac{1}{2\pi} \int_0^{2\pi} A(\dot{Y}X' - \dot{X}Y') + \frac{1}{2}AB' - \frac{1}{2}Y^2X' \, d\xi \right\} \, dt, \tag{A.19}$$

with the time interval (t_a, t_b) chosen so that the dependent variables are fixed at these times.

Now, variations of S with respect to A gives

$$B' = (\dot{X}Y' - \dot{Y}X'), \tag{A.20}$$

which is precisely the kinematic boundary condition, equation (A.6), in the conformally mapped coordinates (equation (2) in the paper of Balk). The constraint that mass is conserved is the condition

$$\frac{d}{dt} \int \eta \, dx = \frac{d}{dt} \frac{1}{2\pi} \int_0^{2\pi} YX' \, d\xi = 0, \tag{A.21}$$

so that taking the constant of integration to be 0, corresponding to the mean water level being at $y = 0$, we find

$$\frac{1}{2\pi} \int_0^{2\pi} YX' \, d\xi = 0, \tag{A.22}$$

which is equation (3) in Balk.

Substituting (A.20) into (A.19) we find that the action becomes

$$S = \int_{t_a}^{t_b} T - V \, dt, \tag{A.23}$$

with the constraint given in (A.22). In the derivation given above, the constraints on the system enter naturally by a change of variables of the Lagrangian of Miles, whereas in Balk's derivation, he simply imposes these conditions. Both approaches constrain the system to obey conservation of mass, the kinematic boundary condition, and the condition of no flow at the bottom. Therefore, these constraints imply that by setting the Lagrangian equal to the difference of kinetic

and potential energies, and varying the associated action, we find the governing equations for water waves (see the discussion in *Luke* 1967).

The constraint of conservation of mass can explicitly be built into the Lagrangian by exploiting the periodicity of the flow in the x-direction. This property implies the following Fourier expansions:

$$X(\xi,t)+iY(\xi,t)=\xi+\sum_{k=-\infty}^{\infty}(X_k(t)+iY_k(t))e^{-ik\xi}, \tag{A.24}$$

and

$$A(\xi,t)+iB(\xi,t)=\sum_{k=-\infty}^{\infty}(A_k(t)+iB_k(t))e^{-ik\xi}, \tag{A.25}$$

where we also must have $Y_{-k}=Y_k^*, X_{-k}=X_k^*, A_{-k}=A_k^*, B_{-k}=B_k^*$ for (X,Y,A,B) to be real. The Hilbert transform then implies $(k\neq 0)$

$$X_k=i\sigma_k Y_k, \quad A_k=i\sigma_k B_k, \tag{A.26}$$

where $\sigma_k=(1,0,-1)$ for $(k>0, k=0, k<0)$, respectively. This gives us the relationships between the real and imaginary parts of the conjugate pairs. We note explicitly:

$$X=\xi+\sum_{1}^{\infty}2Re[Y_k]\sin k\xi-2Im[Y_k]\cos k\xi \tag{A.27}$$

$$Y=Y_0+\sum_{1}^{\infty}2Re[y_k]\cos k\xi+2Im[Y_k]\sin k\xi; \tag{A.28}$$

$$\xi\in(0,2\pi), \tag{A.29}$$

where Re/Im stand for the real and imaginary parts, respectively.

Using the kinematic boundary condition, i.e. equation (A.20), we find (for $n\neq 0$)

$$B_n=\frac{i}{n}\left\{-\dot{Y}_n+\sum_{k+j=n}\dot{Y}_kY_jj(\sigma_k-\sigma_j)\right\}. \tag{A.30}$$

The complex potential is defined up to an arbitrary constant, so that without loss

of generality, we can also set $A_0 = B_0 = 0$.

Substituting the Fourier expansions of (A, B) into the equation for the kinetic energy, i.e. equation (A.18), we find

$$T = \frac{1}{2} \sum_{k=-\infty}^{\infty} |k| B_k B_{-k}. \tag{A.31}$$

Similarly, with these expansions the potential energy is found directly from (A.17) and (A.24) (see also *Longuet-Higgins* 2000):

$$V = \frac{1}{2} \sum_{k=-\infty}^{\infty} Y_k Y_{-k} + \frac{1}{2} \sum_{k+j+l=0} |l| Y_k Y_j Y_l. \tag{A.32}$$

The Lagrangian, $L = T - V$, can now be written as

$$L = \frac{1}{2} \sum_{k=-\infty}^{\infty} |k| B_k B_{-k} - \frac{1}{2} \sum_{k=-\infty}^{\infty} Y_k Y_{-k} - \frac{1}{2} \sum_{k+j+l=0} |l| Y_k Y_j Y_l, \tag{A.33}$$

where B_k is given in (A.30) and we choose Y_0 to satisfy the constraint given in (A.22), namely,

$$Y_0 = - \sum_{k=-\infty}^{\infty} |k| Y_k Y_{-k}. \tag{A.34}$$

The two most obvious conserved quantities associated with this Lagrangian are the x-momentum (associated with phase shift invariance), defined as

$$\mathcal{P} = \int \beta_y \, dx \, dy = -\frac{1}{2} \frac{1}{2\pi} \int_0^{2\pi} B X' \, d\xi = \sum_{k=-\infty}^{\infty} |k| B_k Y_{-k}, \tag{A.35}$$

and energy (associated with time shift invariance) given by

$$H = \frac{1}{2} \sum_{k=-\infty}^{\infty} |k| B_k B_{-k} + \frac{1}{2} \sum_{k=-\infty}^{\infty} Y_k Y_{-k} + \frac{1}{2} \sum_{k+j+l=0} |l| Y_k Y_j Y_l. \tag{A.36}$$

Next, the governing equations are found by varying the Lagrangian (A.33) with

respect to Y_k. This yields the Euler-Lagrange equations for each mode k:

$$\frac{d}{dt}\left(\frac{\partial L}{\partial \dot{Y}_k}\right) = \frac{\partial L}{\partial Y_k}. \tag{A.37}$$

We now develop these equations further to put them in a form more suitable for numerical implementation. Before going into those details, we make some qualitative remarks about the model developed in this section. For *partial* wave solutions, the infinite sums used in the Fourier expansion of the dependent variables will be truncated at a finite N, so that we will have a truncated Lagrangian $L_N = T_N - V_N$. This is advantageous since we know the conserved quantities associated with this truncated Lagrangian *before* deriving the dynamical evolution equations (see Salmon 1988 for a thorough discussion).

A.3 Development for numerical implementation

In order to implement the above equations numerically, we make a straight forward extension of *Longuet-Higgins* (2000, 2001) from the special case of standing waves to the more general equations of motion. This analytical work elucidates the mathematical structure of this rather esoteric presentation of the water wave equations.

Following *Longuet-Higgins* (2000, 2001), we find it convenient to renormalize our dependent variables so that

$$a_n = \begin{cases} 2|n|Y_n & : n \neq 0; \\ 1 & : n = 0. \end{cases}$$

We seek to rewrite the governing equations in these variables. Note, the variables a_n can be complex valued, unlike the variables in *Longuet-Higgins* (2000, 2001) which were restricted to the real domain.

To begin with, we note that Y_0 becomes

$$Y_0 = -\frac{1}{2}\sum_{k=1}^{\infty} \frac{a_k a_{-k}}{|k|} \tag{A.38}$$

Additionally, from (A.31), we have, for $n > 0$.

$$inB_n = ... + a_{n+2}\dot{Y}_{-2} + a_{n+1}\dot{Y}_{-1} + \frac{1}{2}a_n\dot{Y}_0 + a_0\dot{Y}_n + a_{-1}\dot{Y}_{n+1} + a_{-2}\dot{Y}_{n+2} + ... \quad \text{(A.39)}$$

and similarly for $n < 0$

$$inB_n = ... + a_2\dot{Y}_{n-2} + a_1\dot{Y}_{n-1} + a_0\dot{Y}_n + \frac{1}{2}a_n\dot{Y}_0 + a_{n-1}\dot{Y}_1 + a_{n-2}\dot{Y}_2 + ... \quad \text{(A.40)}$$

By substituting these two expressions into (A.31) we find that we can write the kinetic energy as

$$4T = \sum_{m=1}^{N}\left(\sum_{k=-N}^{N} P_{mk}\dot{a}_k\right)\left(\sum_{l=-N}^{N} P_{-ml}\dot{a}_l\right) \quad \text{(A.41)}$$

where

$$P_{mn} = \frac{1}{\sqrt{[m][n]}}\left(f(m-n)a_{m-n} - \frac{1}{2}a_m a_{-n}\right), \quad \text{(A.42)}$$

the operator $[*]$ is defined as

$$[j] = \begin{cases} |j| & : j \neq 0 \\ 1 & : j = 0, \end{cases}$$

and

$$f(m-k) = \begin{cases} 0 & : \ Sign(k) = Sign(m-k); \\ 1 & : \text{otherwise} \end{cases}$$

and $a_k \equiv 0$ when $k > N$ for N the number of Fourier modes in our model, i.e. the resolution. Note, by construction, the first term in parentheses in equation (A.41) is the complex conjugate of the second term.

By using these definitions, and reversing the order of summation, the kinetic energy can be rewritten as

$$T = \sum_k \sum_l Q_{kl}\dot{a}_k\dot{a}_l \quad \text{(A.43)}$$

where

$$Q_{kl} = \frac{1}{4}\sum_{m=1}^{N} P_{mk}P_{-ml}. \tag{A.44}$$

That is, the matrix Q_{ij} is related to the column by column multiplication of two P_{mn} matrices. We next use this compact notation to further develop the equations of motion.

A.3.1 The equations of motion

We now use these definitions to solve for the equations of motion.

First, we note that the Euler-Lagrange equations in these new coordinates take the form

$$\frac{d}{dt}\left(\frac{\partial L}{\partial \dot{a}_k}\right) = \frac{\partial L}{\partial a_k}. \tag{A.45}$$

Substituting the kinetic energy into the first term of these equations, we find

$$\frac{d}{dt}\left(\frac{\partial T}{\partial \dot{a}_n}\right) = \frac{d}{dt}\left(\frac{\partial}{\partial \dot{a}_n}\right)\sum_k\sum_l Q_{kl}\dot{a}_k\dot{a}_l = \frac{d}{dt}\left(\sum_l Q_{kn}\dot{a}_k + \sum_l Q_{nl}\dot{a}_l\right) \tag{A.46}$$

$$= \sum_k Q_{nk}\ddot{a}_k + \sum_l Q_{nl}\ddot{a}_l + \sum_k \frac{dQ_{kn}}{dt}\dot{a}_k + \sum_l \frac{dQ_{nl}}{dt}\dot{a}_l.$$

Next, we note that

$$\frac{dQ_{kn}}{dt} = \sum_j \frac{\partial Q_{kn}}{\partial a_j}\dot{a}_j, \tag{A.47}$$

which implies that (A.46) becomes

$$\sum_k Q_{nk}\ddot{a}_k + \sum_l Q_{nl}\ddot{a}_l + \sum_k\sum_l \frac{\partial Q_{kn}}{\partial a_l}\dot{a}_l\dot{a}_k + \frac{\partial Q_{nl}}{\partial a_k}\dot{a}_l\dot{a}_k. \tag{A.48}$$

Finally, we note that the second term in the Euler-Lagrange equation, equation (A.45), pertaining to the kinetic energy is given by

$$\frac{\partial T}{\partial a_n} = \sum_k\sum_l \frac{\partial Q_{kl}}{\partial a_n}\dot{a}_k\dot{a}_l. \tag{A.49}$$

Putting all of this together, we see that our governing equations are now of the

form

$$\sum_k Q_{kn}\ddot{a}_k + \sum_l Q_{nl}\ddot{a}_l + \sum_k \sum_l \left(\frac{\partial Q_{kn}}{\partial a_l}\dot{a}_l\dot{a}_k + \frac{\partial Q_{nl}}{\partial a_k}\dot{a}_l\dot{a}_k - \frac{\partial Q_{kl}}{\partial a_n}\dot{a}_k\dot{a}_l \right) \tag{A.50}$$

$$-\frac{\partial V}{\partial a_n} = 0,$$

for each $n = (\pm 1, \pm 2, ... \pm N)$.

Further simplifications of these equations can be made by realizing that

$$\frac{\partial Q_{kl}}{\partial a_n} = \frac{\partial}{\partial a_n}\sum_m P_{mk}P_{-ml} = \sum_m \frac{\partial P_{mk}}{\partial a_n}P_{-ml} + P_{mk}\frac{\partial P_{-ml}}{\partial a_n}. \tag{A.51}$$

From the definition of P_{ij}, i.e. equation (A.42), we find that

$$\frac{\partial P_{mk}}{\partial a_n} = \frac{1}{[k]\sqrt{[m]}} \begin{cases} f(m-k) & : m-k-n = 0; \\ -\frac{a_m}{2} & : k+n = 0; \\ -\frac{a_{-k}}{2} & : m-n = 0. \end{cases}$$

Next, we consider the potential energy term, which, from equation (A.17), can be written as

$$2V = -\left(\sum_{n=1}^{\infty} \frac{a_n a_{-n}}{2n} \right)^2 + \sum_{n=1}^{\infty} \frac{a_n a_{-n}}{2n^2} + \tag{A.52}$$

$$+ \sum_{i=-\infty}^{\infty} \sum_{j=-\infty}^{\infty} \sum_{k=-\infty}^{\infty} F(i,j,k)\frac{a_i a_j a_k}{8[j][k]},$$

where

$$F(i,j,k) = \begin{cases} 1 & : i+j+k = 0 \quad \& \quad i,j,k \neq 0; \\ 0 & : \text{otherwise.} \end{cases}$$

To find $\partial V/\partial a_n$, we note that

$$\frac{\partial V}{\partial a_m} = \sum_{k=-\infty}^{\infty} \frac{\partial Y_k}{\partial a_m}\frac{\partial V}{\partial Y_k}, \tag{A.53}$$

where

$$\frac{\partial Y_k}{\partial a_m} = \begin{cases} \frac{1}{2|k|} & : k = m; \\ -\frac{1}{2}\frac{a_{-m}}{|m|} & : k = 0 \\ 0 & : else \end{cases}$$

Finally, we define

$$S_n(k,l) = \left(\frac{\partial Q_{lk}}{\partial a_n} - \frac{\partial Q_{nl}}{\partial a_k} - \frac{\partial Q_{ln}}{\partial a_k} \right), \tag{A.54}$$

so that the governing equation becomes

$$\sum_l (Q_{nl} + Q_{ln})\ddot{a}_l = \sum_l \sum_k S_n(k,l)\dot{a}_k\dot{a}_l + \frac{\partial V}{\partial a_n} \qquad (n = \pm 1, \pm 2, ...). \tag{A.55}$$

Note, this can be written more concisely as

$$\mathbb{Q}_{nl}\ddot{a}_l - S_{nkl}\dot{a}_k\dot{a}_l - \frac{\partial V}{\partial a_n} = 0; \qquad (n = \pm 1, \pm 2, ...) = 0 \tag{A.56}$$

where $\mathbb{Q}_{nl} = Q_{nl} + Q_{ln}$, and Einstein summation is assumed. Together with initial conditions at time $t = 0$ for a_n and $\dot{a}_n$, (A.56) are the complete equations for surface gravity waves written in a compact form.

Analytically, we may also check that our equations reduce to those of *Longuet-Higgins* (2000), for the case where all a_k are real, which corresponds to standing waves. It is a simple matter to show that under the condition that $a_{-k} = a_k$, then the entries of P become

$$P_{mn} \to \frac{1}{2}\frac{1}{\sqrt{|m||n|}}\left(a_{n-m} + a_{m+n} - a_m a_n\right), \tag{A.57}$$

which is precisely the formulation that *Longuet-Higgins* (2000) used. With this identification, the rest of our variables are equivalent to those of *Longuet-Higgins* (2000) and the equivalence is complete.

A.4 Special cases

We consider some simple wave scenarios to both validate our numerical model and provide us with initial conditions that are of interest in later numerical

experiments. Furthermore, these examples give us better familiarity with our model.

A.4.1 Linear waves

In the case of linear waves (i.e. first order in a_n) it is easy to show that the governing equations become a system of decoupled ordinary differential equations of the form

$$\ddot{a}_n + |n| a_n = 0. \tag{A.58}$$

Solutions to these equations correspond to (decoupled) linear waves.

A.4.2 Stokes Waves

A more interesting example comes from the consideration of *Stokes waves*, that is, a permanent progressive solution to the water wave equations. The Fourier coefficients for these waves are well known (see, for instance, *Longuet-Higgins* 1975, 1978a, 1985) and can be accurately derived via the Lagrangian of Balk (see Balk, 1996, §4). Indeed, this gives us a simpler look at some dynamically significant quantities that we focus on in more complicated wave cases. These quantities includes the kinetic and potential energy (and in particular their difference, i.e. the Lagrangian), the phase speed of the wave as well as the wave steepness.

In their canonical presentation, Stokes waves are assumed to be symmetric (*Longuet-Higgins* 1978a, 1985), but as we show below this restriction is not necessary and if it is not taken as an ansatz, then from our model one finds the equations *Zufiria* (1987) used in his study of asymmetric surface gravity waves.

For permanent progressive waves, we boost into a reference frame traveling at a speed c such that in this frame the wave is stationary in the sense that the free surface evolution is time independent. This implies (we return to the Y variables for this calculation since they are easier to compare with the existing literature)

$$\dot{Y}_k = ickY_k. \tag{A.59}$$

Substituting this into the equation for B_n, i.e. equation (A.30), we see that

$$B_n = \frac{i}{n}\left\{-\dot{Y}_n + \sum_{k+j=n} \dot{Y}_k Y_j j(\sigma_k - \sigma_j)\right\} \tag{A.60}$$

$$= cY_n,$$

where the quadratic term has dropped out because for every pair (j,k) yielding a non-zero term, there is an equal and opposite term with index (k,j). Therefore, the kinetic energy can be written as

$$T = c^2 \sum_{n=1}^{N} nY_n Y_{-n} = -c^2 \frac{Y_0}{2} \tag{A.61}$$

and the governing equations take the form

$$\frac{\partial V}{\partial Y_n} = c^2 |n| Y_{-n}, \tag{A.62}$$

for each $n = (\pm 1, \pm 2, ...)$. Carrying out this differentiation, we find that the k-th equation is given by

$$Y_{-k} + |k|Y_{-k}(2Y_0 - c^2) + \sum_{i+j+k=0} (|i| + 1/2|k|)Y_i Y_j = 0, \tag{A.63}$$

together with the equation for the conservation of mass

$$Y_0 + 2\sum_{k=1}^{N} |k| Y_k Y_{-k} = 0. \tag{A.64}$$

As Balk (1996) notes, if we let $Y_0 = (A_0 + c^2)/2$, $Y_k = 1/2A_k$ *and* we restrict our solutions to symmetric waves, i.e. constraining $Y_{-k} = Y_k$, then we arrive at the result of Longuet-Higgins (1978, 1985), namely that these waves are described by the (quadratic) coupled equations

$$A_k + |k|A_k A_0 + \frac{1}{2} \sum_{i+j+k=0} (|i| + 1/2|k|)A_i A_j = 0 \tag{A.65}$$

and

$$A_0 + \sum_{k=1}^{N} |k| A_k A_{-k} = -c^2. \tag{A.66}$$

This is to be juxtaposed against the cubic system of equations one arrives at if they were to attempt to solve for the coefficients using only the condition that the pressure vanishes at the free surface (*Schwartz* 1974, *Longuet-Higgins* 1978b).

Note, this system has $N+1$ equations, with $N+2$ variables. By specifying A_0, the system is completely determined. The wave steepness, ak, is defined as (*Schwartz* 1974)

$$ak = \sum A_{2n+1}, \tag{A.67}$$

while the phase velocity is given by (*Longuet-Higgins* 1985)

$$c^2 = -(A_0 + \sum n A_n^2). \tag{A.68}$$

An example of a permanent progressive symmetric gravity wave will be discussed in section A.6 and shown in Figure A.6. These solutions were also checked against the results of *Schwartz* (1974), *Longuet-Higgins* (1975).

Note, if we do not restrict ourselves to symmetric solutions, and let $Y_k = \alpha_k + i\beta_k$, where (α_k, β_k) are real, then by taking real and imaginary parts of the governing equation we arrive at the result of *Zufiria* (1987) for asymmetric permanent progressive waves.

A.5 The case $N = 1$

It is instructive to consider truncated cases of the governing equations. In particular, we first examine the case where there is one mode in the system. This follows the methodology developed for the standing wave case by *Longuet-Higgins* (2000). Furthermore, it allows us to examine a very simple system of equations that exhibit similar behavior to the much more complicated *physical* system of equations (with N large enough to describe the phenomena in question). This will motivate us to look for permanent progressive solutions to our $N = 1$ example,

which are the analogue of Stokes waves. Examining the behavior of these waves under perturbations forms the motivation for future studies.

To begin, we let $\alpha = a_1$ and $\beta = a_{-1}$, and find

$$4T = \left[\left(1 - \frac{\alpha\beta}{2}\right)\dot{\alpha} - \frac{\alpha^2}{2}\dot{\beta}\right]\left[\left(1 - \frac{\alpha\beta}{2}\right)\dot{\beta} - \frac{\beta^2}{2}\dot{\alpha}\right], \tag{A.69}$$

and

$$4V = \alpha\beta - \frac{(\alpha\beta)^2}{2}. \tag{A.70}$$

The Euler-Lagrange equations for (α, β) then imply

$$L\ddot{\alpha} + M\ddot{\beta} = -\frac{1}{2}\left[L_\alpha\dot{\alpha}^2 + 2L_\beta\dot{\alpha}\dot{\beta} + (2M_\beta - N_\alpha)\dot{\beta}^2\right] + C1 \tag{A.71}$$

$$M\ddot{\alpha} + N\ddot{\beta} = -\frac{1}{2}\left[(2M_\alpha - L_\beta)\dot{\alpha}^2 + 2N_\alpha\dot{\alpha}\dot{\beta} + N_\beta\dot{\beta}^2\right] + C2, \tag{A.72}$$

where

$$L = \frac{1}{4}\alpha\beta^3 - \frac{1}{2}\beta^2, \tag{A.73}$$

$$M = \frac{1}{2} + \frac{1}{4}\alpha^2\beta^2 - \frac{1}{2}\alpha\beta, \tag{A.74}$$

$$N = \frac{1}{4}\alpha^3\beta - \frac{1}{2}\alpha^2, \tag{A.75}$$

and

$$C_1 = \frac{1}{2}\alpha\beta^2 - \frac{1}{2}\beta; \quad C_2 = \frac{1}{2}\alpha^2\beta - \frac{1}{2}\alpha. \tag{A.76}$$

Note, these governing equations can be rewritten as

$$\begin{bmatrix} L & M \\ M & N \end{bmatrix}\begin{bmatrix} \ddot{\alpha} \\ \ddot{\beta} \end{bmatrix} = \begin{bmatrix} F_1 \\ F_2 \end{bmatrix} \tag{A.77}$$

where F_1, F_2 are the right hand sides of equations (A.71) and (A.72), respectively. We define the coefficient matrix as $\mathbb{Q}$, i.e.

$$\mathbb{Q} = \begin{bmatrix} L & M \\ M & N \end{bmatrix}. \tag{A.78}$$

Now, equation (A.77) has solutions provided that $\mathbb{Q}$ is invertible, that is, it is not singular. A matrix is singular when its determinant vanishes, so there is some interest in looking at how the wave evolution breaks down as $det(\mathbb{Q}) \to 0$. To this end, the determinant of $\mathbb{Q}$ is

$$det(\mathbb{Q}) = LN - M^2 = 0 \implies \alpha\beta = 1. \tag{A.79}$$

The reality condition on the Fourier components mandates that $\alpha^* = \beta$, so that letting $\alpha = \mathcal{A} + i\mathcal{B} = \beta^*$, this condition implies that $(\mathcal{A}, \mathcal{B})$ must lie within a circle of radius 1 i.e.

$$\mathcal{A}^2 + \mathcal{B}^2 < 1. \tag{A.80}$$

In the case $\mathcal{B} = 0$, we have the result of the $N = 1$ case for standing waves, as discussed by *Longuet-Higgins* (2000).

A simplified class of solutions to equation (A.77) are those of the permanent progressive type. That is, we choose

$$\alpha = \alpha_0 e^{ict}; \quad \beta = \alpha_0 e^{-ict}, \tag{A.81}$$

where c is a to be determined phase velocity of the waves. When this ansatz is made, we find from equation (A.77) the following relationship between c and α_0:

$$c^2 = 1 - \alpha_0^2. \tag{A.82}$$

Several examples of this class of waves is shown in Figure A.1. For α_0 small we approach the infinitesimal sinusoidal wave solution we expect from linear theory for deep-water surface gravity waves (*Phillips* 1977). As $\alpha_0 \to 1$, the free surface develops a cusp (note this is also when the coefficient matrix $\mathbb{Q}$ becomes singular), taking the form of a cycloid.

The total energy of these waves $T + V$ is conserved, and takes the form

$$T + V = \frac{1}{4}\alpha_0^2 \left(c^2 + \left(1 - \frac{1}{2}\alpha_0^2 \right) \right) = \frac{1}{2}\alpha_0^2 \left(1 - \frac{3}{4}\alpha_0^2 \right). \tag{A.83}$$

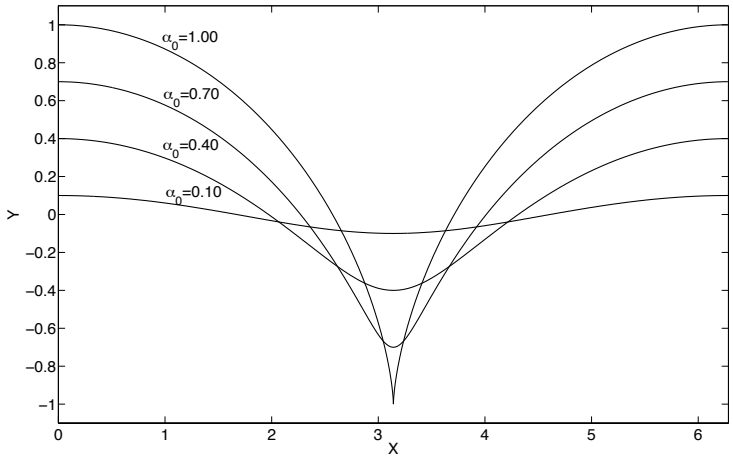

Figure A.1: Permanent progressive wave solutions to the $N = 1$ system of equations, for several values of α_0. The limiting form of the surface profile takes the form of a cycloid, and develops a downward facing cusp, corresponding to the vanishing of the determinant of $\mathbb{Q}$.

This is plotted against α_0 in Figure A.2. We see that, similar to Stokes waves (*Schwartz* 1974, *Longuet-Higgins* 1975), the energy does not monotonically increase with α_0. The energy maximum occurs when $\alpha_0 = \sqrt{2/3}$.

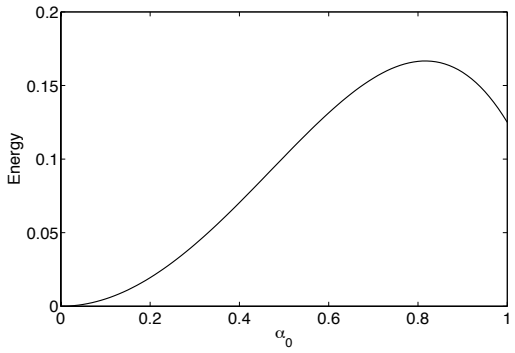

Figure A.2: The total energy $T+V$ as a function of the coefficient α_0. We see that the relationship is not monotonic and the maximum energy occurs at $\alpha_0 = \sqrt{2/3}$.

As a simple example we show in Figure A.3 the propagation of a permanent progressive wave with $\alpha_0 = 0.75$. This also serves as one way to corroborate the numerical scheme and ensure stability of the time stepping algorithm. We see that there is a strong crest-trough asymmetry. Opposite to Stokes waves, these waves

are peakier at their troughs and flatter at their crests. From Figure A.3 we see that this wave travels without change of form, as we expect from our analysis in the previous section. Note, the energy, given by equation (A.83), is conserved to one part in $\mathcal{O}(10^{10})$ when a fourth order Runge-Kutta scheme is used to integrate equations (A.77).

A.5.1 Perturbations to the equilibrium states

We now examine the behavior of these permanent progressive waves to perturbations of the form $\gamma_0 e^{it}$ for γ_0 a constant. These perturbations are *super-harmonic* (*Longuet-Higgins* 1978a) as they (necessarily) have the same horizontal scale as the underlying wave. We would like to know under which conditions perturbations lead to the determinant of $\mathbb{Q}$ going to 0. Note, *Longuet-Higgins* (2000) found that for standing waves one can have $\mathbb{Q}$ invertible, while still obtaining non-physical results, e.g. a free surface with a loop.

We consider three different scenarios, namely $\gamma_0 = (-0.01, 0, 0.01)$. The phase space evolution of these scenarios, in the dependent variables $(Re(\alpha), Im(\alpha))$, is shown in Figure A.4. The grey shaded region represents the values of these variables in which $\mathbb{Q}$ is invertible, and solutions exist. The black line shows the unperturbed wave, with the phase space trajectory of these waves being a circle, as expected. Next, we see that there is a sign dependence on the perturbation, as the behavior of $\gamma_0 = (-0.01, 0.01)$ are very different. This implies that one must employ nonlinear stability analysis to analytically recover this result. We see that for negative perturbations, the trajectory in phase space stays relatively close to the unperturbed wave, remaining well within the domain of solutions for the duration of integration considered here. However, when the perturbation is positive, the trajectory in phase space diverges rapidly from the unperturbed trajectory. In fact, it monotonically approaches the boundary of the domain of solutions and in finite time reaches this boundary, leading to the formation of a cusp. This is shown in Figure A.5. Note, unlike for the limiting Stokes wave, this cusp is downward pointing.

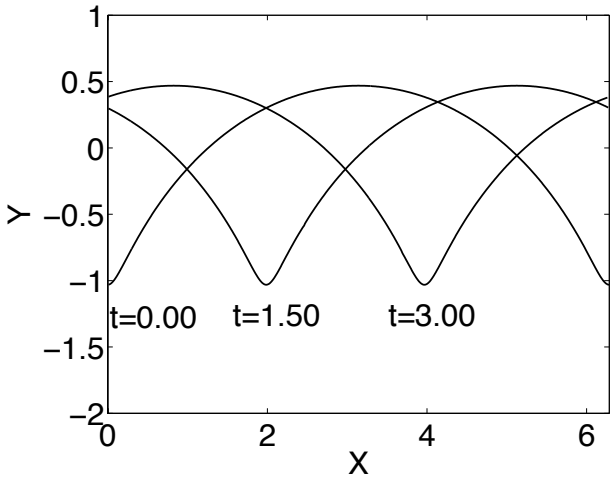

Figure A.3: Evolution of a permanent progressive wave with $\alpha_0 = 0.75$. These waves travel without change of form. Note the region of large curvature in the *trough* of the wave, which is the opposite of steep Stokes waves, which have regions of high curvature at their crests.

A.6 Overturning surface gravity wave

We now turn our attention to modeling overturning, or breaking, surface gravity waves. This involves making N sufficiently large to ensure the phenomena in question is accurately captured. Although this theoretically leads to no additional complication, in practice, it becomes extremely costly to implement this model as N becomes large.

Numerically, we write our scheme in Fortran 77, and employ threaded optimized BLAS (Basic Linear Algebra Subprograms) routines via the MKL (Math Kernel Library) library for the *Intel Fortran* compiler. This has the added advantage that all parallelization is handled internally by the MKL library. Time stepping is achieved by a fourth order Runge-Kutta scheme.

There are no known analytic solutions of the water wave equations to use to test our numerical scheme. However, one classical way to corroborate the validity of water wave models is to integrate the permanent progressive Stokes waves discussed in §A.4 (*Longuet-Higgins and Cokelet* 1976). To this end, we propagate a Stokes wave with $ak = 0.41847$, $c = 1.08907$, and $Q_0 = 0.95$, with $Q_0 = 1$ being the value of the limiting Stokes Wave, where ak is as defined in equation (A.67), c

via equation (A.68) and $Q_0 \equiv 1 + Y_0$ (*Longuet-Higgins* 1985). The quantity Q_0 is used to define these waves instead of ak because relevant physical properties (e.g. phase velocity and energy) increase monotonically as a function of this variable (*Longuet-Higgins* 1985). Note, we generate these initial conditions by following the method outlined in *Longuet-Higgins* (1985, §5). That is, we solve the system of quadratic equations for the Fourier coefficients $\{Y_i\}$ discussed in §A.4.2 using Newton's method until suitable convergence is met. As an initial *guess* we use a linear sinusoidal wave.

An example of the propagation of this Stokes wave is shown in Figure A.6. We see that the wave propagates without change of form. Here, $N = 256$ modes are used. Additionally, we compute the total energy in these waves and find that it is conserved to one part in $\mathcal{O}(10^7)$. These waves have peakier crests and flatter troughs, which should be compared to the $N = 1$ case where the opposite is true.

Next, we consider perturbations to this Stokes wave of the form $\gamma_0 \cos t$, so that $Y = Y_s + \gamma_0 \cos t$ where Y_s is the permanent progressive wave solution discussed in the previous paragraphs. It is well known that Stokes waves are subject to the superharmonic instability (*Longuet-Higgins* 1978a), and that a positive perturbation leads to wave overturning (*Longuet-Higgins* 1997). Figure A.7 shows the free surface just after it has become multi-valued and hence the wave has overturned and is in the process of breaking. Note, for this simulation, we used $N = 2048$ points, while the time step was taken to be $\Delta t = 0.0005$. This simulation was run on 16 processors, and took 24 hours of walltime to complete.

A.7 Future work

In this appendix we have developed the Lagrangian of *Balk* (1996), and put the equations in a form more suitable for numerical implementation. Furthermore, we have examined some of the implications of the water wave equations that are apparent when presented in this form. A simple model with 1 mode is considered and the conditions under which solutions exist are discussed. Next, we integrate a steep Stokes wave to corroborate the model for higher resolution needed to accu-

rately describe surface gravity waves. We then add a superharmonic perturbation, and observe wave overturning.

There are several areas of inquiry that the methodology developed in this appendix opens up. First, the phase space portrait shown for the $N = 1$ model clearly shows the differences in trajectories of the waves based on the sign of the initial perturbation. This has potential application to an analogous scenario of a superharmonic perturbation to a Stokes wave (*Longuet-Higgins* 1997), where this methodology could be used to examine the *predictability* of breaking based on the initial conditions. Therefore, one must develop general criteria for the vanishing of the determinant of the matrix $\mathbb{Q}$, as a way of tracking the tendency towards large curvature generation used as an indication of wave breaking. Work to this end is currently in progress.

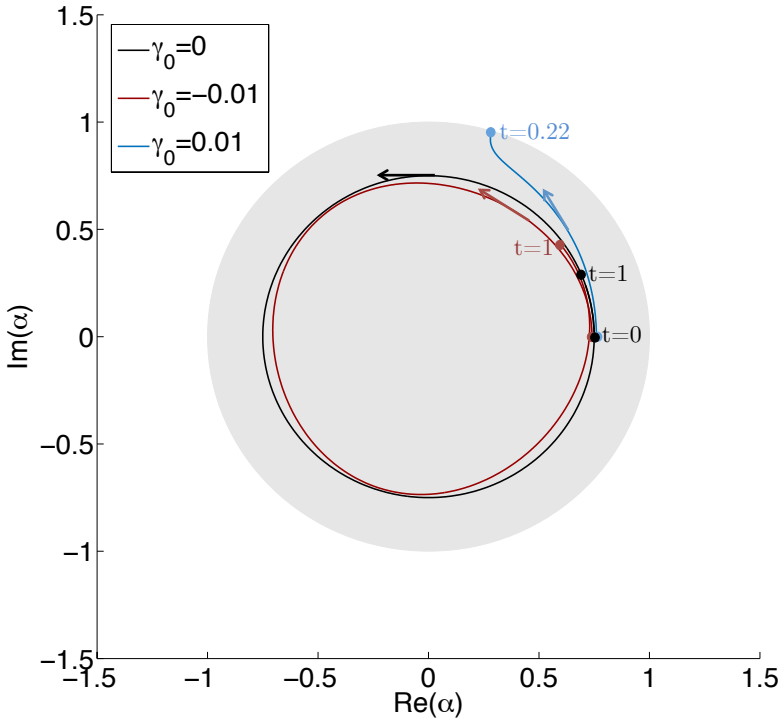

Figure A.4: The phase space evolution of a permanent progressive wave with $\alpha_0 = 0.75$, under three different values of perturbation amplitude γ_0. The grey shaded region represents values of $Re(\alpha)$ and $Im(\alpha)$ such solutions exist, i.e. $\mathbb{Q}$ is invertible. The black line represents the un-perturbed permanent progressive wave. The red line shows the phase space evolution when the wave experiences a negative perturbation ($\gamma_0 < 0$) while the blue line shows the evolution under a positive perturbation ($\gamma_0 > 0$). For the integration times considered here the red line stays confined to the neighborhood of the equilibrium solution, while the blue line rapidly approaches the boundary of solutions, and reaches it at $t = 0.22$, where we see in figure A.5 that a cusp in the free surface is formed. The arrows indicate the direction of positive time evolution.

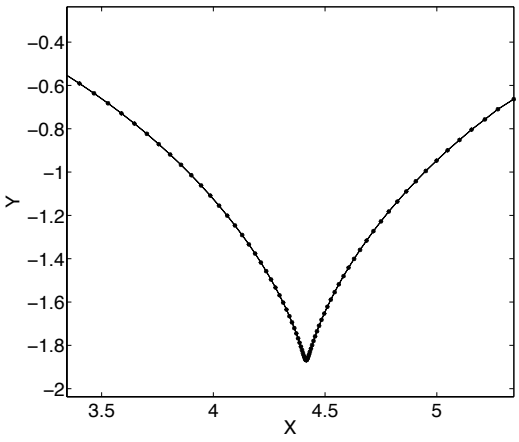

Figure A.5: The formation of a cusp in the free surface for the case where $\gamma_0 = 0.01$. This corresponds to the blue curve in the previous figure, and shows the free surface at the time $t = 0.22$, i.e. when the determinant of $\mathbb{Q}$ vanishes.

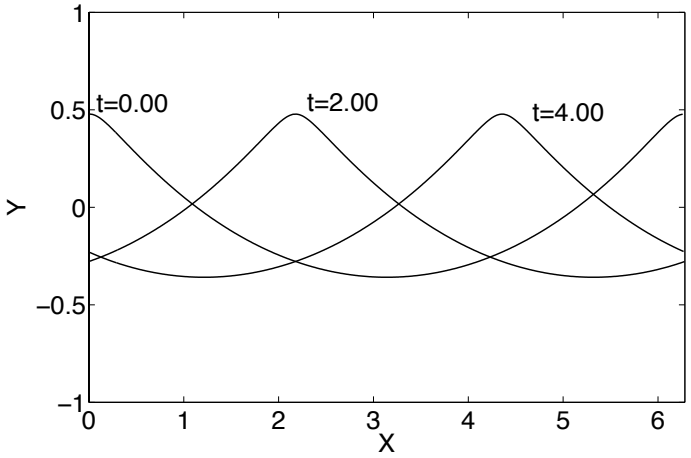

Figure A.6: A permanent progressive (i.e. Stokes) wave, with $Q = 0.95$, $ak = 0.41847$ and $c = 1.08907$, which propagates without change of form. This is one way to corroborate the validity of our model. Note, for this example the number of modes was $N = 256$, the time step is $\Delta t = 0.005$ and it is found that energy is conserved to one part in 10^7.

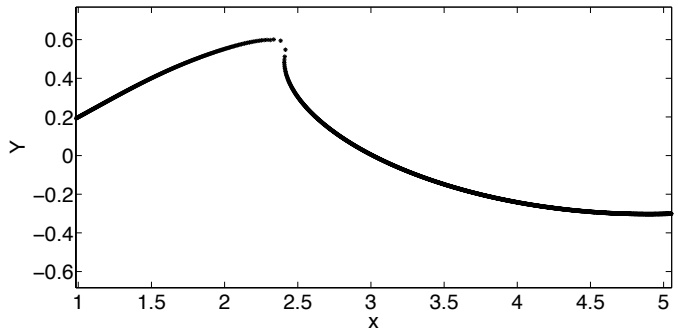

Figure A.7: A breaking wave, due to a superharmonic perturbation to the Stokes wave shown in figure A.6. The asterisks represent surface points. Note, the free surface is multivalued at this time. This simulation is for $N = 2048$ points.

B A Virial theorem for deep-water surface gravity waves

In this appendix we derive a virial theorem for deep-water surface gravity waves, connecting the geometry, kinematics, and dynamics of these waves. Virial theorems have been shown to be insightful in many physical contexts, including astrophysics (*Chandrasekhar and Fermi* 1953, *Ballesteros-Paredes* 2006) and the N-body problem (*Goldstein* 1965). The virial theorem for water waves is also related to a conserved integral originally derived by *Benjamin and Olver* (1982) in their classification of *all* of the conserved integrals of the water wave equations (see also *Longuet-Higgins* 1983).

We begin by defining the moment of inertia I as

$$I = \iint_{\Omega} \rho \mathbf{x} \cdot \mathbf{x} \, dxdy, \tag{B.1}$$

where $\mathbf{x} = (x, y)$, ρ is the density of water (which from now on we take to be 1), and Ω is a domain moving with the fluid. Here x is the horizontal direction while y points vertically upward (see figure 1). This implies

$$\frac{dI}{dt} = 2 \iint_{\Omega} \mathbf{x} \cdot \frac{D\mathbf{x}}{Dt} \, dxdy = 2 \iint_{\Omega} x\phi_x + y\phi_y \, dxdy, \tag{B.2}$$

where commutation of differentiation and integration is admissible because Ω moves with the fluid, and the last equality comes from the relation $D\mathbf{x}/Dt = \boldsymbol{\nabla}\phi$, where ϕ is the velocity potential of the flow. From this we can relate I and a conserved integral of the water wave equations, as originally derived by *Benjamin*

and Olver (1982), which they denote as I_7. In particular,

$$I_7 = \iint_\Omega \boldsymbol{\nabla} \cdot (\phi \mathbf{x})\, dxdy = \oint_{\partial\Omega} \phi(y\, dx - x\, dy), \tag{B.3}$$

where the last equality comes from a Green's integral identity.

In their study, this was the only conserved integral of the water wave equations that the authors were *unable* to put into a physical context. The time evolution of I_7 is given by (*Benjamin and Olver* 1982)

$$\frac{dI_7}{dt} = -\oint_{\partial\Omega} p(y\, dx - x\, dy) + 4T - 3V, \tag{B.4}$$

where T and V are the kinetic and potential energy of the waves, defined as

$$T = \frac{1}{2}\iint_\Omega \left(\phi_x^2 + \phi_y^2\right)\, dxdy; \qquad V = \iint_\Omega gy\, dxdy. \tag{B.5}$$

Therefore, from equation (B.2) we have

$$\frac{1}{2}\frac{dI}{dt} = I_7 - 2\iint_\Omega \phi\, dxdy, \tag{B.6}$$

so that we see that there is a relationship between the quantity I_7 and the evolution of the moment of inertia. Differentiating equation (B.6) with respect to time again, we find

$$\frac{1}{2}\frac{d^2I}{dt^2} = 4T - 3V - 2\iint_\Omega \frac{D\phi}{Dt}\, dxdy. \tag{B.7}$$

The final integral in the above equation can be rewritten as

$$2\iint_\Omega \frac{D\phi}{Dt}\, dxdy = 2\iint_\Omega \left(-(p+gy) + \frac{1}{2}(\phi_x^2 + \phi_y^2)\right)\, dxdy \tag{B.8}$$

$$= -2V + 2T - 2\iint_\Omega p\, dxdy,$$

so that we conclude that the virial theorem for water waves takes the form

$$\frac{1}{2}\frac{d^2I}{dt^2} = 2T - V - 2\mathcal{A} - \oint_{\partial\Omega} p(y\, dx - x\, dy). \tag{B.9}$$

Here we have defined

$$\mathcal{A} = -\iint_{\Omega} p \; dxdy, \tag{B.10}$$

where $\mathcal{A} = \mathcal{A}(t)$ is the *action density*, associated with the Lagrangian for water waves (see Luke 1967, equation (1)).

The term related to the pressure in equation (B.4) is in general nontrivial to evaluate, and has no obvious physical interpretation. This is discussed in detail in *Benjamin and Olver* (1982, § 6.2, 6.3). In the case of the virial theorem, this term can be combined with $\mathcal{A}$ to find

$$-2\mathcal{A} - \oint_{\partial\Omega} p(y \; dx - x \; dy) = \iint_{\Omega} \mathbf{x} \cdot \boldsymbol{\nabla} p \; dxdy, \tag{B.11}$$

Therefore, equation (B.9) can be written as

$$\frac{1}{2}\frac{d^2 I}{dt^2} + \iint_{\Omega} \mathbf{x} \cdot \boldsymbol{\nabla} p \; dxdy = 2T - V. \tag{B.12}$$

Now, we can further elucidate the physics of this equation by rewriting the pressure integral as

$$\iint_{\Omega} \mathbf{x} \cdot \boldsymbol{\nabla} p \; dxdy = -V + \iint_{\Omega} \mathbf{x} \cdot \boldsymbol{\nabla} \hat{p} \; dxdy, \tag{B.13}$$

where $\hat{p}$ denotes the wave induced pressure, i.e. $\hat{p} = gy + p$. This allows us to rewrite equation (B.12) to find

$$\frac{1}{2}\frac{d^2 I}{dt^2} + \iint_{\Omega} \mathbf{x} \cdot \boldsymbol{\nabla} \hat{p} \; dxdy = H + L, \tag{B.14}$$

where the total energy is $H = T + V$, and is conserved, while the Lagrangian is defined as $L = T - V$. For clarity of presentation, we define the integral in the above equation as $\mathcal{B}$, that is,

$$\mathcal{B} = -\iint_{\Omega} \mathbf{x} \cdot \boldsymbol{\nabla} \hat{p} \; dxdy. \tag{B.15}$$

Now, this term $\mathcal{B}$ has a straightforward physical interpretation. In particular, the integrand is (minus) the amount of work required to move a point from the origin to a position $\mathbf{x}$ in the presence of the force due to the pressure induced by the *wave*

motion, $-\boldsymbol{\nabla}\hat{p}$.

We then write the virial theorem as

$$\frac{1}{2}\frac{d^2 I}{dt^2} = \mathcal{B} + H + L, \tag{B.16}$$

The left hand side of equation (B.16) is dependent on the geometry of the fluid at a given instant in time. As is discussed above, $\mathcal{B}$ is related to the work required to displace the fluid particles due to the wave motion. Recall, H is a constant of motion and L reflects the partitioning of energy, between the kinetic and potential energy.

B.1 Second order Stokes waves

To gain intuition about equation (B.16), and to corroborate this relationship for a simple example, we consider second order Stokes waves. Recall, our virial theorem is Lagrangian in nature so that we need the Lagrangian description describing these waves. Labeling the particles as (α, β), we find (see, for instance, *Longuet-Higgins* 1980, *Clamond* 2007)

$$x = \alpha - a\sin(k\alpha - \omega t)e^{k\beta} + \frac{a^2}{2}ke^{2k\beta}\omega t, \tag{B.17}$$

$$y = \frac{1}{2}a^2 k + \beta + a\cos(k\alpha - \omega t)e^{k\beta},$$

where a is the wave amplitude, k is the wavenumber, and ω the angular frequency, with the two connected via the dispersion relationship for linear deep-water waves, i.e. $\omega^2 = gk$. These equations are valid to $\mathcal{O}((ak)^2)$, and we note that the last term in the expansion of x is due to the Stokes drift. A sketch of the problem set up is shown in Figure B.1.

The Jacobian of the transformation from the (x, y) plane to the particle labels (α, β) is given by

$$\frac{\partial(x, y)}{\partial(\alpha, \beta)} = 1 + \mathcal{O}((ak)^2). \tag{B.18}$$

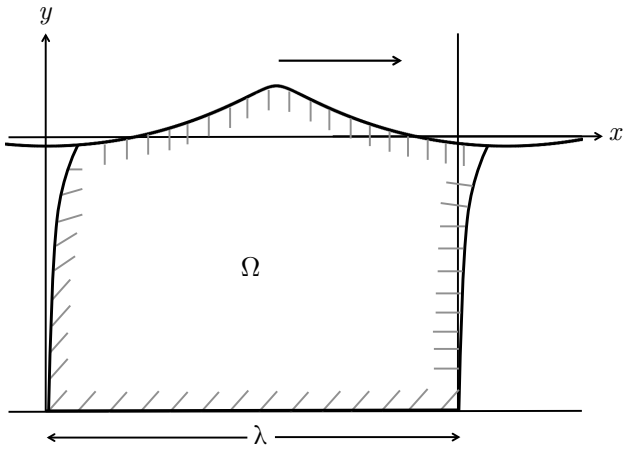

Figure B.1: A sketch of Ω, used in computing the virial theorem for second order Stokes waves in deep-water. This domain moves with the fluid, and is bounded above by the free surface displacement η while the horizontal width of the domain is λ, the wavelength of the Stokes wave. The arrow shows the direction of wave propagation, which is from the left to the right.

The particle velocities associated with these expansions are

$$u = a\omega \cos(k\alpha - \omega t)e^{k\beta} + \frac{a^2}{2}k\omega e^{2k\beta}, \tag{B.19}$$

$$v = a\omega \sin(k\alpha - \omega t)e^{k\beta}.$$

The domain of integration will, to this order, be given by $\alpha \in (0, \lambda)$ and $\beta \in (-\infty, 0)$, where $\lambda = 2\pi/k$. We begin by computing the moment of inertia and find

$$I = \iint_{\Omega} x^2 + y^2 \; dxdy = \int_0^{\lambda} \int_{-\infty}^{0} x(\alpha, \beta)^2 + y(\alpha, \beta)^2 \; d\alpha d\beta. \tag{B.20}$$

Substituting in the expansions given in equation (B.17) we find

$$I = (ak)^2 \left(\frac{\lambda^3}{6k} + \frac{3\lambda}{4k^3} \right) + \frac{2ak}{k^3}\lambda \cos \omega t - \frac{\lambda^2}{2k^2}(ak)^2 \omega t + C + \mathcal{O}((ak)^3), \tag{B.21}$$

where C is the moment of inertia of the fluid when no waves are present, and

does not contribute to the dynamical evolution of I. The time dependent terms in I represent the simple harmonic motion of the particles, and the Stokes drift, respectively.

Now, the expansion given in equation (B.21) implies

$$\frac{1}{2}\frac{d^2 I}{dt^2} = -\frac{ag\lambda}{k}\cos\omega t. \tag{B.22}$$

Next, we calculate $\mathcal{B}$ and find

$$\mathcal{B} = -\iint_{\Omega} \mathbf{x}\cdot\boldsymbol{\nabla}\hat{p}\; dxdy = \int_0^{\lambda}\int_{-\infty}^{0} \mathbf{x}\cdot\frac{d\mathbf{u}}{dt}\; d\alpha d\beta, \tag{B.23}$$

where we have used the fact that $d\mathbf{u}/dt = -\boldsymbol{\nabla}\hat{p}$ in a Lagrangian reference frame, with $\mathbf{u} = (u, v)$. Substituting in the expansions for $\mathbf{x}, \mathbf{u}$, we have

$$\mathcal{B} = -\frac{a^2}{2}g\lambda - \frac{ag\lambda}{k}\cos\omega t. \tag{B.24}$$

Therefore, the two terms on the left hand side of the virial theorem, i.e. equation (B.14), sum to

$$\frac{1}{2}\frac{d^2 I}{dt^2} - \mathcal{B} = \frac{ga^2}{2} = H + L. \tag{B.25}$$

This confirms the well known result that for these waves, $L = 0 \implies T = V$ (i.e. the waves are in energy equipartition), and $H = 1/2ga^2$ (*Phillips* 1977).

C Variational form of the variance identity and the Benjamin-Feir Instability

C.1 Introduction

This appendix provides an alternative method of obtaining the stability criteria of finite amplitude permanent progressive waves, i.e. Stokes waves, to subharmonic perturbations as originally obtained by *Benjamin and Feir* (1967, see also *Zakharov* 1968). This method is based on the variance identity for the nonlinear Schrodinger equation (*Sulem and Sulem* 1999), and extends the classical case for compact wave groups to include the effects of a non-vanishing envelope of a quasi-periodic wave train. By following classical work in astrophysics (*Chandrasekhar and Fermi* 1953), we use the variational form of the variance identity to derive stability criteria for second order Stokes waves, reproducing the results of *Benjamin and Feir* (1967).

The seminal work of *Benjamin and Feir* (1967, see also *Lighthill* 1965, *Zakharov* 1968) elucidated the weak linear instability of finite amplitude deep-water surface gravity waves to subharmonic perturbations. This culminated over one hundred years of work on permanent progressive waves, also known as Stokes waves. These permanent progressive waves have been a source of interest since the original work by *Stokes* (1847), including the important proof of the convergence of the sums defining these waves by *Levi-Civita* (1925). The Benjamin-Feir in-

stability shapes the way we think about surface gravity waves in both theoretical (*Sulem and Sulem* 1999, *Zakharov and Ostrovsky* 2009) and oceanographic contexts (*Zakharov et al.* 1992, *Janssen* 2003). Therefore, it is worth reporting an alternative derivation of this important result.

Moment equations, governing the evolution of the centroid and the variance of the linear energy density, have proven to be useful in understanding geometric, kinematic, and dynamic properties of waves governed by the nonlinear Schrodinger equation. The variance identity in particular has been used to look at the stability of soliton solutions to perturbations (*Rasmussen and Rypdal* 1986, *Sulem and Sulem* 1999). These equations are nearly always restricted to compact wave groups, which vanish at the endpoints of the domain. In this note, we extend the variance identity to include these effects, allowing us to apply this methodology to periodic wave trains.

The outline of this appendix is as follows. In section C.2 we derive the variance identity for the nonlinear Schrodinger equation under the assumption that the modulus of the complex valued amplitude does *not* vanish over the domain of interest. In section C.3 we use the variational method to look at the evolution of the variance under the influence of a subharmonic perturbation, from which we reproduce the stability criteria of *Benjamin and Feir* (1967).

C.2 Variance identity of periodic waves governed by the nonlinear Schrodinger equation

The nonlinear Schrodinger equation,

$$A_t + iA_{xx} + i|A|^2A = 0, \tag{C.1}$$

governs weakly nonlinear narrow-banded deep-water surface gravity waves. Here, we are are in a reference frame moving at the linear group velocity $c_g = \omega_0/2k_0$ and we have normalized the space and time variables for clarity of presentation. That is, if (x', t') represent space and time in the laboratory reference frame, we

have

$$x = 2\epsilon k_0 x'; \qquad t = \epsilon^2 \omega_o (t' - x'/c_g). \tag{C.2}$$

In equation (C.1), A is a complex valued function related to the coefficient of the first mode of the free surface displacement $\eta(x,t)$ and $\epsilon = ak$ is the small parameter, given by the slope of the waves. This equation arises in a variety of physical models, and has been the source of considerable interest across many disciplines.

To derive our variance identity, we need to recall two conservation laws of equation (C.1). First, the conservation law associated with the phase shift invariance is (see, e.g. *Sulem and Sulem* 1999)

$$\frac{\partial |A|^2}{\partial t} + \frac{\partial P}{\partial x} = 0, \tag{C.3}$$

where

$$P = i\left(AA_x^* - A^* A_x\right). \tag{C.4}$$

The conservation law for invariance to spatial shifts yields

$$\frac{\partial P}{\partial t} + \frac{\partial D}{\partial x} = 0, \tag{C.5}$$

where

$$D = \left(2|A_x|^2 - (A^* A_{xx} + AA_{xx}^*) - |A|^4\right). \tag{C.6}$$

Next, we define the variance of the wave packet as

$$I = \int_0^\Lambda x^2 |A|^2 \, dx, \tag{C.7}$$

where Λ is a (normalized) wavenumber, to be defined precisely below. First, we have

$$\frac{dI}{dt} = \int_0^\Lambda x^2 |A|_t^2 \, dx = 2\int_0^\Lambda xP \, dx - \Lambda^2 \, P|_{x=\Lambda} \tag{C.8}$$

Differentiating this equation again, and dividing C.8 by 8, we have

$$\frac{1}{8}\frac{d^2 I}{dt^2} = H + \frac{1}{4}\int_0^{\Lambda} |A|^4 \, dx - \frac{1}{4}\Lambda \, D|_{x=\Lambda} + \frac{1}{8}\Lambda^2 \left.\frac{\partial D}{\partial x}\right|_{x=\Lambda}, \tag{C.9}$$

where

$$H = \int_0^{\Lambda} |A_x|^2 - \frac{1}{2}|A|^4 \, dx. \tag{C.10}$$

Note, in the limit of compact wave groups, we can take $\Lambda \to \infty$ and the terms evaluated at $x = \Lambda$ will go to zero, so that we return to the classical result (*Sulem and Sulem* 1999).

C.3 The variational method and the Benjamin-Feir instability

The envelope of unperturbed second order Stokes waves are stationary in this reference frame, and serve as states of dynamical equilibrium (*Benjamin and Feir* 1967). We takes these waves as our basic state, and then consider variations from this equilibrium, due to a subharmonic perturbation.

That is, as initial conditions we take

$$A_o = A + \delta A = \epsilon e^{-i\epsilon^2 t} + \epsilon e^{-i\epsilon^2 t}\left(\gamma^+ e^{i\theta^+} + \gamma^- e^{i\theta^-}\right), \tag{C.11}$$

where the slowly varying phase of the perturbed waves are given by $\theta^{\pm} = \pm(\epsilon K x - \epsilon\Omega t)$ and the perturbation amplitudes are given by the constants $\gamma^{\pm}$. Here, we associate the integration limit Λ with K, that is $\Lambda = 2\pi/K$.

Note, A_o is the basic state (second order Stokes waves) in dynamical equilibrium, and δA is the subharmonic perturbation to this state. The variational method (*Ledoux* 1945, *Chandrasekhar and Fermi* 1953) provides *a* way of determining the linear stability of this system.

We start by taking variations to the left hand side of equation (C.9) to find

$$\delta I = \int_0^{\Lambda} \delta A A^* + A\delta A^* \, dx. \tag{C.12}$$

Similarly,

$$\delta H = \delta \int_0^\Lambda |A_x|^2 - \frac{1}{2}|A|^4 dx \tag{C.13}$$

$$= \int_0^\Lambda (A_x \delta A_x^* + \delta A_x A_x^*) - \frac{1}{2}|A|^2 (A\delta A^* + \delta A A^*)\ dx,$$

while

$$\delta \int_0^\Lambda |A|^4 dx = 2 \int_0^\Lambda |A|^2 (A\delta A^* + \delta A A^*)\ dx. \tag{C.14}$$

The variation of D is given by

$$\delta D = 2(\delta A_x A_x^* + A_x \delta A_x^*) - (\delta A^* A_{xx} + A^* \delta A_{xx} + \delta A A_{xx}^* + A \delta A_{xx}^*) \tag{C.15}$$

$$-2|A|^2 (A\delta A^* + \delta A A^*)$$

The variational form of our variance identity takes the form

$$\frac{1}{8}\frac{d^2}{dt^2}\delta I = \delta H + \frac{1}{2}\int_0^\Lambda |A|^2 (A\delta A^* + \delta A A^*) dx \tag{C.16}$$

$$-\frac{\Lambda}{4}\delta\ D|_{x=\Lambda} + \frac{\Lambda^2}{8}\frac{\partial}{\partial x}\delta\ D|_{x=\Lambda}$$

We now substitute in the initial condition given in equation (C.11), and keep terms to $\mathcal{O}(\epsilon^4, \gamma^\pm)$. First, we note that $\partial D/\partial x$ does not contribute, as it is $\mathcal{O}(\epsilon^5)$. Next, the integrals on the right hand side of (C.16) all vanish, as they are periodic functions integrated over one period. Hence, the variational form of the variance identity reduces to

$$\Omega^2 = \frac{2\Lambda}{\delta I_o}(K^2 - 2\epsilon^2), \tag{C.17}$$

where δI_o is a constant. Therefore, the instability criteria (Ω imaginary) is met when

$$K^2 < 2\epsilon^2. \tag{C.18}$$

This is exactly the criterion found by *Benjamin and Feir* (1967) in this mapped reference frame.

References

Ablowitz, M. J., and H. Segur (1979), On the evolution of packets of water waves, *Journal of Fluid Mechanics*, *92*(04), 691–715.

Agrawal, G. P. (2007), *Nonlinear Fiber Optics*, Academic press.

Andrews, D. G., and M. McIntyre (1978), An exact theory of nonlinear waves on a lagrangian-mean flow, *Journal of Fluid Mechanics*, *89*(04), 609–646.

Baker, G. R., and C. Xie (2011), Singularities in the complex physical plane for deep water waves, *Journal of Fluid Mechanics*, *685*, 83–116.

Balk, A. (1996), A lagrangian for water waves, *Physics of Fluids*, *8*(2), 416–420.

Ballesteros-Paredes, J. (2006), Six myths on the virial theorem for interstellar clouds, *Monthly Notices of the Royal Astronomical Society*, *372*(1), 443–449.

Banner, M., and W. L. Peirson (2007), Wave breaking onset and strength for two-dimensional deep-water wave groups, *Journal of Fluid Mechanics*, *585*(1), 93–115.

Banner, M., and D. Peregrine (1993), Wave breaking in deep water, *Annual Review of Fluid Mechanics*, *25*(1), 373–397.

Banner, M. L., and J.-B. Song (2002), On determining the onset and strength of breaking for deep water waves. Part ii: Influence of wind forcing and surface shear, *Journal of physical oceanography*, *32*(9), 2559–2570.

Banner, M. L., and X. Tian (1998), On the determination of the onset of breaking for modulating surface gravity water waves, *Journal of Fluid Mechanics*, *367*, 107–137.

Batchelor, G. K. (1967), *An Introduction to Fluid Dynamics*, Cambridge University Press.

Benjamin, T. B., and J. Feir (1967), The disintegration of wave trains on deep water part 1. theory, *Journal of Fluid Mechanics*, *27*(03), 417–430.

Benjamin, T. B., and P. J. Olver (1982), Hamiltonian structure, symmetries and conservation laws for water waves, *Journal of Fluid Mechanics*, *125*, 137–185.

Bretherton, F. P., and C. J. Garrett (1968), Wavetrains in inhomogeneous moving media, *Proceedings of the Royal Society of London. Series A. Mathematical and Physical Sciences*, *302*(1471), 529–554.

Bridges, T. J. (1992), Spatial hamiltonian structure, energy flux and the water-wave problem, *Proceedings of the Royal Society of London A: Mathematical, Physical and Engineering Sciences*, *439*(1906), 297–315.

Bühler, O. (2007), Impulsive fluid forcing and water strider locomotion, *Journal of Fluid Mechanics*, *573*, 211–236.

Bühler, O. (2014), *Waves and Mean Flows*, Cambridge University Press.

Cavaleri, L., B. Fox-Kemper, and M. Hemer (2012), Wind waves in the coupled climate system, *Bulletin of the American Meteorological Society*, *93*(11), 1651–1661.

Chandrasekhar, S., and E. Fermi (1953), Problems of gravitational stability in the presence of a magnetic field, *Astrophysical Journal*, pp. 116–141.

Chereskin, T., and E. Mollo-Christensen (1985), Modulational development of non-linear gravity-wave groups, *Journal of Fluid Mechanics*, *151*, 337–365.

Chu, V. H., and C. C. Mei (1970), On slowly-varying stokes waves, *Journal of Fluid Mechanics*, *41*(04), 873–887.

Clamond, D. (2007), On the lagrangian description of steady surface gravity waves, *Journal of Fluid Mechanics*, *589*, 433–454.

Clamond, D., M. Francius, J. Grue, and C. Kharif (2006), Long time interaction of envelope solitons and freak wave formations, *European Journal of Mechanics-B/Fluids*, *25*(5), 536–553.

Constantin, A., and J. Escher (1998), Wave breaking for nonlinear nonlocal shallow water equations, *Acta Mathematica*, *181*(2), 229–243.

Cooker, M. J., and D. Peregrine (1992), Wave impact pressure and its effect upon bodies lying on the sea bed, *Coastal Engineering*, *18*(3), 205–229.

Craik, A. D., and S. Leibovich (1976), A rational model for langmuir circulations, *Journal of Fluid Mechanics*, *73*(03), 401–426.

Csanady, G. (1994), Vortex pair model of langmuir circulation, *Journal of marine research*, *52*(4), 559–581.

da Silva, A. T., and D. Peregrine (1990), Nonlinear perturbations on a free surface induced by a submerged body: a boundary integral approach, *Engineering Analysis with Boundary Elements*, *7*(4), 214–222.

Deike, L., and W. Melville (2015), Air entrainment and bubble statistics in three-dimensional breaking waves, *Journal of Fluid Mechanics*, *Submitted*.

Deike, L., D. Fuster, M. Berhanu, and E. Falcon (2014), Direct numerical simulations of capillary wave turbulence, *Phys. Rev. Lett.*, *112*, 234,501.

Deike, L., S. Popinet, and W. Melville (2015), Capillary effects on wave breaking, *Journal of Fluid Mechanics*, *769*, 541–569.

Dhanak, M., and B. Bernardinis (1981), The evolution of an elliptic vortex ring, *Journal of Fluid Mechanics*, *109*, 189–216.

Dold, J. (1992), An efficient surface-integral algorithm applied to unsteady gravity waves, *Journal of Computational Physics*, *103*(1), 90–115.

Dold, J., and D. Peregrine (1986), Water-wave modulation, *Coastal Engineering Proceedings*, *1*(20).

Dommermuth, D. G., and D. K. Yue (1987), A high-order spectral method for the study of nonlinear gravity waves, *Journal of Fluid Mechanics*, *184*, 267–288.

Dommermuth, D. G., D. K. Yue, W. Lin, R. Rapp, E. Chan, and W. Melville (1988), Deep-water plunging breakers: a comparison between potential theory and experiments, *Journal of Fluid Mechanics*, *189*, 423–442.

Donelan, M. (1998), Air-water exchange processes, *Coastal and Estuarine Studies*, pp. 19–36.

Drazen, D. A., and W. K. Melville (2009), Turbulence and mixing in unsteady breaking surface waves, *Journal of Fluid Mechanics*, *628*, 85–119.

Drazen, D. A., W. K. Melville, and L. Lenain (2008), Inertial scaling of dissipation in unsteady breaking waves, *Journal of Fluid Mechanics*, *611*, 307–332.

Duncan, J. (1981), An experimental investigation of breaking waves produced by a towed hydrofoil, *Proceedings of the Royal Society of London. A. Mathematical and Physical Sciences*, *377*(1770), 331–348.

Duncan, J. H. (2001), Spilling breakers, *Annu. Rev. Fluid. Mech.*, *33*, 519–547.

Dyachenko, A. I., E. A. Kuznetsov, M. Spector, and V. E. Zakharov (1996), Analytical description of the free surface dynamics of an ideal fluid (canonical formalism and conformal mapping), *Physics Letters A*, *221*(1), 73–79.

Dysthe, K. B. (1979), Note on a modification to the nonlinear schrodinger equation for application to deep water waves, *Proceedings of the Royal Society of London. A. Mathematical and Physical Sciences*, *369*(1736), 105–114.

Dysthe, K. B., K. Trulsen, H. E. Krogstad, and H. Socquet-Juglard (2003), Evolution of a narrow-band spectrum of random surface gravity waves, *Journal of Fluid Mechanics*, *478*, 1–10.

Fedorov, A. V., and W. K. Melville (1998), Nonlinear gravity–capillary waves with forcing and dissipation, *Journal of Fluid Mechanics*, *354*, 1–42.

Fornberg, B. (1980), A numerical method for conformal mappings, *SIAM Journal on Scientific and Statistical Computing*, *1*(3), 386–400.

Fornberg, B., and G. Whitham (1978), A numerical and theoretical study of certain nonlinear wave phenomena, *Philosophical Transactions of the Royal Society of London. Series A, Mathematical and Physical Sciences*, *289*(1361), 373–404.

Fuster, D., G. Agbaglah, C. Josserand, S. Popinet, and S. Zaleski (2009), Numerical simulation of droplets, bubbles and waves: state of the art, *Fluid Dyn Res*, *41*, 065,001.

Fuster, D., J.-P. Matas, S. Marty, S. Popinet, J. Hoepffner, A. Cartellier, and S. Zaleski (2013), Instability regimes in the primary breakup region of planar coflowing sheets., *Journal of Fluid Mechanics*, *736*, 150–176.

Goldman, M. V., and D. R. Nicholson (1978), Virial theory of direct langmuir collapse, *Physical Review Letters*, *41*(6), 406.

Goldstein, H. (1965), *Classical Mechanics*, Addison-Wesley.

Gramstad, O., and K. Trulsen (2011), Hamiltonian form of the modified nonlinear schrödinger equation for gravity waves on arbitrary depth, *Journal of Fluid Mechanics*, *670*, 404–426.

Grare, L., W. L. Peirson, H. Branger, J. W. Walker, J.-P. Giovanangeli, and V. Makin (2013), Growth and dissipation of wind-forced, deep-water waves, *Journal of Fluid Mechanics*, *722*, 5–50.

Hasselmann, K. (1974), On the spectral dissipation of ocean waves due to white capping, *Boundary-Layer Meteorology*, *6*(1-2), 107–127.

Helmholtz, H. (1858), About integrals of hydrodynamic equations related with vortical motions, *J. für die reine Angewandte Mathematik*, *55*, 25.

Hornung, H. G., C. Willert, and S. Turner (1995), The flow field downstream of a hydraulic jump, *Journal of Fluid Mechanics*, *287*, 299–316.

Iafrati, A. (2011), Energy dissipation mechanisms in wave breaking processes: Spilling and highly aerated plunging breaking events, *Journal of Geophysical Research: Oceans*, *116*(C7).

Janssen, P. A. (1983), On a fourth-order envelope equation for deep-water waves, *Journal of Fluid Mechanics*, *126*, 1–11.

Janssen, P. A. (2003), Nonlinear four-wave interactions and freak waves, *Journal of Physical Oceanography*, *33*(4), 863–884.

Kit, E., and L. Shemer (2002), Spatial versions of the zakharov and dysthe evolution equations for deep-water gravity waves, *Journal of Fluid Mechanics*, *450*, 201–205.

Kundu, P., I. Cohen, and D. Dowling (2012), *Fluid Mechanics*, Academic Press, Waltham, MA.

Lamarre, E., and W. Melville (1991), Air entrainment and dissipation in breaking waves, *Nature*, *351*, 469–472.

Lamb, H. (1932), *Hydrodynamics*, Cambridge University Press.

Ledoux, P. (1945), On the radial pulsation of gaseous stars., *The Astrophysical Journal*, *102*, 143.

Leibovich, S. (1983), The form and dynamics of Langmuir circulations, *Annual Review of Fluid Mechanics*, *15*(1), 391–427.

Levi-Civita, T. (1925), Determination rigoureuse des ondes permanentes d'ampleur finie, *Mathematische Annalen*, *93*(1), 264–314.

Lighthill, J. (1978), *Waves in fluids*, Cambridge university press.

Lighthill, M. (1965), Contributions to the theory of waves in non-linear dispersive systems, *IMA Journal of Applied Mathematics*, *1*(3), 269–306.

Linden, P., and J. Turner (2001), The formation of 'optimal' vortex rings, and the efficiency of propulsion devices, *Journal of Fluid Mechanics*, *427*, 61–72.

Lo, E., and C. C. Mei (1985), A numerical study of water-wave modulation based on a higher-order nonlinear schrödinger equation, *Journal of Fluid Mechanics*, *150*, 395–416.

Lo, E. Y. (1985), *Long-Time Evolution of Surface Waves in Coastal Waters*, 303, Dept. of Civil Engineering, Massachusetts Institute of Technology.

Longuet-Higgins, M. S. (1957), The statistical analysis of a random, moving surface, *Philosophical Transactions of the Royal Society of London A: Mathematical, Physical and Engineering Sciences*, *249*(966), 321–387.

Longuet-Higgins, M. S. (1974), Breaking waves in deep or shallow water, *Proc. 10th Conf. on Naval Hydrodynamics*, *597*.

Longuet-Higgins, M. S. (1975), Integral properties of periodic gravity waves of finite amplitude, *Proceedings of the Royal Society of London A: Mathematical, Physical and Engineering Sciences*, *342*, 157–174.

Longuet-Higgins, M. S. (1978a), The instabilities of gravity waves of finite amplitude in deep water. I. Superharmonics, *Proceedings of the Royal Society of London. A. Mathematical and Physical Sciences*, *360*(1703), 471–488.

Longuet-Higgins, M. S. (1978b), Some new relations between stokes's coefficients in the theory of gravity waves, *IMA Journal of Applied Mathematics*, *22*(3), 261–273.

Longuet-Higgins, M. S. (1980), Spin and angular momentum in gravity waves, *Journal of Fluid Mechanics*, *97*(01), 1–25.

Longuet-Higgins, M. S. (1983), On integrals and invariants for inviscid, irrotational flow under gravity, *Journal of Fluid Mechanics*, *134*, 155–159.

Longuet-Higgins, M. S. (1985), Bifurcation in gravity waves, *Journal of Fluid Mechanics*, *151*, 457–475.

Longuet-Higgins, M. S. (1997), Progress towards understanding how waves break, *Twenty-First Symposium on Naval Hydrodynamics*, pp. 7–28.

Longuet-Higgins, M. S. (2000), Theory of water waves derived from a lagrangian. part 1. standing waves, *Journal of Fluid Mechanics*, *423*, 275–291.

Longuet-Higgins, M. S. (2001), Vertical jets from standing waves, *Proceedings of the Royal Society of London A: Mathematical, Physical and Engineering Sciences*, *457*(2006), 495–510.

Longuet-Higgins, M. S., and E. Cokelet (1976), The deformation of steep surface waves on water. i. a numerical method of computation, *Proceedings of the Royal Society of London A: Mathematical, Physical and Engineering Sciences*, *350*(1660), 1–26.

Longuet-Higgins, M. S., and R. Stewart (1962), Radiation stress and mass transport in gravity waves, with application to surf beats, *Journal of Fluid Mechanics*, *13*(04), 481–504.

Longuet-Higgins, M. S., and R. Stewart (1964), Radiation stresses in water waves; a physical discussion, with applications, *Deep Sea Research and Oceanographic Abstracts*, *11*(4), 529–562.

Longuet-Higgins, M. S., and J. Turner (1974), An entraining plume model of a spilling breaker, *Journal of Fluid Mechanics*, *63*(01), 1–20.

Luke, J. (1967), A variational principle for a fluid with a free surface, *Journal of Fluid Mechanics*, *27*(02), 395–397.

McIntyre, M. (1981), On the wave momentummyth, *Journal of Fluid Mechanics*, *106*, 331–347.

McLean, J., Y. Ma, D. Martin, P. Saffman, and H. Yuen (1981), Three-dimensional instability of finite-amplitude water waves, *Physical Review Letters*, *46*(13), 817.

Meiron, D. I., S. A. Orszag, and M. Israeli (1981), Applications of numerical conformal mapping, *Journal of Computational Physics*, *40*(2), 345–360.

Melville, W. (1983), Wave modulation and breakdown, *Journal of Fluid Mechanics*, *128*, 489–506.

Melville, W. (1994), Energy dissipation by breaking waves, *Journal of Physical Oceanography*, *24*(10), 2041–2049.

Melville, W. K. (1982), The instability and breaking of deep-water waves, *Journal of Fluid Mechanics*, *115*, 165–185.

Melville, W. K. (1996), The role of surface wave breaking in air-sea interaction, *Annual Review of Fluid Mechanics*, *28*, 279–321.

Melville, W. K., and D. J. Rapp (1985), Momentum flux in breaking waves, *Nature*, *317*.

Melville, W. K., F. Veron, and C. J. White (2002), The velocity field under breaking waves: coherent structure and turbulence, *J. Fluid. Mech.*, *454*.

Meza, E., J. Zhang, and R. J. Seymour (2000), Free-wave energy dissipation in experimental breaking waves, *Journal of Physical Oceanography*, *30*(9), 2404–2418.

Miles, J. W. (1977), On hamilton's principle for surface waves, *Journal of Fluid Mechanics*, *83*(01), 153–158.

Nye, J., and M. Berry (1974), Dislocations in wave trains, *Proceedings of the Royal Society of London A: Mathematical, Physical and Engineering Sciences*, *336*(1605), 165–190.

Peregrine, D. (1998), Surf zone currents, *Theoretical and computational fluid dynamics*, *10*(1-4), 295–309.

Peregrine, D. (1999), Large-scale vorticity generation by breakers in shallow and deep water, *European Journal of Mechanics-B/Fluids*, *18*(3), 403–408.

Peregrine, D., and G. Thomas (1979), Finite-amplitude deep-water waves on currents, *Philosophical Transactions of the Royal Society of London. Series A, Mathematical and Physical Sciences*, *292*(1392), 371–390.

Perić, R., N. Hoffmann, and A. Chabchoub (2015), Initial wave breaking dynamics of peregrine-type rogue waves: A numerical and experimental study, *European Journal of Mechanics-B/Fluids*, *49*, 71–76.

Perlin, M., W. Choi, and Z. Tian (2013), Breaking waves in deep and intermediate waters, *Annual Review of Fluid Mechanics*, *45*, 115–145.

Phillips, O. (1977), *The Dynamics of the Upper Ocean*, Cambridge University Press.

Phillips, O. M. (1985), Spectral and statistical properties of the equilibrium range in wind-generated gravity waves, *Journal of Fluid Mechanics*, *156*, 505–531.

Pizzo, N., and W. K. Melville (2013), Vortex generation by deep-water breaking waves, *Journal of Fluid Mechanics*, *734*, 198–218.

Pope, S. B. (2000), *Turbulent Flows*, Cambridge university press.

Popinet, S. (2003), Gerris: a tree-based adaptative solver for the incompressible euler equations in complex geometries, *Journal of Computational Physics*, *190*, 572–600.

Popinet, S. (2009), An accurate adaptative solver for surface-tension-driven interfacial flows, *Journal of Computational Physics*, *228*, 5838–5866.

Rapp, R., and W. Melville (1990), Laboratory measurements of deep-water breaking waves, *Philosophical Transactions of the Royal Society of London. Series A, Mathematical and Physical Sciences*, pp. 735–800.

Rapp, R. J. (1986), Laboratory measurements of deep water breaking waves, Ph.D. thesis, Massachusetts Institute of Technology.

Rasmussen, J. J., and K. Rypdal (1986), Blow-up in nonlinear schrödinger equations-i a general review, *Physica Scripta*, *33*(6), 481.

Restrepo, J. M., J. M. Ramírez, J. C. McWilliams, and M. Banner (2011), Multiscale momentum flux and diffusion due to whitecapping in wave-current interactions, *Journal of Physical Oceanography*, *41*(5), 837–856.

Robinson, P. (1997), Nonlinear wave collapse and strong turbulence, *Reviews of modern physics*, *69*(2), 507.

Romero, L., W. K. Melville, and J. M. Kleiss (2012), Spectral energy dissipation due to surface wave breaking, *Journal of Physical Oceanography*, *42*(9), 1421–1444.

Saffman, P. G. (1992), *Vortex Dynamics*, Cambridge University Press.

Salmon, R. (1998), *Lectures on Geophysical Fluid Dynamics*, Oxford University Press.

Schwartz, L. W. (1974), Computer extension and analytic continuation of stokes expansion for gravity waves, *Journal of Fluid Mechanics*, *62*(03), 553–578.

Serrin, J. (1959), *Mathematical principles of classical fluid mechanics*, 125–263 pp., Springer.

Shariff, K., and A. Leonard (1992), Vortex rings, *Annual Review of Fluid Mechanics*, *24*(1), 235–279.

Shemer, L., E. Kit, and H. Jiao (2002), An experimental and numerical study of the spatial evolution of unidirectional nonlinear water-wave groups, *Physics of Fluids (1994-present)*, *14*(10), 3380–3390.

Stokes, G. G. (1847), On the theory of oscillatory waves, *Transactions Cambridge Philosophical Society*, *8*, 441–473.

Su, M.-Y. (1982), Three dimensional deep water waves. part 1. experimental measurement of skew and symmetric wave patterns, *Journal of Fluid Mechanics*, *124*, 73–108.

Su, M.-Y., M. Bergin, P. Marler, and R. Myrick (1982), Experiments on nonlinear instabilities and evolution of steep gravity-wave trains, *Journal of Fluid Mechanics*, *124*, 45–72.

Sulem, C., and P.-L. Sulem (1999), *The nonlinear Schrödinger equation: self-focusing and wave collapse*, vol. 139, Springer.

Sulem, C., P.-L. Sulem, and H. Frisch (1983), Tracing complex singularities with spectral methods, *Journal of Computational Physics*, *50*(1), 138–161.

Sullivan, P. P., and J. C. McWilliams (2009), Dynamics of winds and currents coupled to surface waves, *Annual Review of Fluid Mechanics*.

Sullivan, P. P., J. C. McWilliams, and W. K. Melville (2004), The oceanic boundary layer driven by wave breaking with stochastic variability. part 1. direct numerical simulations, *Journal of Fluid Mechanics*, *507*, 143–174.

Sullivan, P. P., J. C. McWilliams, and W. K. Melville (2007), Surface gravity wave effects in the oceanic boundary layer: Large-eddy simulation with vortex force and stochastic breakers, *Journal of Fluid Mechanics*, *593*, 405–452.

Sutherland, P., and W. K. Melville (2013), Field measurements and scaling of ocean surface wave-breaking statistics, *Geophysical Research Letters*, *40*(12), 3074–3079.

Tait, P. (1867), Translation of (helmholtz 1858): On the integrals of the hydrodynamical equations, which express vortex-motion, *Phil. Mag*, *33*, 485512.

Tao, T. (2006), *Nonlinear Dispersive Equations: Local and Global Analysis*, vol. 106, American Mathematical Soc.

Taylor, G. I. (1935), Statistical theory of turbulence, *Proceedings of the Royal Society of London A: Mathematical, Physical and Engineering Sciences*, *151*(873), 421–444.

Taylor, G. I. (1953), Formation of a vortex ring by giving an impulse to a circular disk and then dissolving it away, *Journal of Applied Physics*, *24*(1), 104–104.

Terray, E., M. Donelan, Y. Agrawal, W. Drennan, K. Kahma, A. Williams, P. Hwang, and S. Kitaigorodskii (1996), Estimates of kinetic energy dissipation under breaking waves, *Journal of Physical Oceanography*, *26*(5), 792–807.

Thorpe, S. A. (2005), *The turbulent ocean*, Cambridge University Press.

Tian, Z., M. Perlin, and W. Choi (2010), Energy dissipation in two-dimensional unsteady plunging breakers and an eddy viscosity model, *Journal of Fluid Mechanics*, *655*, 217–257.

Tian, Z., M. Perlin, and W. Choi (2011), Frequency spectra evolution of two-dimensional focusing wave groups in finite depth water, *Journal of Fluid Mechanics*, *688*, 169–194.

Titchmarsh, E. C. (1948), *Introduction to the theory of Fourier integrals*, Clarendon Press Oxford.

Trulsen, K. (1998), Crest pairing predicted by modulation theory, *Journal of Geophysical Research: Oceans*, *103*(C2), 3143–3147.

Trulsen, K. (1999), Wave kinematics computed with the nonlinear schrodinger method for deep water, *Journal of Offshore Mechanics and Arctic Engineering*, *121*(2), 126–130.

Trulsen, K. (2006), *Weakly Nonlinear and Stochastic Properties of Ocean Wave Fields. Application to an Extreme Wave Event*, Springer.

Trulsen, K., and K. B. Dysthe (1997), Frequency downshift in three-dimensional wave trains in a deep basin, *Journal of Fluid Mechanics*, *352*, 359–373.

Trulsen, K., I. Kliakhandler, K. B. Dysthe, and M. G. Velarde (2000), On weakly nonlinear modulation of waves on deep water, *Physics of Fluids (1994-present)*, *12*(10), 2432–2437.

Veron, F., W. K. Melville, and L. Lenain (2009), Measurements of ocean surface turbulence and wave-turbulence interactions, *Journal of Physical Oceanography*, *39*(9), 2310–2323.

White, C. (1996), A laboratory study of breaking waves using digital particle image velocimetry, Master's thesis, University of California, San Diego.

Whitham, G. (1962), Mass, momentum and energy flux in water waves, *journal of Fluid Mechanics*, *12*(01), 135–147.

Whitham, G. (1965), A general approach to linear and non-linear dispersive waves using a lagrangian, *Journal of Fluid Mechanics*, *22*(02), 273–283.

Whitham, G. B. (1974), *Linear and Nonlinear Waves*, vol. 42, John Wiley & Sons.

Yuen, H. C., and B. M. Lake (1982), Nonlinear dynamics of deep-water gravity waves, *Adv. Appl. Mech*, *22*(67), 229.

Zakharov, V., and L. Ostrovsky (2009), Modulation instability: the beginning, *Physica D: Nonlinear Phenomena*, *238*(5), 540–548.

Zakharov, V. E. (1968), Stability of periodic waves of finite amplitude on the surface of a deep fluid, *Journal of Applied Mechanics and Technical Physics*, *9*(2), 190–194.

Zakharov, V. E., V. S. L'vov, and G. Falkovich (1992), *Kolmogorov Spectra of Turbulence 1. Wave Turbulence.*, vol. 1, Springer.

Zufiria, J. A. (1987), Non-symmetric gravity waves on water of infinite depth, *Journal of Fluid Mechanics*, *181*, 17–39.